

AMERICAN UNIVERSITY OF BEIRUT

NON-INVASIVE DIAGNOSIS AND MONITORING OF SKIN
ANOMALIES

by
NADER MOHAMAD SHAFI

A thesis
submitted in partial fulfillment of the requirements
for the degree of Master of Engineering
to the Department of Electrical and Computer Engineering
of the Maroun Semaan Faculty of Engineering and Architecture
at the American University of Beirut

Beirut, Lebanon
January 2021

AMERICAN UNIVERSITY OF BEIRUT

NON-INVASIVE DIAGNOSIS AND MONITORING OF SKIN
ANOMALIES

by
NADER MOHAMAD SHAFI

Approved by:

Dr. Joseph Costantine, Associate Professor
Electrical and Computer Engineering



Advisor

Dr. Rouwaida Kanj, Associate Professor
Electrical and Computer Engineering



Co-Advisor



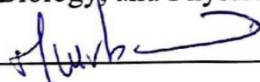
Dr. Youssef Tawk, Assistant Professor
Electrical and Computer Engineering

Member of Committee



Dr. Assaad Eid, Associate Professor
Anatomy, Cell Biology, and Physiological Sciences

Member of Committee



Dr. Mazen Kurban, Associate Professor
Dermatology

Member of Committee



Dr. Ali Ramadan, Assistant Professor
Electrical Engineering
Fahad Bin Sultan University

Member of Committee

Date of thesis defense: January 27, 2021

ACKNOWLEDGEMENTS

The work presented herein was successfully completed in 2020, one of the most challenging and unusual of years, through perseverance, dedication, and patience.

To my supervisors who have become family to me, Prof. Joseph Costantine and Prof. Rouwaida Kanj, thank you for your guidance, your limitless support throughout this journey, and your constant motivation.

To the amazing committee members: Prof. Youssef Tawk, Prof. Assaad Eid, Prof. Mazen Kurban, and Prof. Ali Ramadan, thank you for being part of my thesis committee and providing me with helpful advice and insights.

To my family and friends, thank you for the unconditional support and encouragement, and for always believing in me.

Finally, I could not have made it without the guidance and patience bestowed upon me from God.

ABSTRACT OF THE THESIS OF

Nader Mohamad Shafi

for

Master of Engineering

Major: Electrical and Computer
Engineering

Title: Non-Invasive Diagnosis and Monitoring of Skin Anomalies

Skin cancer, Acne, Eczema, among others, are some of the most commonly occurring skin anomalies that impose debilitating strain on the health of affected individuals and impede their social and economic welfare. The world health organization estimates between 2 to 3 million skin cancer cases occurring globally every year, highlighting its commonality. However, traditional skin disease diagnosis techniques typically followed by medical professionals, including physicians and dermatologists, primarily rely on qualitative and invasive measures, such as visual screening and biopsies. Therefore, developing an adjunctive tool that assists medical professionals in providing diagnosis that is more accurate in a low-cost, non-invasive manner is highly advantageous. Such a novel tool relieves the time-consuming and uncomfortable procedures of traditional diagnosis methods. Additionally, proper monitoring and characterization of the condition of a skin anomaly increases the chances of successful treatment. Keeping in mind that early diagnosis reduces any potential health complications.

Extensive research measures have been taken in the pursuit of non-invasive, low-cost, and reliable diagnosis and monitoring methods. In the radio-frequency domain, clear differentiation between healthy and malignant tissues has been shown. Throughout this thesis, a novel and complete system for the non-invasive diagnosis and monitoring of skin anomalies using radio-frequency technology is designed and validated. The portable and handheld system comprises a highly sensitive electromagnetic sensor, custom wave analyzer circuitry, and the corresponding firmware and statistical classification algorithms. The system is then validated by performing clinical trials on patients with pre-diagnosed skin cancer and on healthy controls. Our findings illustrate a clear, distinct, and consistent differentiation between healthy and cancerous skin lesions, thereby conceiving a powerful tool that has the ability to augment traditional diagnosis methods to improve clinical diagnosis accuracy and enhance the patients' overall quality of life.

CONTENTS

ACKNOWLEDGEMENTS	1
ABSTRACT	2
ILLUSTRATIONS	6
TABLES	10
INTRODUCTION	11
LITERATURE REVIEW	14
A. Introduction.....	14
B. Electromagnetic Probes	14
1. Millimeter Wave (mm-Wave) Reflectometry.....	14
2. Micro-Machined Dielectric Resonator Waveguide at 100 GHz.....	16
3. Evanescent Electromagnetic Waves for High Resolution Measurements.....	17
4. A Near-Field Microwave Sensor	19
5. High Resolution Imaging Using Resonance Probes	21
6. A Split Ring Resonator Dielectric Probe	22
C. Vector Network Analyzers	23
1. Integrated Network Analyzer.....	23
2. Single-Port Vector Network Analyzer.....	25
THE INTERACTION OF ELECTROMAGNETIC WAVES WITH BIOLOGICAL TISSUE.....	26
A. Introduction.....	26
B. Permittivity, Dispersion, and Relaxation	26

C. The Physiology and Anatomy of Skin and The Most Common Types of Skin Cancer	29
1. Skin	29
2. Skin Cancer	31
D. Interaction of EM Waves with Skin Lesions	32
E. Discussion	35

TECHNIQUES FOR DIELECTRIC CHARACTERIZATION ..36

A. Introduction.....	36
B. Planar Non-Resonant Methods	38
1. Reflection Methods.....	38
2. Transmission/Reflection Methods	38
C. Planar Resonant Methods	39
1. The Planar One-Port Resonant Probe	39
2. The Ring Resonator	40
3. The Ribbon Resonator:	41
D. Discussion	42

THE SKIN ANOMALY DETECTION DEVICE43

A. Introduction.....	43
B. What are we measuring? - Scattering Parameters (S Parameters).....	43
C. The Microwave Sensor	44
1. Preliminary Microwave Sensor Design	45
2. The Improved Microwave Sensor.....	47
D. Backend Analyzer Circuit.....	55
1. Microwave Structures	56

2. Proposed VNA Architecture: WaveWhisperer.....	58
E. Discussion.....	84
CLINICAL TRIALS	86
A. Introduction.....	86
B. Measurements on Skin Cancer Patients.....	86
C. Measurements on a Healthy Control Group	89
D. Discussion.....	89
ANALYSIS, RESULTS, AND DISCUSSION	91
A. Introduction.....	91
B. Performance: The Distinct Response to Healthy and Cancerous Skin Lesions .	91
C. Model Design, Analysis, and Results	93
1. Imbalanced to Balanced Data: Synthetic Minority Oversampling Technique (SMOTE):	93
2. Support Vector Machines (SVM):.....	94
3. Approaches for Classification and Prediction	97
D. Discussion.....	106
CONCLUSION AND FUTURE WORK.....	108
BIBLIOGRAPHY	109

ILLUSTRATIONS

Figure

1. Punch Biopsy illustration from [4].	12
2. Reflectometer setup in [8].	15
3. Tapered DRW in [9].	17
4. S_{11} measurements for different dielectric samples from [9].	17
5. Tapered EMP in [18].	18
6. Shift in S_{11} and frequency in [18].	19
7. (a) Optical image of a tooth, (b) EMP image of tooth in [18].	19
8. Near-field characteristics of the probe in [19].	20
9. Photograph of sample under test, (a) without skin, (b) with skin, S_{11} image (c), frequency shift image (d) in [19].	20
10. Magnitude of E-Field in [20].	21
11. Loaded aperture probe in [20].	21
12. Photograph of sample test structure, (a) optical photograph, (b) S_{11} -based image reconstruction from [20].	22
13. SRR setup (a), field concentration (b) in [21].	23
14. The variation of the transmission coefficient S_{21} as a function of an alternating permittivity test structure in [21].	23
15. TINA in [22].	24
16. System schematic in [22].	24
17. VNA in [23].	25
18. Comparison between magnitude and phase of S_{11} of the proposed VNA vs a commercial VNA in [23].	25
19. Dispersion ranges from [28].	28
20. The dielectric spectrum of Skin and Heart tissue from [26].	29
21. The anatomy of skin [4].	30
22. The Fitzpatrick Scale [32].	31
23. Illustration of BCC, SCC, and Melanoma [37].	33

24. The test setup in [17], and the corresponding measured permittivity values of BCC, SCC, where (a) shows the real part, and (b) shows the complex part.....	34
25. System overview and obtained results [10].....	34
26. Wave at a boundary from [24].	37
27. A typical dielectric characterization kit with a VNA [38].	37
28. Transmission Line and loaded transmission line from [24]......	38
29. Near-field probe from [24].	39
30. Circuit models from [24]......	40
31. Effect of frequency on penetration depth in [24].	40
32. Ring resonator from [24]......	41
33. Ribbon resonator from [24]......	42
34. Radiation regions [40]......	44
35. The proposed EM Sensor.	46
36. The fabricated sensor.	47
37. The measured and simulated S_{11} of the proposed sensor.	47
38. EM field locations at the sensor's tip.....	49
39. Topology of the improved microwave sensor.....	51
40. (a) E-field distribution along the resonator, (b) along the hemispherical tip. (c) E-field projection on a SUT. (d) The enclosed sensor.....	52
41. An illustration of a typical sensing scenario. The figure is modified from http://www.scientificanimations.com/wiki-images/	53
42. The simulated and measured S_{11} of the proposed sensor.	54
43. Photograph of the assembled sensor within its enclosure.	55
44. Directional Coupler illustration from [23].	56
45. A functional block diagram of the proposed analyzer architecture.....	59
46. ADS schematic of the 40 MHz LPF.....	64
47. Simulated results of the LPF at (a) small bandwidth, and (b) large bandwidth.....	64
48. The magnitude response of the AD8302 (a), and its phase response (b) [51].	66
49. The effect of introducing a 90° phase shift [52]......	67

50. ADS schematic of the 90 degrees phase shifter.	68
51. Simulated performance of the phase shifter.	68
52. The schematic of microcontroller and the power sections of the proposed architecture.	70
53. The schematic of the utilized PLL.	71
54. The schematic of the down-conversion and detection chain.....	71
55. The different layers of the PCB. (a) Layer 1, (b) Layer 2, (c) Layer 3, and (d) Layer 4.....	73
56. A Top-layer view of the designed PCB.	74
57. 3D rendered view of the top and bottom layers.	74
58. Exploded view of all layers. Blue layers represent the silkscreen, golden layers represent copper, and white layers represent the dielectric material.....	75
59. Locations of the VIA stitches and the ground pour.	76
60. The fabricated PCB.	77
61. The soldered PCB (a) top layer, and (b) bottom layer.	77
62. The source frequency module.	77
63. The WaveWhisperer PCB in the palm for scale.....	78
64. Screenshots from the spectrum analyzer, showing the synthesized frequencies: (a) 1 GHz, (b) 2 GHz, (c) 3 GHz, and (d) 6 GHz.	79
65. WW while powered on. The red LED module is the transmitter, and the blue LED module is the receiver.	80
66. The raw and the calibrated S11 of the used EM sensor.	81
67. (a) The S11 response with and without loading. (b) The FIR filtered response.	82
68. The phase response of the two detectors in: (a) the raw unloaded state, (b) the FIR filtered unloaded state, (c) the raw loaded state, and (d) the filtered loaded state. .	83
69. (a) The raw unloaded and loaded 0-360° phase response. (b) The FIR filtered version of the phase response.	83
70. Most common cancer locations throughout the clinical trials. This figure is modified from https://www.pixtastock.com/illustration/60972716	88
71. The EM sensor placed on top of skin.	92
72. S11 magnitude measurement of a skin cancer and its adjacent healthy skin.....	93

73. S11 phase measurement of a skin cancer and its adjacent healthy skin.	93
74. Illustration of SMOTE synthesis [62].	94
75. Typical SVM hyperplanes [75].	96
76. S11 magnitude variation between healthy and cancerous lesions for 12 patients. .	98
77. S11 phase variation between healthy and cancerous lesions for 10 patients.	99
78. S11 magnitude variation between two forehead locations for 11 volunteers.	99
79. S11 phase variation between two forehead locations for 11 volunteers.	100
80. The overall magnitude and phase sample points and the corresponding predictions.	103
81. Four runs of the SVM model fed by training and testing data shuffled randomly.	103
82. The model's test outcome with and without SMOTE employed.....	104
83. CV error as a function of number of features for every used kernel function.	106

TABLES

Table

1. Obtained results in [8].	16
2. DIVA values for different frequency ranges.	62
3. Patient details.....	88
4. Overall subject and measurement information.	89
5. CV evaluation of the polynomial, RBF, and linear kernels.....	102
6. Performance metrics for the best SVM model.	102
7. Performance metrics for the FFSW approach.	106

CHAPTER I

INTRODUCTION

Skin is the largest organ of the human body, covering almost 1.85 square meters in area. Several skin anomalies affect skin and cause individuals irritation or even hinder daily life activities, such as skin cancer, Psoriasis, Eczema, and Acne. Skin cancer is notably one of the most dangerous among these diseases, especially in the case of Melanoma [1]. In fact, skin cancer is the most common type of cancer, where the world health organization (WHO) estimates that 2-3 million non-Melanoma cancers and more than 130,000 Melanoma cancers occur globally each year [2]. Skin cancer is divided into two categories, Melanoma and non-Melanoma. Non-melanoma skin cancers are mainly Basal Cell Carcinoma (BCC) and Squamous Cell Carcinoma (SCC) which are often non-lethal and comprise the largest portion of skin cancers. Non-Melanoma skin cancer is often a byproduct of excessive exposure to UV radiation and is usually present in areas of the body that are regularly exposed to sunlight, such as the arms, legs, and the neck [2].

On the other hand, Melanoma is referred to as the major cause of death originating from skin cancer. Studies indicate the existence of a correlation between risk of having malignant melanoma and genetic predisposition as well as UV exposure [2]. It is necessary to emphasize that early diagnosis and timely intervention increase the chances of successful treatment, enhance survival rate, and prevent harmful complications [3].

Typically, a medical professional follows certain procedures in order to diagnose skin anomalies. First, the medical professional starts with visual inspection

and seeks the observable signs and symptoms such as the size, color, and shape of the lesion. Typically, a dermatoscope, essentially a magnifying lens with integrated illumination, allows the dermatologist to examine the anomaly more clearly. If the anomaly is suspicious, an invasive surgical procedure known as the biopsy is often required. A biopsy involves the extraction of a sample from the suspected lesion in aims of performing histopathological examination to determine its malignancy. However, biopsies are invasive, uncomfortable, cost-inefficient, and potentially cause disfigurement. One type of biopsy, the punch biopsy, can be seen in Fig. 1 [4].

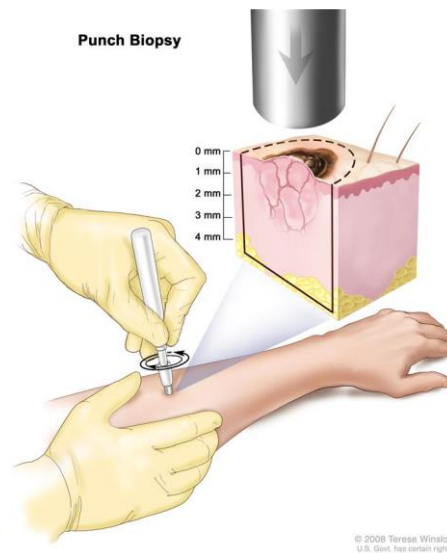


Figure. 1. Punch Biopsy illustration from [4].

Due to the inconvenient, invasive, and time-consuming methods of diagnosis, many researchers have explored the potential of electromagnetic (EM) waves as non-invasive means for the characterization of healthy and anomalous skin. As a result, several publications have verified the ability of EM-based techniques to characterize human skin permittivities at different frequencies [5]-[6]. Several other works in the literature have identified differences between healthy and anomalous skin tissues [5], [7], [8]–[11], which is mainly attributed to the increased interaction between EM waves

and the increased water content within malignant skin lesions along with other dielectric differences. This technology has also proved its efficacy throughout its application in the detection of lung cancer [12], the measurement of skin hydration [13], and several other industrial applications such as sub-surface imaging of buried structures [14], inspection of glass specimens [15], and even the detection of corrosion [16].

In this work, we propose a novel, compact, and non-invasive sensing system that is tailored for the detection of skin cancer. This system involves a highly sensitive electromagnetic sensor, a custom-made wave analyzer, and the corresponding classification algorithms. Our proposed system exhibits several advantages that distinguish it from other approaches, related to sensitivity, compactness, and design optimizations that account for several challenges in such detection systems. Additionally, the proposed system is validated by clinical trials on patients and healthy volunteers. Finally, the observations are comprehensively analyzed, and the relevant statistical models that best differentiate the measured classes are produced.

Chapter two of this thesis provides a literature review that discusses the background technology for such diagnosis and monitoring technique. Chapter three discusses the interaction between electromagnetic fields and biological tissues. Chapter four presents different techniques of characterizing dielectric materials. Chapter five discusses the full device implementation, including background knowledge, EM sensor design, and the development of the back-end circuitry. Chapter six discusses the performed clinical trials and the pertinent procedures. Chapter seven provides the analysis of the obtained results as well as the designed models and their performance. Chapter eight concludes the proposed project and delivers insightful vectors for future work.

CHAPTER II

LITERATURE REVIEW

A. Introduction

The ability of EM fields to non-invasively and non-destructively characterize dielectric properties of materials has made it one of the most attractive technologies for sensing applications. Consequently, extensive research has been implemented in the literature regarding the utilization of EM-based solutions for diverse applications spanning the medical, agricultural and industrial domains. In this chapter, we review some of the most relevant works in the literature that discuss EM-based sensors and signal analyzer circuitry in aims of understanding the current state of research within this area. This section will be divided into two sub-sections: Electromagnetic Probes and Vector Network Analyzers.

B. Electromagnetic Probes

1. Millimeter Wave (mm-Wave) Reflectometry

The work presented in [8] introduces a system for the early detection of skin cancer operating within the mm-Wave portion of the frequency spectrum. Accordingly, two design variations based on a mm-Wave reflectometer are introduced. Traditionally, a reflectometer is a system that is used to measure the EM signal reflection properties of a device under test (DUT). In this case, the reflectometer is utilized to quantify the level of the reflected EM waves off skin. Depending on the nature of the specimen under test (healthy vs. malignant tissues), the output of the reflectometer is expected to change accordingly. The proposed reflectometer circuit is created by combining a Y-circulator,

an open-ended waveguide, a Gunn diode, and a zero-bias Schottky diode that outputs the voltage magnitude of the reflected wave. The open-ended waveguide is pressed against skin tissue while the Gunn diode generates a signal at the frequency of interest. The EM waves are then reflected off the skin, and the Y-circulator separates the transmitted waves from the reflected ones. The latter then passes through a Schottky diode that transforms the time-varying reflected signal into a DC voltage level. The first design employs a WR-22 waveguide operating at 42 GHz and the second design employs a WR-15 waveguide operating at 70 GHz. The proposed setup in [8] is shown in Fig. 2. The system is tested on healthy skin, benign lesions, and BCC tissue, where clear differences in terms of the reflected voltages were obtained. The obtained results are presented in Table 1.

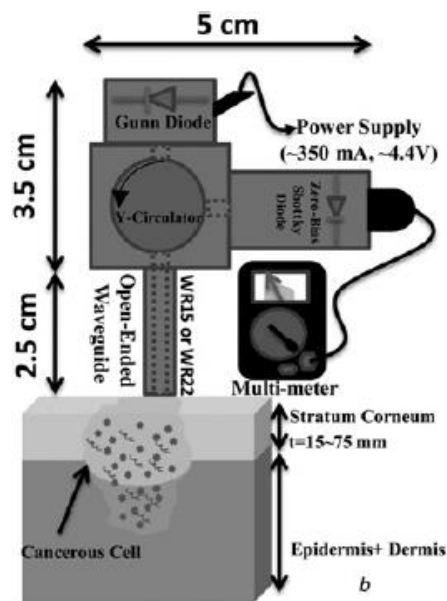


Figure 2. Reflectometer setup in [8].

Table 1. Obtained results in [8].

Biological Object	Reflection, mV
Healthy Skin	12-12.8
Benign Lesion	10.5-11
Basal Cell Carcinoma	6.8-7.7

2. *Micro-Machined Dielectric Resonator Waveguide at 100 GHz*

In [9], a method for distinguishing tumors from healthy skin is proposed by relying on a tapered probe based on a dielectric rod waveguide (DRW) that operates between 94 GHz and 106 GHz. The objective of the proposed work is to obtain an aperture that is small enough for precision sensing of a tumor without involving portions of healthy skin in the measurements. The waveguide and the probe setup are shown in Fig. 3. To validate the operation, silicon test materials that contain air gaps of variable sizes are designed. These artificial materials are specifically designed to mimic the dielectric properties of real anomalies in the skin. Subsequently, the probe's aperture is loaded with the artificial materials that have varying dielectric properties, and then the reflection coefficient, S_{11} , is measured for each material. The results illustrate clear differences in the magnitude of the S_{11} for the various materials used, as shown in Fig. 4. This work concludes that the designed probe exhibits adequate sensitivity for permittivity values that mimic those of healthy and diseased skin.

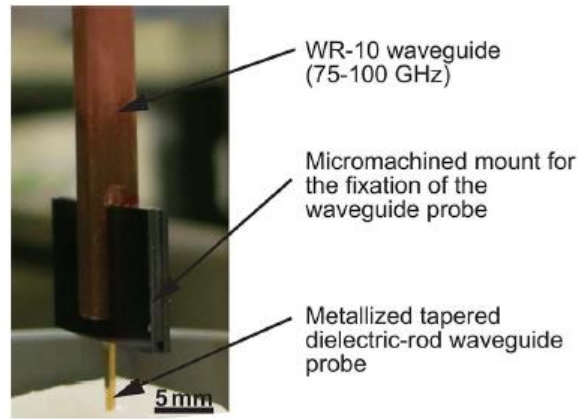


Figure. 3. Tapered DRW in [9].

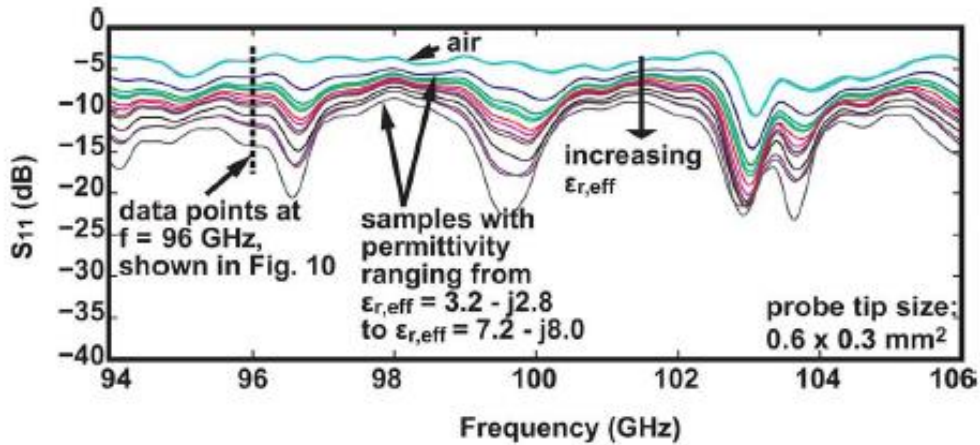


Figure. 4. S_{11} measurements for different dielectric samples from [9].

3. *Evanescent Electromagnetic Waves for High Resolution Measurements*

In [18], a new method is introduced for imaging materials with variations in conductivity, permittivity, and density. This work proposes a planar resonator that utilizes perturbations in its EM field to perform different sensing roles. One of its most interesting features is that it overcomes the Abbe barrier. This barrier designates the spatial resolution limit that electromagnetic waves can achieve as half the wavelength used, or $\lambda/2$, where λ is the wavelength. This limit is surpassed by utilizing evanescent electromagnetic waves, such as the fringing electric and magnetic fields from a

resonator's conductor. By relying on these evanescent waves, the resolution becomes controlled by the geometry of the used probe. Hence, as the probe's effective sensing tip reduces in size, its resolution increases. For that reason, an Evanescent Microwave Probe (EMP) based on a $\lambda/2$ microstripline resonator is designed at 985 MHz, and its edge is tapered so that the lateral resolution can be increased. The topology of this sensor can be seen in Fig. 6 [18].

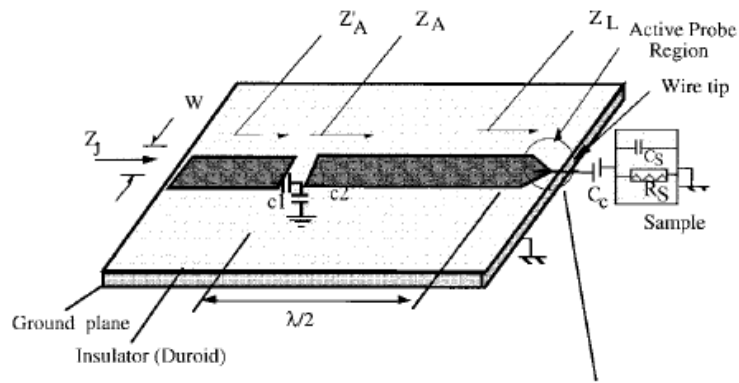


Figure. 5. Tapered EMP in [18].

The spatial resolution achieved is around $0.4 \mu\text{m}$. It is important to note that the electric field decays exponentially with distance from the sample. In addition, Fig. 6 displays the shift in the frequency and magnitude of the S_{11} when the probe is placed over a metal, illustrating the sensitivity of the probe. In Fig. 7(a) we can see an optical image of a tooth, and Fig. 7(b) shows an image obtained via the EMP scanning over a tooth specimen, verifying the ability of the EMP to sense small changes in the dielectric properties [18].

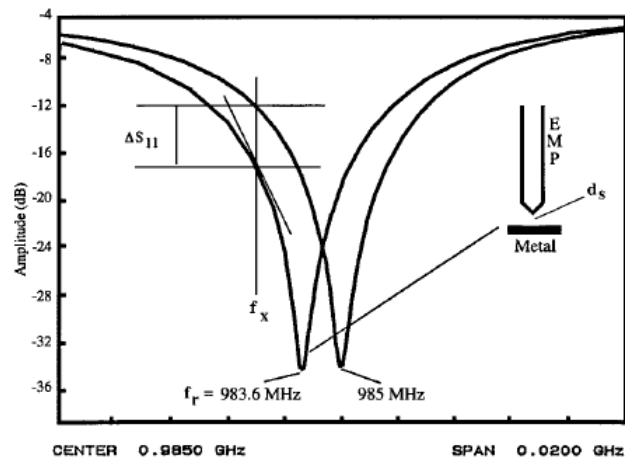


Figure. 6. Shift in S_{11} and frequency in [18].

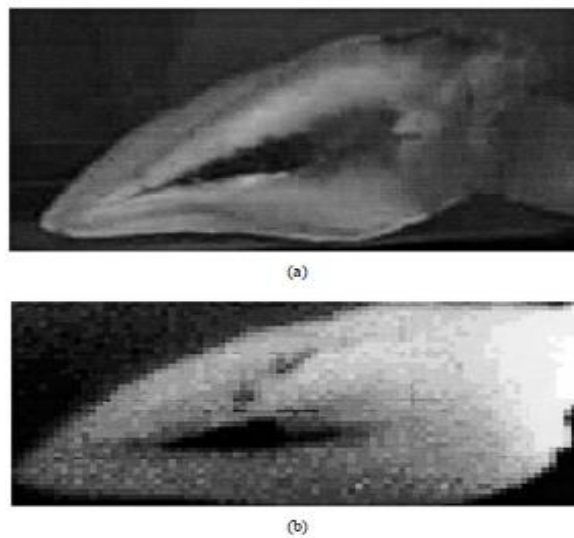


Figure. 7. (a) Optical image of a tooth, (b) EMP image of tooth in [18].

4. A Near-Field Microwave Sensor

In [19], a near-field microwave resonator is designed for the detection of biological abnormalities in skin. The resonator probe shown in Fig. 8 consists of a gap-coupled $\lambda/2$ microstrip line that is tapered to achieve a finer sensing resolution as well as to obtain a higher quality factor (Q-Factor). Furthermore, the design is fabricated and tested on chicken meat and fat which were covered with chicken skin to represent tumors or lipomas beneath the skin. Then, the specimen is scanned with the proposed

probe to produce a 2D S_{11} image. The results show a significant change in S_{11} magnitude across fat measurements. Fig. 9(a) and Fig. 9(b) show the used chicken meat and the corresponding skin layer. Additionally, Fig. 9(c) and Fig. 9(d) show the 2D S_{11} images of the used specimen after scanning them with the probe.

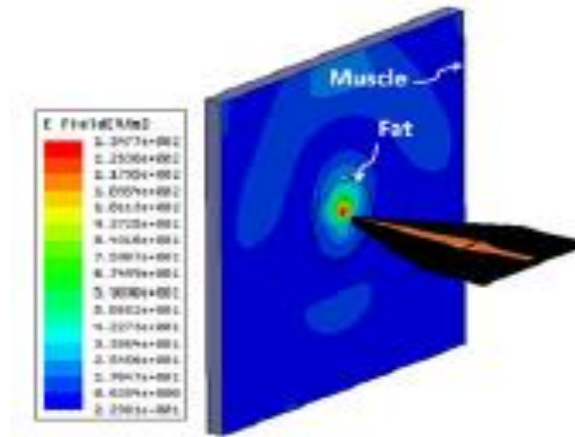


Figure. 8. Near-field characteristics of the probe in [19].

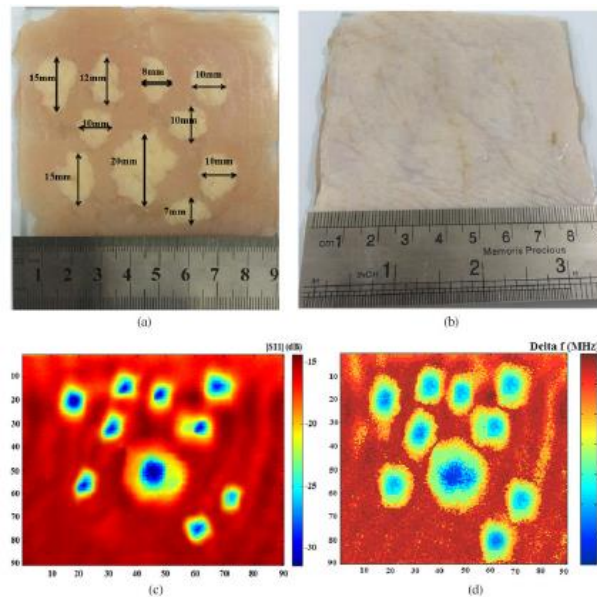


Figure. 9. Photograph of sample under test, (a) without skin, (b) with skin, S_{11} image (c), frequency shift image (d) in [19].

5. High Resolution Imaging Using Resonance Probes

In [20], two near-field probes for resonance imaging are proposed. First, a loaded aperture is designed to resonate at around 4 GHz. The aperture is loaded with a folded open loop resonator having a length of $\lambda/2$ at 4 GHz. The second design is a helix antenna that operates at 4 GHz. Both structures are designed to exhibit tight field localization. In Fig. 10, we can see the magnitude of the electric field of the helix antenna, showing maximum sensitivity, highlighted in red, directly below it [20].

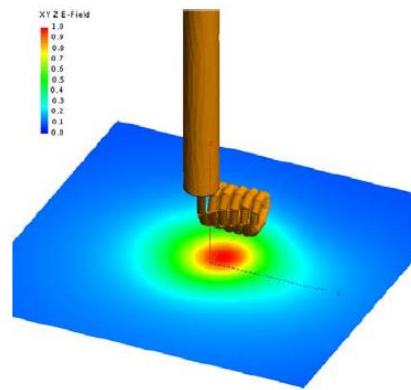


Figure. 10. Magnitude of E-Field in [20].

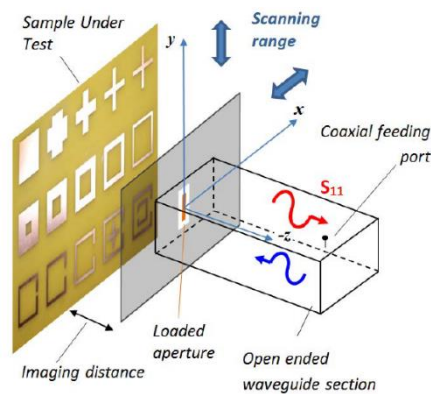


Figure. 11. Loaded aperture probe in [20].

Fig. 11 displays the resonantly loaded probe along with its test structure. In Fig. 12(a), a test structure is constructed using fragments of a dielectric material with varying dimensions. After scanning the entire test structure with the helix antenna, the

2D S_{11} image in Fig. 12(b) is obtained. This 2D image verifies the loaded aperture probe's ability to detect the dielectric fragments due to their distinct dielectric nature. Both designs exhibit a high sensitivity and result in high quality images.

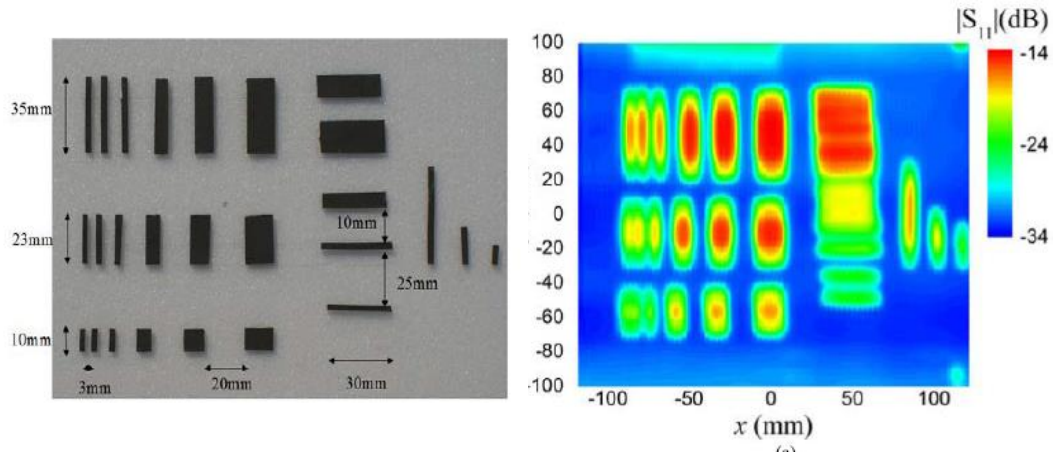


Figure. 12. Photograph of sample test structure, (a) optical photograph, (b) S_{11} -based image reconstruction from [20].

6. A Split Ring Resonator Dielectric Probe

In [21], a split ring resonator (SRR) is investigated for the imaging and characterization of composite dielectric materials. Composite dielectric materials provide interesting electromagnetic properties such as variable dielectric permittivity and magnetic permeability values. Consequently, a sensor must be able to sense the fabricated material in order to ensure that the composite's electromagnetic properties match the simulated ones. An SRR is introduced as a sensing element that can achieve sub-millimeter resolution as well as the ability to cover larger areas of composite materials. The sensor setup can be seen in Fig. 13(a). The SRR resonates at a certain natural resonance frequency based on its inherent capacitance and inductance. When the ring is positioned on a material's surface, these capacitance and inductance values are disturbed based on the interaction of the generated EM field with the material under

test. This disturbance is manifested as changes in the transmission coefficient, S_{21} . In Fig. 13(b), we can see that the probe is highly sensitive at its open-end gap based on the intensity field within. The probe was tested over an array of materials with alternating dielectric properties, where a “chess-board”-like material is 3D printed with alternating permittivity values. An electromagnetic image is generated after scanning the material with the probe, as can be seen in Fig. 14 [21].

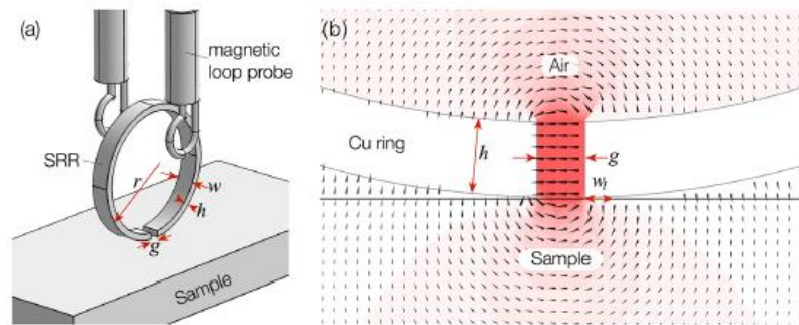


Figure. 13. SRR setup (a), field concentration (b) in [21].

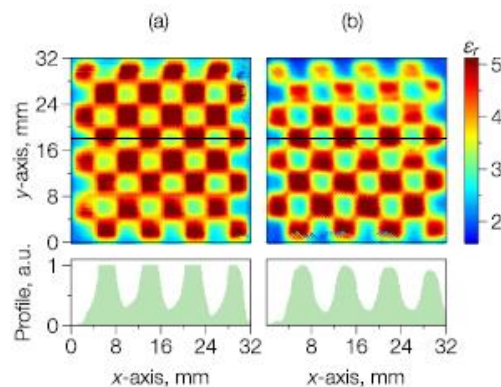


Figure. 14. The variation of the transmission coefficient S_{21} as a function of an alternating permittivity test structure in [21].

C. Vector Network Analyzers

1. Integrated Network Analyzer

In [22], a highly portable integrated network analyzer is designed and tested.

The network analyzer abbreviated by “TINA” (Tiny Integrated Network Analyzer) is a

solution to the difficult on-device measurement of electrically small antennas. TINA is composed of a microcontroller and RF circuitry whose function is to measure the S-parameters of a two-antenna system, and the device can be seen in Fig. 15. The RF circuitry mainly revolves around the AD8302 gain and phase detector. The function of the AD8302 is to measure the difference in magnitude and phase of the two inputs coming from a directional coupler by outputting voltages that can be later transformed into S-Parameters. The results have shown an acceptable level of accuracy for the measurement in GSM operation. The schematic of the system can be seen in Fig. 16.

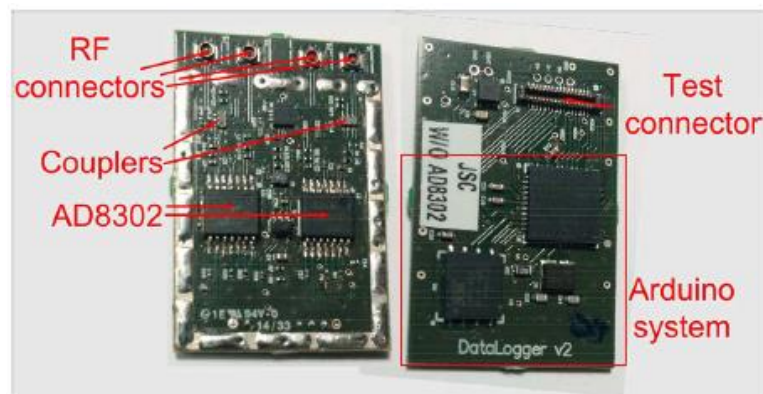


Figure. 15. TINA in [22].

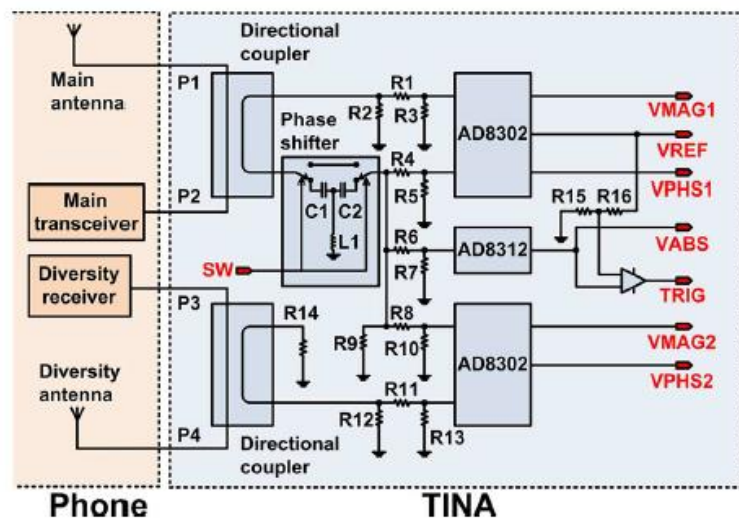


Figure. 16. System schematic in [22].

2. Single-Port Vector Network Analyzer

In [23], a VNA design is proposed using an electronically controllable phase shifter, a transmission line, and a diode power detector. This VNA architecture relieves the complexity of the traditional heterodyne VNAs, and it functions similar to a slotted-line. By measuring the power of the standing wave formed on the transmission line at different locations, the magnitude and phase of the S_{11} can be measured. The integration of an electronically controllable phase shifter was extremely advantageous in reducing the number of needed diodes. This is due to the fact that the phase shifter mimics the effect of moving a power detector along the transmission line, resulting in measurements at multiple points on it. The block diagram of this system can be seen in Fig. 17. Results obtained by the proposed VNA are compared to ones obtained from a commercial VNA, and very good agreement is observed as shown in Fig. 18.

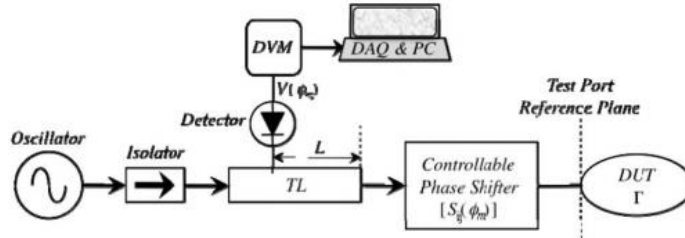


Figure. 17. VNA in [23].

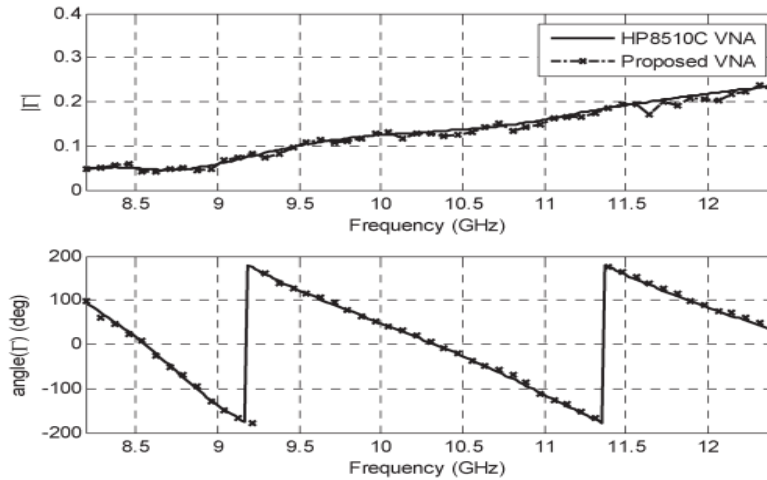


Figure. 18. Comparison between magnitude and phase of S_{11} of the proposed VNA vs a commercial VNA in [23].

CHAPTER III

THE INTERACTION OF ELECTROMAGNETIC WAVES WITH BIOLOGICAL TISSUE

A. Introduction

In this chapter, we introduce important concepts and terms --relevant to the dielectric properties of materials-- that will serve as building blocks for the forthcoming study. We also discuss the physiology and anatomy of skin and skin cancer to obtain a solid understanding of their constituents which will highlight their differences and orient our design decisions. Finally, we emphasize on the link between these differences and the variation of the electromagnetic behavior of a sensing structure.

B. Permittivity, Dispersion, and Relaxation

When discussing the complex dielectric properties of different materials, such as skin and other tissues, we are particularly concerned with the complex relative permittivity. The permittivity of a material describes how charges within it react when exposed to an electric field. In other words, permittivity is a property that allows us to understand a material's ability to store and absorb electromagnetic energy. The complex relative permittivity is often referred to the free-space permittivity and denoted by ϵ_r , which is defined by $\epsilon_r = \epsilon'_r - j\epsilon''_r$. The real part of the complex permittivity ϵ'_r is known as the dielectric constant, and the complex part ϵ''_r is known as the dielectric loss factor. Both terms, as will be shown in the proceeding section, depend on frequency and other factors that are specific to the material under test [24].

Over the years, numerous works in the literature have experimentally characterized the dielectric properties of human tissue, such as skin, muscle, bones, and

various other body organs over different frequency ranges [25]–[27]. This was heavily motivated by the by the need to understand the effect of EM exposure on tissues, specifically relevant to the field of dosimetry, and to aid in building better models used in simulations [28].

The complex relative permittivity of materials and its variation with frequency is defined as *Dielectric Dispersion*, and it is ideally approximated by the Debye model, given by (1), where ϵ_∞ is the permittivity at the high frequency limit, ϵ_s is the permittivity at low frequencies, τ is the relaxation time, and ω is the angular frequency [24].

$$\epsilon_r = \epsilon_\infty + \frac{\epsilon_s - \epsilon_\infty}{1 + j\omega\tau} \quad (1)$$

The plot in Fig. 19 shows an abstract illustration of the behavior of both the real and imaginary parts of the complex permittivity of tissues as a function of frequency. *Dispersion* occurs due to the fact that materials are electrically polarized once exposed to an electric field, causing changes in the charge distribution within. Having become polarized, the particles within will arrive at a new equilibrium once the applied electric field is altered, consequently changing the distribution and orientation of the charged particles. The time it takes to reach the new equilibrium is defined as the *Relaxation Time*. Depending on the composition of the material, different relaxation times are obtained, providing significant insight into the properties of the MUT [26].

Due to the complex nature of biological tissue, the simplified Debye model given by (1) may not accurately describe its dielectric spectrum. This is a result of the existence of multiple compounds and substances within biological tissues that may not be characterized using the same relaxation times, which causes different dispersion

regions to broaden. As a result, the Cole-Cole model given by (2) modifies the original Debye model, most notably by the introduction of a loss factor α to account for broadening, and it is commonly used to approximate the dielectric spectrum of tissues.

$$\epsilon_r = \epsilon_r' - j\epsilon_r'' = \epsilon_\infty + \frac{\epsilon_s - \epsilon_\infty}{1 + (j\omega\tau)^{1-\alpha}} \quad (2)$$

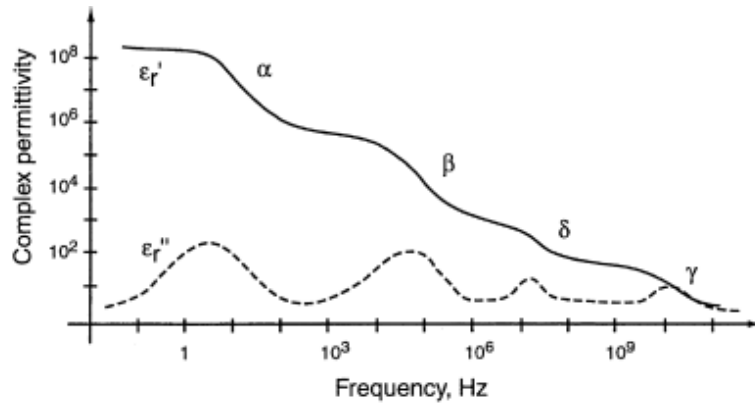


Figure. 19. Dispersion ranges from [28].

The dielectric spectrum of tissues is typically divided into 3 primary dispersion regions known as the α , β , and γ dispersions, as shown in Fig. 19. These dispersions relate the change of permittivity at certain frequency ranges to physiological and chemical phenomena within the tissue under test. To illustrate, the α and β dispersions are primarily caused by the different properties of cell membranes, surface conductance, and the cellular structures. Whereas the γ -dispersion that is dominant at sub-GHz frequencies is mainly governed by the water and protein content of the tissue [28].

Understanding the dispersion properties of biological tissues allows us to understand the cause of variability in their dielectric properties. By linking the known variability in response of water molecules, proteins, acids, and glucose to variations in skin dielectric properties, researchers are able to identify the main factors responsible for dielectric variations between anomalies and healthy skin.

Fig. 20 illustrates some of the experimental results obtained from the characterization of tissues in [26], namely skin and heart tissues respectively, by plotting the behavior of the ϵ_r' and ϵ_r'' as a function of frequency. To obtain these plots, measurements were performed on the respective tissues using a dielectric characterization kit. This kit is mainly composed of a coaxial probe that is placed directly on the MUT, while being connected to a VNA that runs a dielectric characterization software. Essentially, the VNA measures the S_{11} over a wide bandwidth and transforms it into permittivity values.

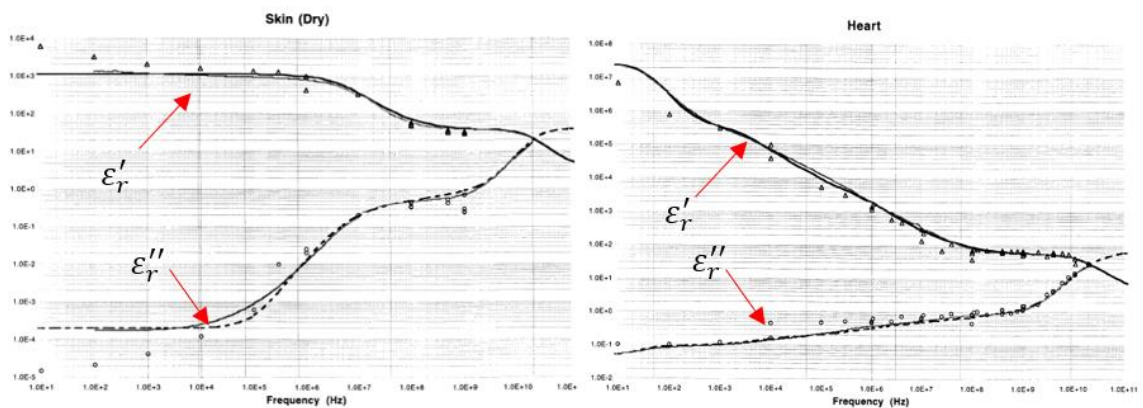


Figure. 20. The dielectric spectrum of Skin and Heart tissue from [26].

C. The Physiology and Anatomy of Skin and The Most Common Types of Skin Cancer

1. Skin

Skin, the largest organ of the human body and its first line of defense, is composed of three main layers as shown in Fig. 21. The epidermis is outermost layer, followed by the dermis and the subcutaneous tissue. The epidermis is primarily composed of cells known as keratinocytes, whose function is to synthesize keratin, a protein that controls the rigidity of the skin as well as to assume protective roles such as response to injury (cytokines). On the other hand, the dermis acts as a durable, yet

flexible, layer that prevents mechanical injury and plays important roles in thermoregulation whilst including receptors for various stimuli such as temperature and pressure. The dermis is composed of different cells such as fibroblasts, ground substance, and fibers, and it significantly contributes in synthesizing different macromolecules and proteins. Notably, fibroblasts are cells that produce collagen, a protein that represents 30% of the dermis' volume, and it is considered one of the building blocks of bones, skin, and other tissues. The last layer, subcutaneous tissue, is mainly composed of fat cells known as lipocytes with blood vessels and collagen seeping in between. Subcutaneous tissue undertakes roles related to energy storage, buoyancy and hormone conversion. The thickness of these layers depends on the specimen's location on the body [29], [30]. For example, the epidermis significantly changes in thickness on the eyelid (<0.1mm) when compared to the palms and soles (~1.5 mm) [31].

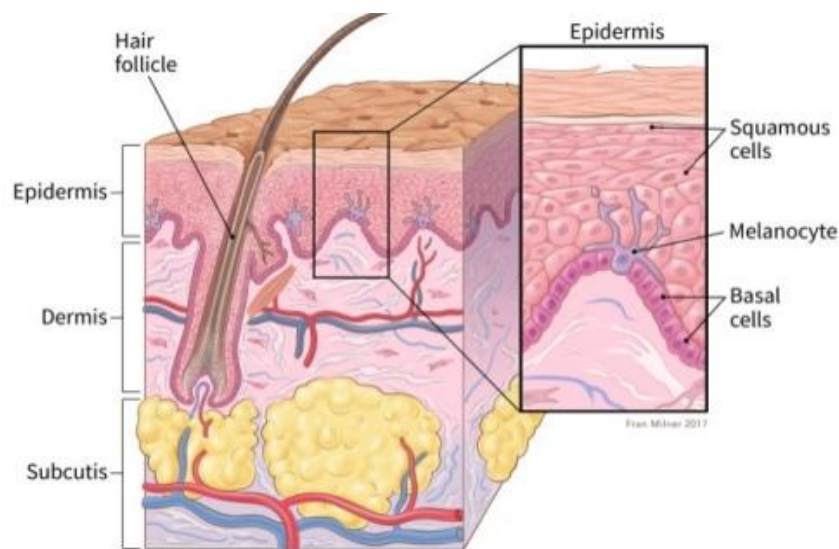


Figure. 21. The anatomy of skin [4].

It is necessary to note that different skin tones react differently to environmental factors, where some skin tones are more susceptible to damage from the environment,

e.g.: UV-exposure and burns. As a result, the Fitzpatrick skin scale is a system used to predict the response of different skin tones to sun exposure based on the amount of melanin pigment within. The Fitzpatrick scale is shown shown in Fig. 22.



Figure. 22. The Fitzpatrick Scale [32].

2. *Skin Cancer*

1. Basal Cell Carcinoma (BCC)

Statistics have shown that 80% of skin cancers are diagnosed as BCC, rendering it the most common type of skin cancer. The basal layer in the epidermis, which is composed of basal cells, is the starting point for the anomalous growth that results in BCC. Essentially, UV-radiation exposure from the sun, aging, among other factors, cause alterations in the DNA of the concerned cells, resulting in unrestrained tumor growth. In addition, BCC is often located on the most sun-exposed areas such as the head and the face. Most BCCs are treatable and cause negligible harm when diagnosed and treated early due to its slow progression. However, in rare occurrences it can spread into different tissues and cause dangerous complications. Typically, BCC is represented by several lesion characteristics that change the appearance of the skin and are not self-healing, such as elevated pink patches, scaly red patches, brown lesions among others [33].

2. Squamous Cell Carcinoma (SCC)

SCC is much less common than BCC, where it is estimated to comprise 20% of most skin cancer diagnoses. The SCC originates within the outermost layer of the epidermis containing squamous cells. SCC is typically located in the same regions where BCC develops, and it also shares the same set of causes, primarily attributed to UV-radiation from sun exposure. However, SCC develops and grows faster than BCC, meaning that it can possibly spread into other parts of the body more quickly, leading to dangerous complications [34].

3. Melanoma

Melanoma skin cancer is the most dangerous of the aforementioned cancers. This is due to its aggressiveness in rapidly spreading into other tissues. Melanoma originates from the mutation of Melanocytes, the producers of Melanin, in the epidermis, which is the pigment that gives skin its color. Although the exact causes of Melanoma are not fully known, a combination of multiple factors such as UV radiation and genetic predisposition are attributed as potential causes. Unlike other skin cancers, Melanoma does not only develop on sun-exposed areas, but also in places like the soles of the feet, mouth, and the digestive tract. Generally, Melanoma is represented by changes in present moles or the birth of unusual growing lesions on the skin [35]. Fig. 23 illustrates the aforementioned cancers on skin.

D. Interaction of EM Waves with Skin Lesions

Throughout the literature, it is concluded that an increased water content in malignant tissues is highly correlated with the dielectric variations at sub-GHz

frequencies, which is identified through dispersion analysis [36].

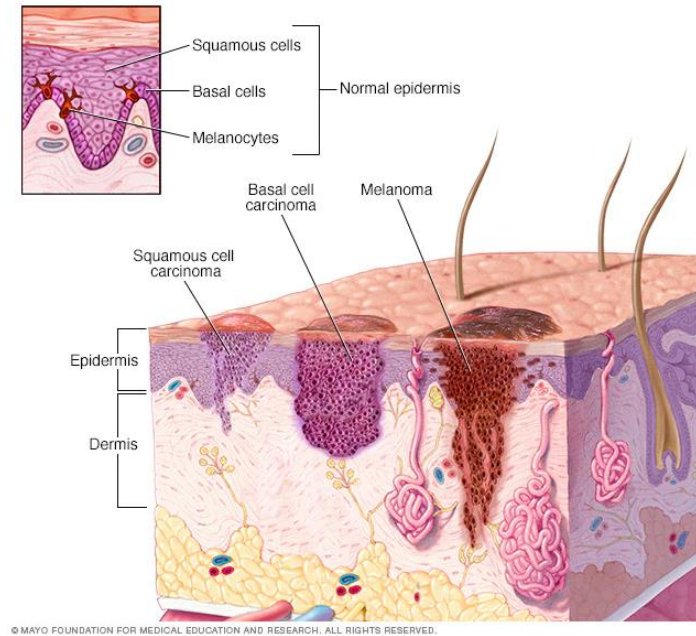


Figure. 23. Illustration of BCC, SCC, and Melanoma [37].

For example, in [17], the dielectric properties of freshly excised healthy and malignant tissues are characterized at an ultra-wide bandwidth. Fig. 24(a) shows the measurement setup and a piece of excised skin to be used in the characterization experiment. After analyzing the dielectric properties of these excisions, the study concludes with the existence of statistically significant differences in the dielectric properties of malignant and healthy tissues. Fig. 24(b) shows an overlapped plot of the real and complex permittivities of healthy skin, BCC, and SCC, with clear differences shown between them. It is also concluded that water content within BCC and SCC was the primary cause of variation in the dielectric properties.

Furthermore, the work presented in [10] also illustrates the powerful ability of EM waves to differentiate between healthy and malignant tissues by relying on a ultra-

wideband synthetic imaging system, as shown in Fig. 25. The system is tested on excised BCC and SCC cancers, and is able to differentiate between cancerous and healthy skin based on their electromagnetic reflectivity, as summarized in Fig. 25.

Finally, several publications have had the similar goal of characterizing tissues at a wide range of frequencies such as [6], [17], [26], [36], further illustrating the interaction between healthy and anomalous tissues. A comprehensive list of dielectric properties and models can be obtained from [25]-[27].

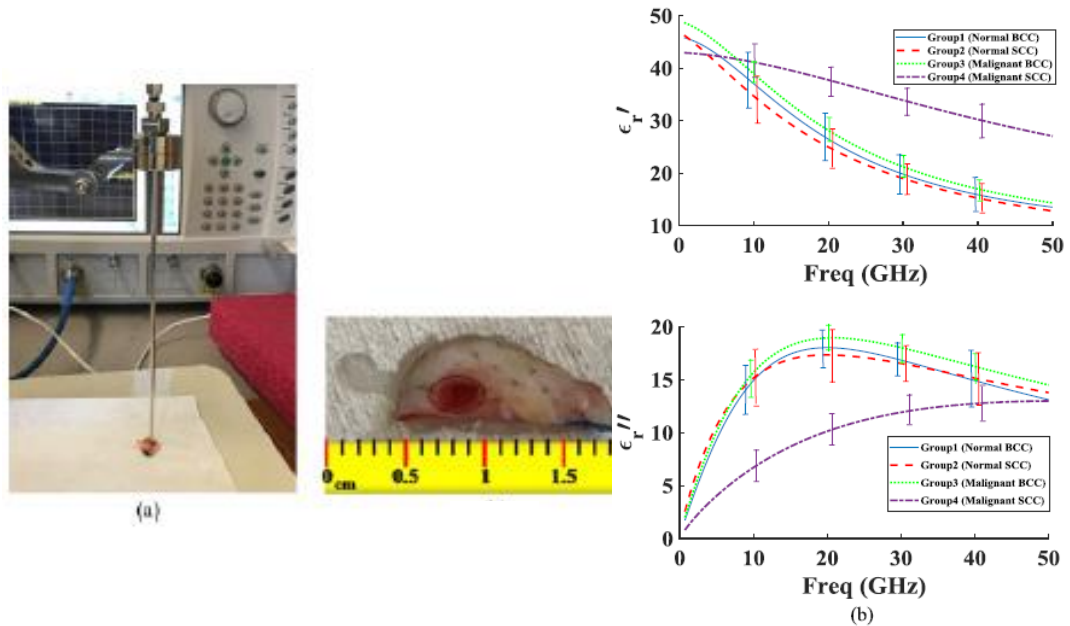


Figure. 24. The test setup in [17], and the corresponding measured permittivity values of BCC, SCC, where (a) shows the real part, and (b) shows the complex part.

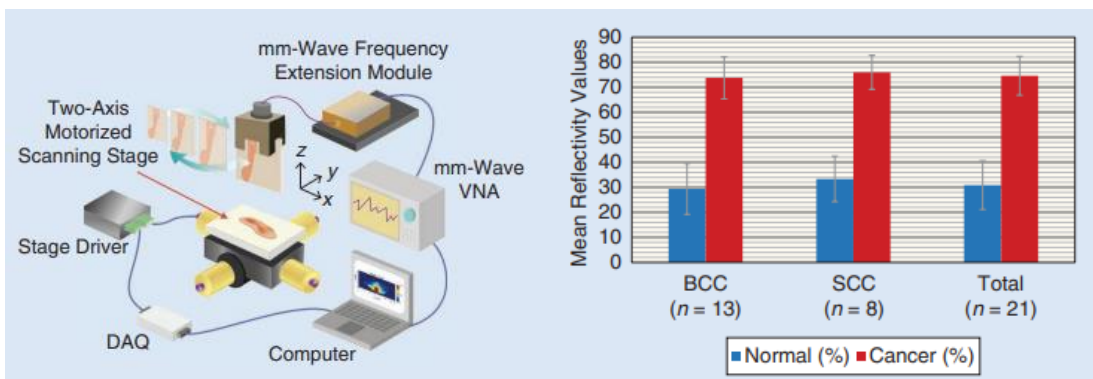


Figure. 25. System overview and obtained results [10].

E. Discussion

The complex permittivity, an electrical property that explains how an applied electric field interacts with a material, is the fundamental concept behind EM-based material sensing. Based on the plethora of research within the literature, it is shown that the complex permittivity of healthy skin is different than that of a diseased skin. This difference can be quantified using the right equipment and techniques to ultimately predict whether a suspected lesion is cancerous or healthy. This conclusion forms the basis of this study. It also highlights the fact that designing a tailored RF-based solution can produce an impactful and clinically practical non-invasive skin cancer detector. Such a device reduces the patient's discomfort and improves the throughput and accuracy of a medical professional.

CHAPTER IV

TECHNIQUES FOR DIELECTRIC CHARACTERIZATION

A. Introduction

As discussed in Chapter III, materials have different electromagnetic properties based on their composition. In the literature, many techniques have been introduced with the common goal of characterizing dielectric materials. By characterizing different materials, we are obtaining the permittivity and loss tangent. Observing changes in these properties provides important insight on the nature of the specimen under test. In our case, the variations are in skin permittivity, which is necessary to distinguish whether a skin lesion is healthy or anomalous [6], [10], [19]. To achieve characterization, different methods that share similar fundamentals exist within the literature. Generally, most of these techniques depend on the effects of perturbing the EM field within a microwave structure, which invokes a direct effect on the measured S_{11} , the Q-factor, and the frequency of operation of the used microwave structure [24]. These dielectric characterization techniques include Reflection methods, Reflection and Transmission methods, Resonator methods, and Resonant-perturbation methods [24]. The focus of our proposed study is on planar resonator methods that utilize the concept of resonant perturbation. This decision is motivated by the inherent compactness of planar structures, their convenient integration with different devices and circuits, and their enhanced sensitivity. Planar methods utilize microwave structures that are of planar nature, primarily composed of microstrip-based structures such as transmission lines (TLs), TL-based resonators, and TL-based antennas. When an electromagnetic wave propagates from one medium to another with different EM properties, portions of the wave are reflected and transmitted, as shown in Fig. 26. By measuring the amount

of reflection or transmission, one can deduce the electrical properties of the MUT. The typical method of performing dielectric characterization depends on reflection methods that utilize coaxial probe kits, which is hailed as the gold standard for dielectric characterization over wide frequency ranges. However, this method requires bulky hardware that is often very expensive [38]. An example of a dielectric probe kit with the required VNA is shown in Fig. 27.

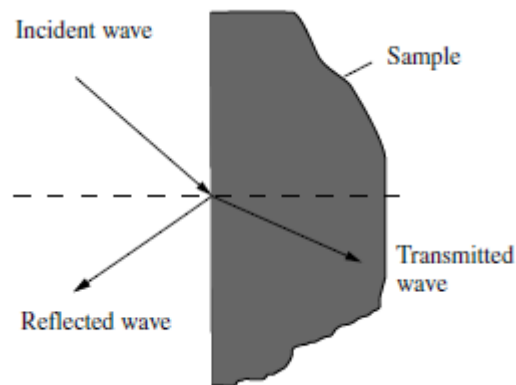


Figure. 26. Wave at a boundary from [24].



Figure. 27. A typical dielectric characterization kit with a VNA [38].

B. Planar Non-Resonant Methods

Non-resonant methods, as the naming suggests, employ TL-based structures that do not resonate, such as open-ended or short-circuited TLs. These methods include two sub-categories: Reflection and Reflection/Transmission methods, and they are discussed in the following sections [24].

1. Reflection Methods

To characterize the properties of a MUT using the reflection method, the MUT itself is prepared in a way that allows it to fit as a substrate for a microstrip transmission line where it is sandwiched between two conductors, as shown in Fig. 28(a). Then, the MUT's properties are extracted from the TL's changing reflection properties which are typically measured by a VNA. This technique is quite challenging since it requires precise sample preparation and fabrication [24].

2. Transmission/Reflection Methods

In this method, the MUT is placed on top of a transmission line as shown in Fig. 28(b). To obtain the dielectric properties, both the reflection coefficient (S_{11}) and the transmission coefficient (S_{21}) are measured. The material properties can then be calculated through numerical procedures and full-wave analysis [24].

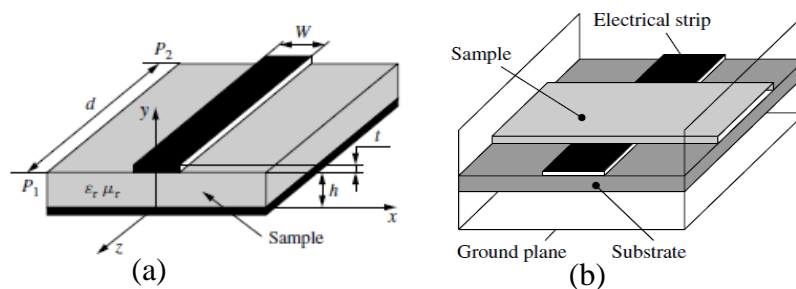


Figure. 28. Transmission Line and loaded transmission line from [24].

C. Planar Resonant Methods

Resonant methods utilize resonating structures to characterize material properties. The primary principle of operation relies on the changes in the frequency of resonance and the Q-factor upon loading the structure with the MUT, thereby forcing loading effects that perturb the structure's EM field distribution. Two examples of such resonating structures are discussed below [24].

1. The Planar One-Port Resonant Probe

This structure utilizes a one-port planar resonator and it operates based on the resonant perturbation theory, where a MUT is placed within the near-field region of the structure. When the MUT is placed within the resonator's illumination region near its open end, as shown in Fig. 29, the EM fringing fields emanating from this aperture will be disturbed due to the presence of this MUT. Consequently, the resonant frequency, the S_{11} , and Q-factor will change, thereby reflecting the properties of the MUT. Essentially, the probe can be modeled by a resonant LCR circuit, as shown in Fig. 30(a). When the probe is loaded with a MUT, the LCR model is augmented by a capacitor or an inductor that represent the loading effect of the MUT, as shown in Fig. 30(b).

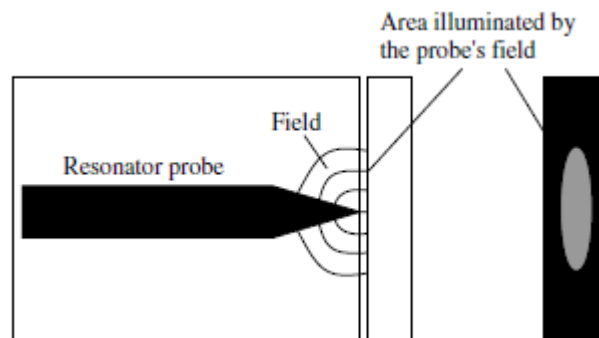


Figure. 29. Near-field probe from [24].

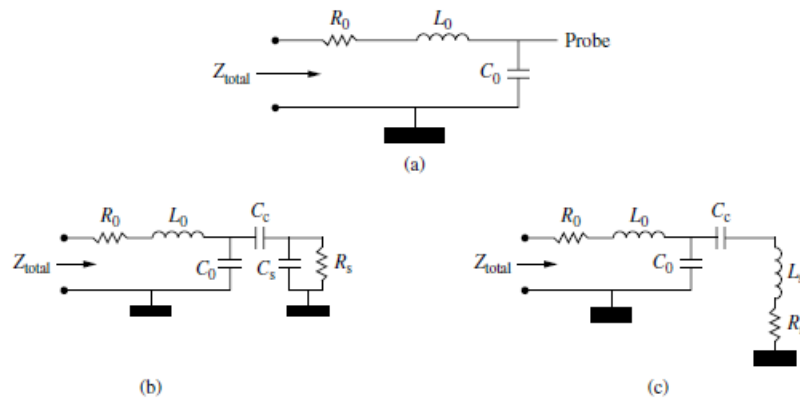


Figure. 30. Circuit models from [24].

In addition, the length of the resonant probe dictates its frequency of operation, and this fact is crucial for understanding the penetration depth of the resulting evanescent fields that emanate from the open-end. This depth determines the maximum distance at which a buried specimen can be detected. The general rule is, the lower the frequency, the deeper the field penetration, and vice versa, as illustrated in Fig. 31 [24].

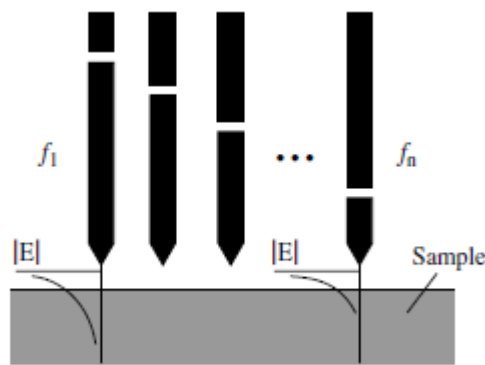


Figure. 31. Effect of frequency on penetration depth in [24].

2. The Ring Resonator

Ring resonators are two-port microstrip-based ring-shaped resonators that follow specific length requirements that dictate their operational frequency. Fig. 32 illustrates a typical gap-coupled ring resonator used in dielectric characterization. In this topology,

the MUT is placed directly on top of the ring resonator, fully covering it. After introducing the sample, numerical methods are used to relate the resultant shift in the resonator's resonance frequency to the MUT's dielectric properties [24].

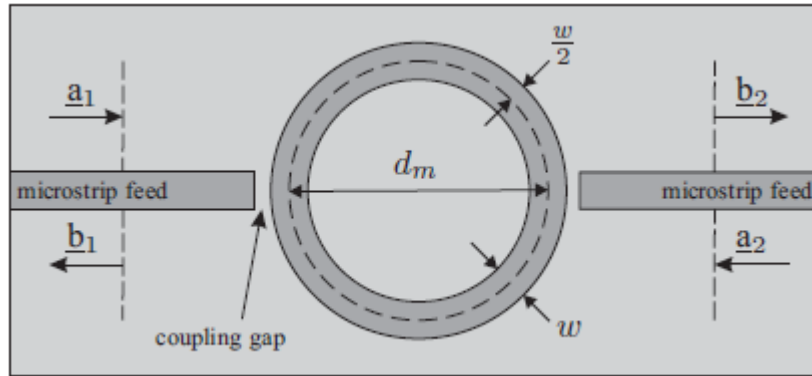


Figure. 32. Ring resonator from [24].

3. *The Ribbon Resonator:*

As shown in Fig. 33, a ribbon resonator consists of a half-wave length resonator that is fed by gap-coupling. Similar to the ring resonator case, the MUT can be used as the resonator's substrate or it can be used to directly load the resonator. The change in the resonant frequency leads to the estimation of the MUT's dielectric constant .

However, the presence of the coupling gaps adds extra EM field fringing that effectively changes the electrical length of the resonator, a change that must be taken into account to obtain maximum accuracy. A typical solution is to use two ribbon resonators operating at different resonance frequencies, where the additional electrical length due to fringing can be cancelled out [24].

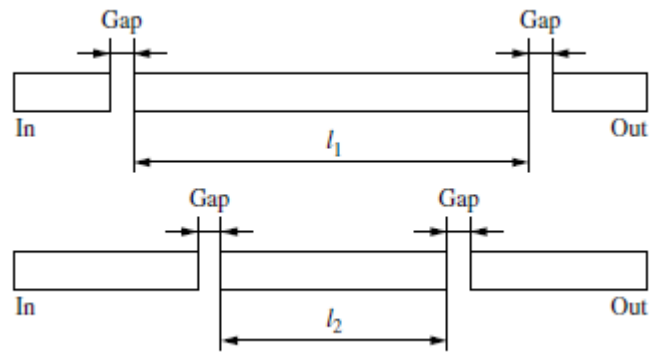


Figure. 33. Ribbon resonator from [24].

D. Discussion

Several EM structures have been introduced; however, they all share the same fundamental concept of being susceptible to the effect of the material under test on the properties of the resulting EM fields. In the grand scheme of our application, understanding the properties and physical requirements of each structure enabled us to design a sensor topology that best suits skin lesion measurements. As such, the microstrip-based resonant-type sensor topology is adopted since it can be highly compact, easily integrated within a system, and is highly sensitive to surrounding materials.

CHAPTER V

THE SKIN ANOMALY DETECTION DEVICE

A. Introduction

Our proposed EM sensing system is composed of three parts, the highly sensitive EM sensor, the wave analyzer circuitry, and the corresponding software. The EM sensor is the component responsible for sensing the dielectric differences between healthy and malignant lesions. In addition, a wave analyzer circuit must be present to perform the crucial roles of generating the high frequency signals and retrieving the waves that reflect off the skin lesion under test in order to extract the parameters that enable us to quantify the observed differences. In this chapter, we define the main parameters that we are measuring, the requirements of such a system, the EM sensor design procedure, and the wave analyzer design procedure. Additionally, the constituents of such a wave analyzer are briefly explained due to their crucial importance in understanding the proposed architecture. Finally, the proposed designs are tested, and their performance is validated in a series of tests.

B. What are we measuring? - Scattering Parameters (S Parameters)

Our measurements revolve around S parameters. In short, S parameters are quantities that describe the reflection and transmission characteristics of RF devices and sensors [39]. In our application, the main S parameter of interest is the S_{11} which is known as the reflection coefficient. As mentioned previously in chapters I, II, and III, S parameters of RF devices will change depending on the properties of a material loading the device, such as a skin lesion under test. Furthermore, the S_{11} is a complex value that

is characterized by its magnitude and phase, both of which are necessary quantities that provide significant insight within specific sensing applications

C. The Microwave Sensor

First, we must introduce a key term to our method of sensing, which is the near-field. Generally speaking, the near-field corresponds to a region of space directly surrounding a radiating structure, such as a sensor, where the EM fields are decoupled and non-propagating. The different field regions can be seen in Fig. 34 [40].

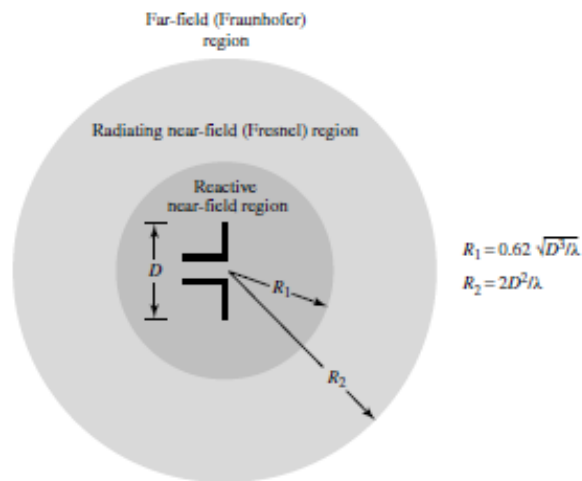


Figure. 34. Radiation regions [40].

Due to the varying dielectric properties of skin and anomalies, there is a complex loading effect to the radiating structure, which leads to changes in S-parameter magnitude, phase, and resonance frequency. It is this process through which we can acquire information regarding a specific tissue [24].

The objective herein is to design a sensor that is highly sensitive, compact, cost-effective, and tailored for skin anomaly detection.

1. Preliminary Microwave Sensor Design

In this section we propose a microwave sensor design based on a capacitively-coupled microstrip half-wavelength resonator. The proposed sensor is distinguished by several attractive features such as a simple planar topology, compactness, enhanced sensitivity, and its naturally high quality-factor due to its patch antenna resemblance [40]. This sensor is composed of a feeding line, a matching network, and the resonant element. The sensor is designed using the Ansys Electronics Desktop electromagnetics simulator [41]. Additionally, the sensor utilizes a 0.79 mm thick RT Duroid 5880 substrate with a dielectric constant of 2.2. In this topology, the resonant element is designed to resonate at 5.73 GHz, which corresponds to an optimized resonant element length of 21 mm. In addition, the resonant element is 1 mm wide, which corresponds to a line impedance of 85 ohms that subsequently tapers to a 2 mm long, 0.2 mm wide, line that corresponds to 100 ohms. By adopting a narrow resonant element width, we significantly increase the quality factor of the sensor [18], [42]. The higher quality factor allows for the observation of shifts in frequency more clearly due to the narrow bandwidth. Both are crucial features when the sensor is employed in a dielectric characterization application, which assure higher measurement resolution and enhanced sensitivity to the properties of the MUT. Additionally, the narrower section at the sensor's tip increases the density of E-fields at this location, which equivalently increases the strength of the evanescent fields fringing from the sensing tip. This will be crucial in discerning the dielectric differences between healthy and cancerous lesions beneath the tip.

Furthermore, the narrow resonant element results in a high input impedance [39] which necessitates the design of an impedance matching section that transforms the

sensor's impedance to the standard 50 ohm impedance at the input. Consequently, the resonant element is fed using a capacitive coupling gap and a 5 mm microstrip line with an 85-ohm characteristic impedance. The capacitive coupling gap behaves as a lumped element capacitor with a limited range of small capacitance values. Lumped elements, when compared to distributed elements such as microstrip-based solutions, are known to increase the quality factor of a system due to their inherent narrow bandwidth effects.

The sensor is shown in Fig. 35(a), and the generated E-field across its resonant element is plotted in Fig. 35(b), which verifies that the maximum E-field intensity is at the designated tapered sensing tip. Fig. 35(c) illustrates how a specimen under test (SUT) will be placed beneath the tapered tip of the sensor. In addition, Fig. 35(c) also illustrates a projection of the E-field emanating from its tip, which verifies that the maximum sensitivity (highlighted in red) is focused directly beneath the sensing tip. Finally, the sensor is fabricated as shown in Fig. 36, then measured using the Keysight N9923A Fieldfox VNA [43]. Furthermore, excellent agreement is obtained between the measured S_{11} and the simulated one, as shown in Fig. 37.

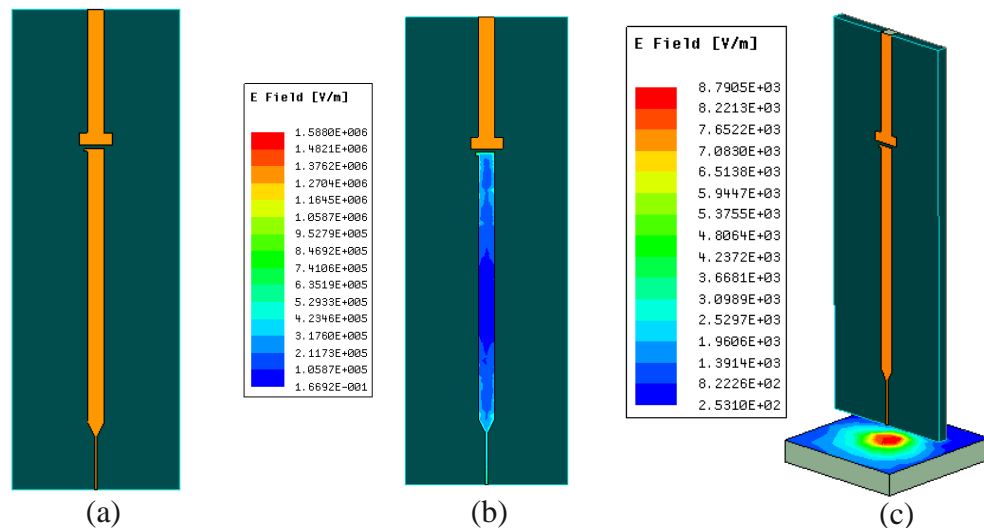


Figure. 35. The proposed EM Sensor.



Figure. 36. The fabricated sensor.

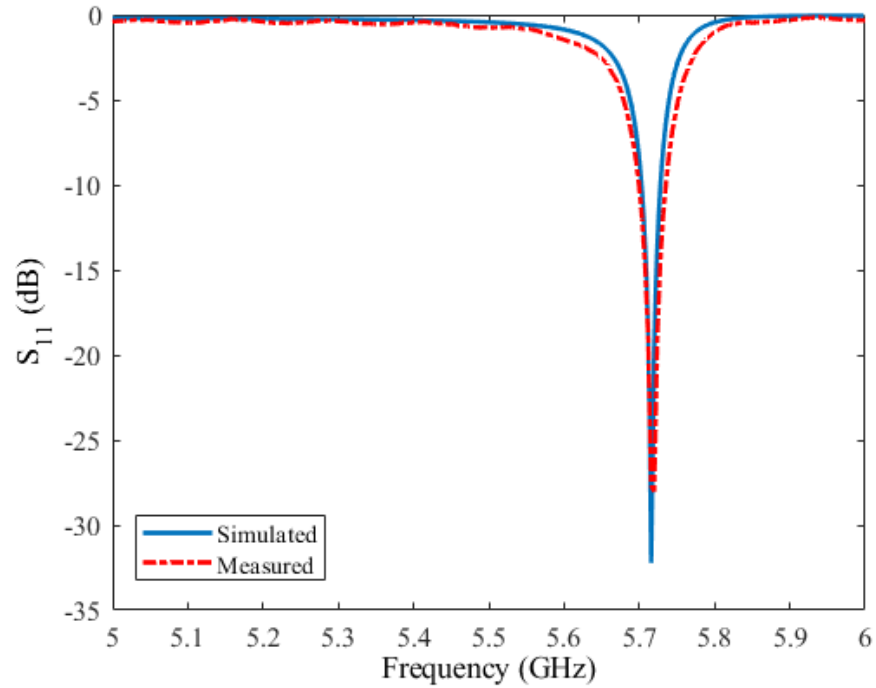


Figure. 37. The measured and simulated S_{11} of the proposed sensor.

2. The Improved Microwave Sensor

Despite the high quality factor of the designed sensor in the previous subsection, several key challenges related to performance, sensitivity, and usability were identified upon employing the sensor in a real-world practical application. These challenges are

categorized into skin lesion sensitivity issues, susceptibility to environmental noise, and impractical stand-off requirements. Each of these challenges are discussed in the consequent subsections.

a. Sensitivity

Center to the functionality of a microwave sensor specifically designed for skin lesion diagnosis is its ability to discern between cancerous and healthy skin lesions accurately and practically. The previously designed microwave sensor relied on the evanescent fields that reside between the very narrow conductive tip and the ground plane, as shown in Fig. 38. After its evaluation, two main problems related to sensitivity were detected. First, upon the placement of a SUT beneath the sensing tip, the sensor exhibited low sensitivity, which was depicted by the minor changes in the S_{11} response. This is attributed to the small area in which the evanescent fields reside, especially that the conductor of the resonant element is extremely narrow, which reduces the effective EM-field density that is capable of interacting with a SUT. A second factor attributed to the low sensitivity is due to the microstrip nature of the sensor, wherein the EM fields in such a structure are not solely confined to the sensing tip. In fact, the bulk of these fields is concentrated within the substrate, situated directly beneath the resonant element, as illustrated by the straight red lines in Fig. 38. Additionally, a significant portion of these fields fringes through air and into the substrate around the resonant element, as illustrated by the red curves in Fig. 38. The second sensitivity-reducing impediment is the crucial dependence on short stand-off distance, which is the separation between the sensor's tip and the SUT. This is a consequence of the low evanescent field density in a miniscule sensing area, which requires SUTs to be placed within a few micrometers away from the sensing tip. Such short stand-off distance

renders the sensor highly impractical and significantly prone to errors originating from movement and pressure during measurements. These factors emphasize the adoption of new measures that enhance the sensitivity of such sensors.

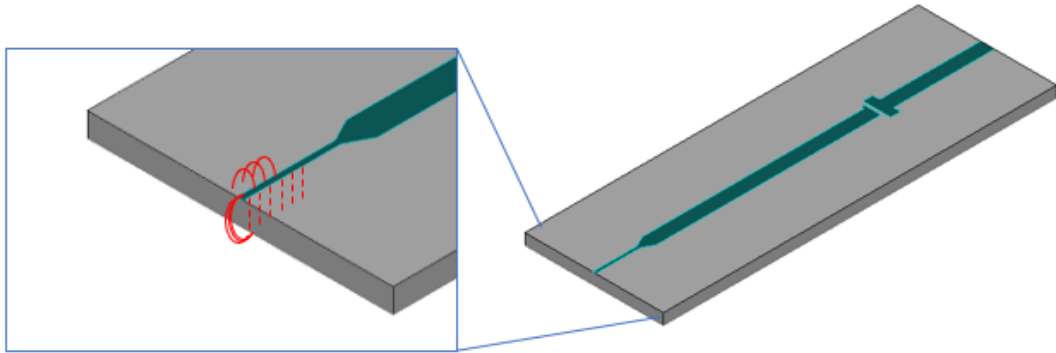


Figure. 38. EM field locations at the sensor's tip.

b. Environmental Noise

When designing a sensor that will be hand-operated at conditions that are far from a controlled laboratory setting, one must take several critical factors into consideration. Primarily, the proximity of different materials, such as the hand of the operator or a SUT, to undesired regions on the sensor leads to unwanted loading effects that cause erroneous measurements. Not only that, ambient radiation from different RF sources common in public places, such as mobile phones and WiFi routers, can also introduce noise into the system, potentially compromising the fidelity of the measurements. The previous sensor, being essentially an unshielded radiator, was particularly susceptible to the aforementioned problems.

c. Physical Nature of Skin

Understanding the physical nature of the specimen subjects of this application, namely the human skin, must also be taken into consideration. Skin is elastic and flexible, and knowing that the proposed sensors are composed of stiff materials that will

be pressed against it, a sinking action will occur. This slight sinking of the sensor into the skin will expose the sensitive tip to an area larger than the boundary of the skin lesion, which contributes to reduced sensitivity. This emphasizes the need for a proper structure that not only ensures a fixed distance from the skin, but also preserves its flatness.

d. Sensor Design

In order to tackle the aforementioned challenges, a new sensor is developed. The improved sensor adopts some of the elements from the previous sensor's design due to their convenience, while introducing new features that overcome the shortcomings of the previous one. As such, the improved sensor adopts a similar half wavelength resonator as its sensing element that operates at 4.75 GHz. This sensor is designed on an RT Duroid 5880 substrate having a dielectric constant of 2.2 and a thickness of 0.79 mm. Furthermore, two main sections comprise this sensor, a matching network and the resonant element. First, the resonant element is characterized by its length, 19.825 mm, corresponding to an optimized half wavelength at 4.75 GHz, as well as its narrow width of 1 mm, corresponding to an 85-ohm characteristic impedance.

To overcome the sensitivity challenges, a solution is devised in which part of the resonant element and its emanating fields are actively involved in the sensing procedure, representing stronger and denser EM-fields at the sensing tip. This solution is implemented by extending the length of the resonant element and connecting it to a hemispherical sensing tip of 1.3 mm radius. This connection is achieved by means of a via through a cylindrical substrate of 6 mm radius and 0.79 mm thickness, as shown in Fig. 39. This hemispherical tip will emanate stronger evanescent fields around it when compared to the evanescent fringing field from the previous sensor that lacked the resonant extension. Fig. 40(a) shows the E-field concentration along the resonant

element, while Fig. 40(b) shows a tilted view of the sensor that highlights the increased concentration of the E-field at the hemispherical tip. Additionally, the hemispherical tip is optimally chosen to suit the measurement of skin cancers which are typically larger than 1 mm. In Fig. 40(c), the EM illumination region of the sensor is shown, where the red projection illustrates the maximum sensitivity region, which is directly beneath the tip. Consequently, when the sensor is positioned directly above a SUT, the interaction of the electromagnetic field with the specimen under test is maximized.

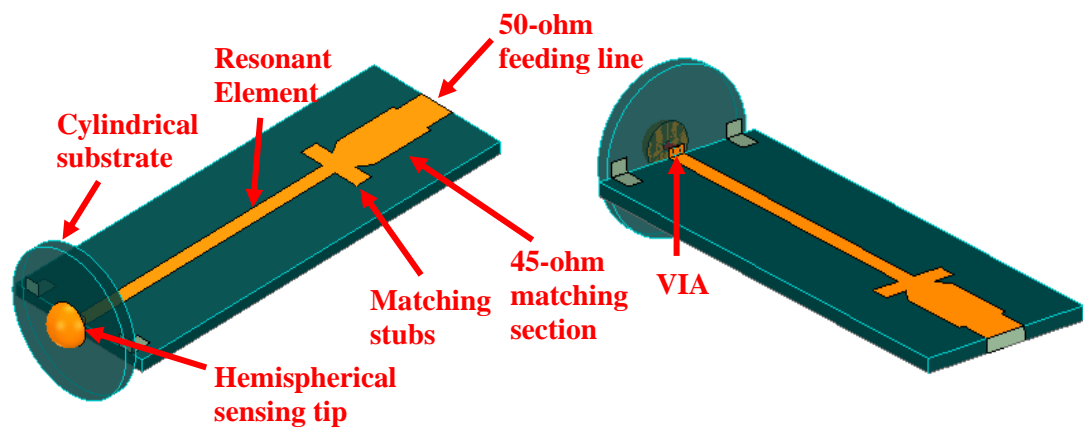


Figure. 39. Topology of the improved microwave sensor.

Such necessary modifications to the sensor's topology will enable a clearer observation of the dielectric differences between lesions, a more practical stand-off distance of 2 mm, and the full inclusion of the suspected lesion in the sensing procedure without incorporating unwanted adjacent lesions into the measurement.

Furthermore, a metallic shield is designed to the dimensions of the sensor, which, fundamentally, is a conductive enclosure that prevents sensing from undesired regions and mitigates the introduction of ambient RF noise into the system. This enclosure also includes a cutout at the sensing tip of the sensor, where desired sensing will be performed at the tip. Fig. 40(d) shows the sensor within its metallic enclosure. In

addition, the enclosure includes a partition that accepts a 2 mm-thick cylindrical foam spacer that fixes the distance between the sensing tip and the SUT according to this thickness. Furthermore, the topology of this shield enables us to preserve the flatness of the underlying skin when placing the sensor on a skin lesion. A typical sensing scenario including the sensor and an SUT is shown in Fig. 41.

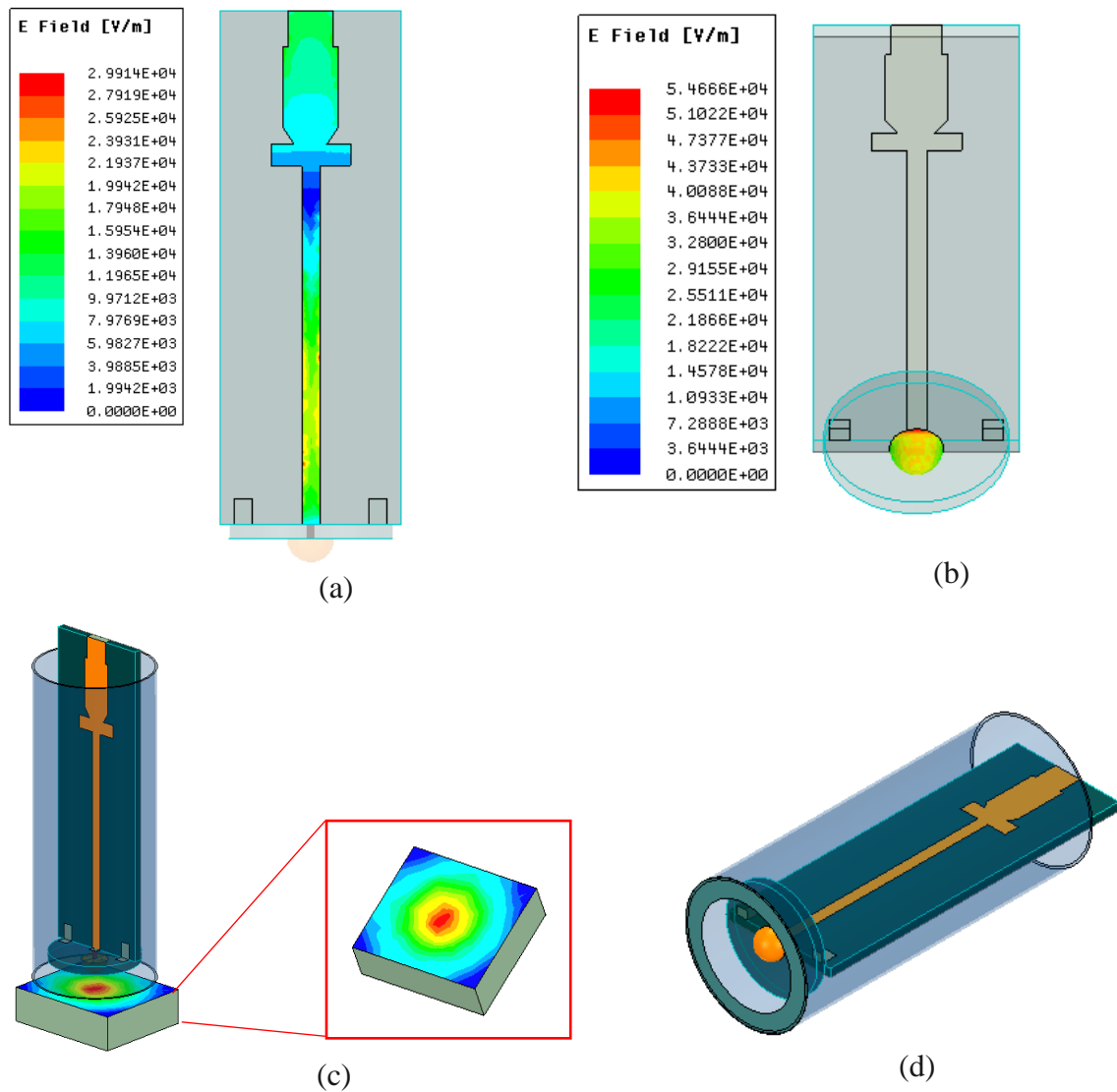


Figure. 40. (a) E-field distribution along the resonator, (b) along the hemispherical tip. (c) E-field projection on a SUT. (d) The enclosed sensor.

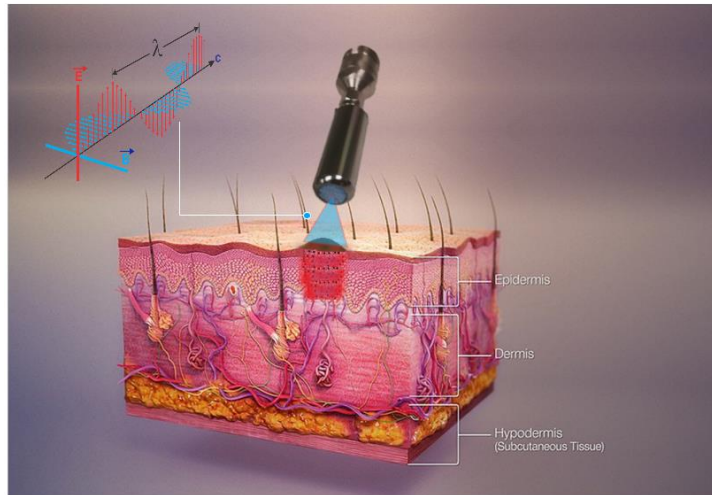


Figure. 41. An illustration of a typical sensing scenario. The figure is modified from <http://www.scientificanimations.com/wiki-images/>.

e. Impedance Matching

The narrow width of the resonant element within the proposed sensor will result in a high input impedance [39], which must be transformed to 50 ohms in order to achieve a good impedance match between the feeding structure and the sensor. Not only that, the presence of the conductive shield enclosing the sensor must also be accounted for during simulations to obtain maximum accuracy. As a result, a matching network is designed between the resonant element and its 50-ohm input. This matching network comprises a 43.5-ohm microstrip line of 4.5 mm in length that is then connected to an open stub having a characteristic impedance of 32.8 ohms and a length of 1.2 mm. Furthermore, triangle-like cutouts are made from the 43.5-ohm line to better optimize the overall impedance matching.

f. Performance

This sensor is fabricated, then measured by the Fieldfox VNA [43] to validate its performance. The measured and simulated S_{11} are in excellent agreement, as shown by the overlapped plots in Fig. 42. Finally, the sensor is fitted within its enclosure, as shown in Fig. 43.

g. Safety and SAR Analysis

The proposed sensor operates within the microwave region, a non-ionizing portion of the EM frequency spectrum [39]. This ensures the safety of our method, which does not pose any of the health risks associated with ionizing radiation, such as X-rays [44]. Furthermore, the Federal Commissions Committee (FCC) adopts certain standards and requirements to regulate the emission levels of radiating structures to mitigate any health risks, such as the ANSI/IEEE C95.1-1992 [45]. Accordingly, the FCC limits the Specific Absorption Ratio (SAR) – a measure of the amount of RF energy absorbed by human tissues – from wireless devices, to 1.6 W/Kg. The proposed sensor operates at -15 dBm, where a peak SAR of 0.1 W/Kg is obtained, well below the recommended limit.

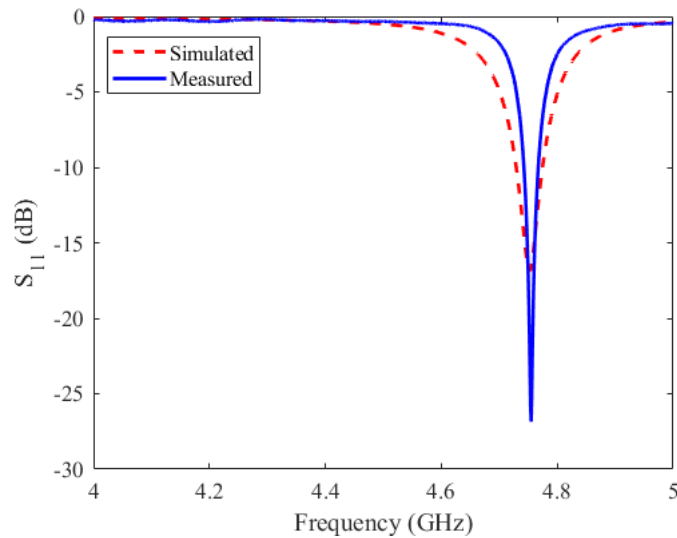


Figure. 42. The simulated and measured S_{11} of the proposed sensor.

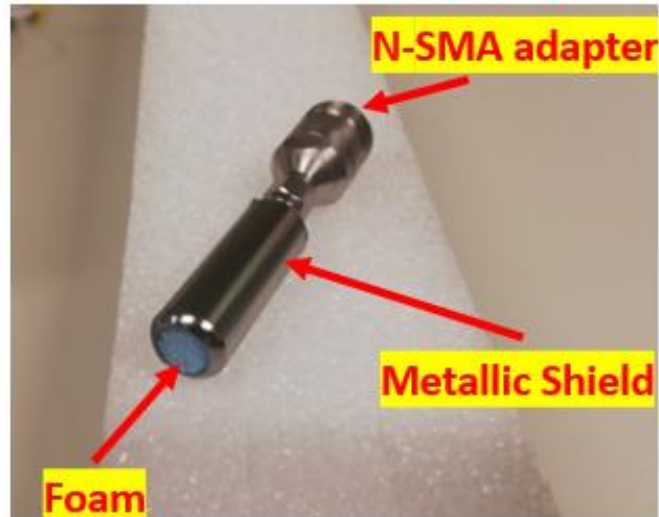


Figure. 43. Photograph of the assembled sensor within its enclosure.

D. Backend Analyzer Circuit

An EM sensor is the front-end of a sensing system that interacts with an MUT; however, it cannot operate on its own. The second crucial part of the proposed sensing system is the backend wave analyzer. This wave analyzer will handle the generation of the stimulus signals sent to the sensor at the front-end, analyze the reflected signals in the sensing procedure, extract the magnitude and phase of the S_{11} , and perform the required input/output (IO) operations to record and process the obtained data.

The objective herein is to design a custom, portable, compact, and cost-efficient analyzer that operates from 2.3 GHz to 6 GHz that will seamlessly connect to the proposed sensor. This wave analyzer will perform the reflection coefficient measurement duties that a typical VNA would do, only at a fraction of the cost, with extreme miniaturization, and the ability to run custom software that suits the application at hand.

Before leaping into the architecture and design of our custom analyzer, it is essential to gain an appropriate understanding of the typical microwave structures that

constitute such a system. The following section will briefly introduce the functionality of each of these components.

1. Microwave Structures

a. Directional Coupler

The directional coupler is a four-port network used to couple a fixed amount of an incident wave or a reflected wave traveling in one direction. By looking at Fig. 44, we can see that the input power is supplied through Port 1, and a portion of this power is coupled to Port 3 by a factor that dictates the level of coupling. Port 2 is the through port, where most of the power is transmitted to a load, and Port 4 is an isolated port which ideally should not receive any power from Port 1. In analyzer circuits and VNAs, the directional coupler is responsible for sampling the incident and reflected waves to and from a device under test, e.g.: sensor, antenna. Center to the functionality of a directional coupler is the *Directivity*. *Directivity* dictates the ability of a directional coupler to isolate the undesired reflected signals from the coupled port. Having a directional coupler characterized by a good directivity is necessary for the accurate functionality of an analyzer circuit, since lower directivity values typically result in reflected signals coupling to undesired ports. This impedes the ability to accurately measure the reflection coefficient, and equivalently, results in inaccurate measurements in a sensing application [39].

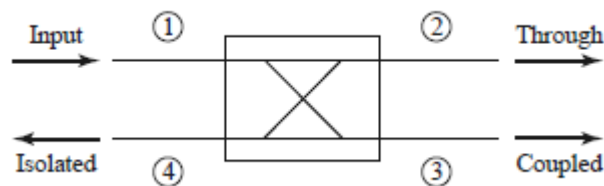


Figure. 44. Directional Coupler illustration from [23].

b. RF Amplifier

Weak RF signals, such as the ones received by mobile phones or the ones coupled from a reflected signal in a directional coupler, cannot be directly processed due to their low power. Mainly, the RF amplifier boosts such weak signals up to certain levels for appropriate processing in later stages of the RF chain. These amplifiers are characterized by their gain, which is expressed in dB [39].

c. Mixer

A mixer is a three-port device that is center to many communication applications, such as radio transmitters and receivers. The function of a mixer is to either raise (up-convert) or lower (down-convert) the frequency of a desired signal. For instance, in transmitters, the mixer receives a low-frequency baseband signal and up-converts it to the RF range for suitable communication. In receivers, the mixer receives the high frequency input signal and down-converts it to baseband for suitable digital signal processing, which is difficult to accomplish at high frequencies [39].

d. Filter

A filter is a device that, based on its configuration, allows certain frequencies to continue propagating into the system while blocking others. Different types of filters exist, such as: low-pass, high-pass, band-pass, and band-stop [39]. Utilizing filters in such systems is crucial to minimizing the interfering signals that result from harmonics or other non-linearities present within the system. These signal interferers can significantly degrade the operation of the entire system, and ultimately, prevent accurate measurements.

e. Phase-Locked Loop (PLL) and Voltage-Controlled Oscillator (VCO)

RF systems deal with signals characterized by different frequencies. The source of these signals is usually a VCO. The VCO outputs different frequencies based on the applied voltage. In more complex systems, PLLs perform the job of frequency synthesis by employing multiple VCOs to cover wider frequency ranges and ensures the phase synchronization between the input and the output of the loop [39].

2. *Proposed VNA Architecture: WaveWhisperer*

a. General Overview

The proposed analyzer system, “WaveWhisperer”, comprises the analog and digital circuitry, the code, and the algorithms that facilitate the configuration of this system and the analysis of the measured data. The functional block diagram of the proposed architecture is shown in Fig. 45. The WaveWhisperer operates as follows: A frequency synthesizer, known as the *Source*, is programmed to sweep and output a specific range of frequencies encompassing a sensor’s frequency of operation. The output of the source is connected to two directional couplers whose purpose is to couple portions of the incident and reflected signals propagating towards and from the sensor, respectively. These coupled signals are of high frequency content and must be down-converted to enable further processing. Consequently, two mixers are used to perform this action on the reflected and incident waves simultaneously. For these mixers to operate, a second frequency synthesizer, known as the *Local Oscillator (LO)* must be used to drive the LO port of the mixers. The LO produces two 180 ° out of phase outputs, where each output drives the LO port of a corresponding mixer. The source and LO frequencies are set to be 40 MHz apart, resulting in two 40 MHz down-converted

signals at the output of each mixer. The lower 40 MHz signal passes through an attenuator for amplitude regulation. Furthermore, both 40 MHz signals then pass through a low-pass filter to block harmonics and intermodulation products from propagating into the detectors. Then, each 40 MHz signal is split into two signal paths that will be connected to two detectors that accept two inputs each. As will be discussed in the following sections, one of the arms of the split 40 MHz signals must undergo a 90 degrees phase shift before being fed to the detector. Finally, the detectors output the gain and the phase of the input signals to a microcontroller that performs the rest of the digital processing.

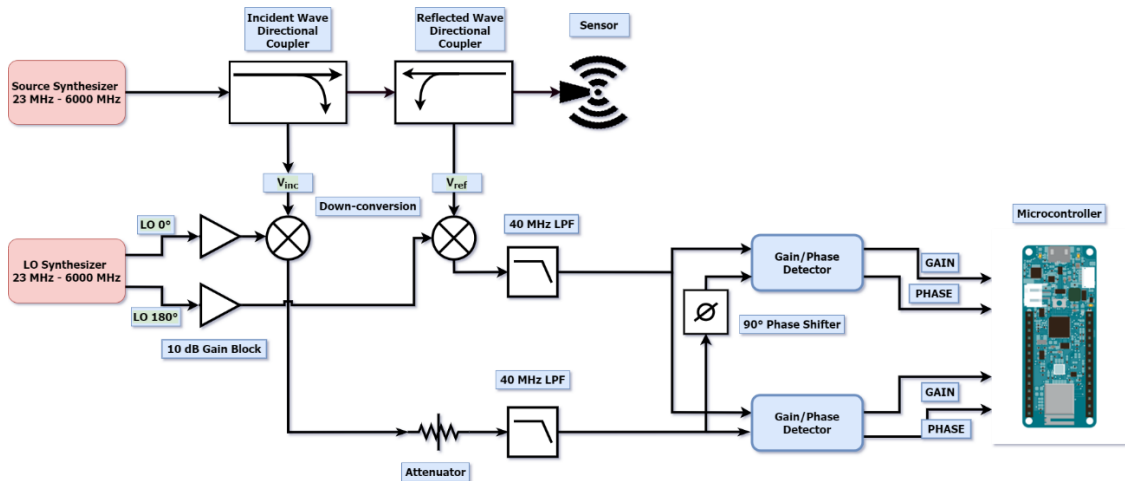


Figure. 45. A functional block diagram of the proposed analyzer architecture.

b. Component Details and Functionality

i. PLL

To generate the required frequencies that energize our proposed sensor and to perform down-conversion, two high-performance frequency synthesizers (PLLs), MAX2871 from Maxim Integrated [46] are used to fulfill the roles of the *Source* and *LO*. One of the most attractive features of this PLL is its wide output bandwidth, 23.5 MHz to 6 GHz. Furthermore, the MAX2871 is fully software programmable through a

simple 4-wire SPI interface, allowing simple configuration for the choice of generated frequency, power level, phase, among other settings. In addition, the MAX2871 has two fully differential outputs, A and B. This means that each of A and B has two ports that are 180° out of phase. The first PLL, the *Source* will be used to generate the frequencies that energize the sensor, utilizing only one output, A. The second PLL which acts as an LO, utilizes output A as a testing port to verify the intended performance, while output B's differential ports will be used as the LO signals feeding the two mixers in our architecture. To perform successful communication, one must understand the interface protocol of the MAX2871 and its underlying registers. This PLL contains seven 32-bit registers in total, six of which are write-only and one is read-only. Each register is organized in a way such that the 29 most significant bits (MSBs) are data bits while the last 3 bits (LSBs) are the register address. One of the 4 wire SPI interface logic connections, known as the load-enable (LE), controls the loading of bits into registers. If the LE is set to logic low, the data is loaded into the register MSB first. When LE is toggled to logic high, the MSBs are loaded into the register whose address is in the LSB. According to datasheet recommendations, all register values must be programmed twice with at least 20ms delay in between the writes at startup.

PLLs require an external low frequency oscillator, typically a quartz crystal oscillating between 10-140 MHz, to be connected as the reference signal. In our design, the crystal oscillates at 40 MHz. The oscillating signal coming from the crystal oscillator acts as the base frequency (PFD), thereby allowing the PLL to generate multiples of this base frequency based on integer or fractional coefficients stored in programmable registers to achieve a desired frequency. To synthesize a desired frequency, the 40 MHz signal incoming from the crystal oscillator is multiplied within

the PLL by certain factors that result in the desired frequency. The MAX2871 operates in two modes, the Integer-N and the Fraction-N modes. The Integer-N mode, as the name suggests, allows for the synthesis of integer multiples of the base frequency. On the other hand, the Fraction-N mode, enables the synthesis of a fractional multiple of the base frequency. Equation (3) governs the aforementioned operation, where F/M is zero in Integer-N mode, and non-zero otherwise. N, F, and M are the parameters of interest when synthesizing a frequency, and they represent values stored as bit sequences in different registers.

$$N + \left(\frac{F}{M}\right) = \left(\frac{f_{RFOUTA} \times DIVA}{f_{PFD}}\right) \quad (3)$$

N is the integer multiple of the PFD that results in the desired frequency, and the fractional remainder $\frac{F}{M}$ represents the fractional value resulting from the division of the desired frequency by the PFD. M is the modulus which can take values from 1-4095, while DIVA is the output divider that can take values from 2^0 to 2^7 , depending on a list of frequency ranges as shown in Table. 2.

Example A - Integer: Assume we want to synthesize a 4.8 GHz and our crystal oscillator frequency (PFD) is 40 MHz, while M is chosen to be 4000 for high resolution, then, the following procedure is followed in order to produce the desired frequency:

Get DIVA: By looking at Table. 2, 4.8 GHz requires a DIVA value of 1.

Get N: $N = DIVA \times \text{Desired Freq} / PFD = 1 \times 4.8 \text{ GHz} / 40\text{MHz} = 120$.

Since 4.8 GHz is an integer multiple (120) of 40 MHz, then the fractional mode is unneeded, hence, F/M will be 0. Finally, these values are loaded into their respective registers and the frequency is synthesized.

Example B- Fractional: Assume that we would like to synthesize 2.537 GHz, then:

Get DIVA: $DIVA = 2$, since $1500 \text{ MHz} \leq 2537 \text{ MHz} \leq 3000 \text{ MHz}$ according to Table.

2.

Get N: $DIVA \times \text{Desired Freq} / \text{PFD} = 2 \times 2.537 \text{ GHz} / 40 \text{ MHz} = 126.85$. This time, 126.85 is no longer an integer – it's a fraction. This means that $N = 126$ and F/M is the remainder = 0.85.

Get F: $F = 0.85 \times 4000 = 3400$.

These values are then loaded into their respective registers and the frequency is synthesized.

Table 2. DIVA values for different frequency ranges.

DIVA	Frequency Range
1	$3000 \text{ MHz} \leq f_{RFOUTA} \leq 6000 \text{ MHz}$
2	$1500 \text{ MHz} \leq f_{RFOUTA} \leq 3000 \text{ MHz}$
4	$750 \text{ MHz} \leq f_{RFOUTA} \leq 1500 \text{ MHz}$
8	$375 \text{ MHz} \leq f_{RFOUTA} \leq 750 \text{ MHz}$
16	$187.5 \text{ MHz} \leq f_{RFOUTA} \leq 375 \text{ MHz}$
32	$93.75 \text{ MHz} \leq f_{RFOUTA} \leq 187.5 \text{ MHz}$
64	$46.875 \text{ MHz} \leq f_{RFOUTA} \leq 93.75 \text{ MHz}$
128	$23.5 \text{ MHz} \leq f_{RFOUTA} \leq 46.875 \text{ MHz}$

The full programming sequence can be understood from the [46], and an Arduino implementation from [47] was modified to suit this application's needs.

ii. Directional Couplers

Directional couplers, which were defined previously, are used to couple the incident and reflected signals from our sensor. The directional couplers used are two

ZHDC-10-63+ units from mini-circuits [48] and they are characterized by a high directivity of 33 dB as well as a wide bandwidth of operation from 2 GHz to 6 GHz. The high directivity of these directional couplers is crucial in significantly reducing directivity errors and enabling easier calibration.

iii. Mixers

As mentioned previously, operating at very high frequencies imposes severe constraints on the hardware that can be used to process such signals. As a solution, the high frequencies are lowered in a process called down-conversion to 40 MHz using two SIM-762H+ mixers from mini-circuits [49]. These mixers are characterized by their simple passive design as well as their large bandwidth of operation from 2.3 GHz to 6 GHz.

iv. Filters:

The synthesizers, mixers, and amplifiers are of non-linear nature. This means that additional frequency components will be injected into our detectors, critically distorting our desired frequency of interest due to the inability of our detectors to distinguish between a desired and an undesired frequency. As a result, 40 MHz low-pass filters (LPFs) are designed to allow the desired low frequency to pass unattenuated while heavily attenuating the higher frequencies. Advanced Design System (ADS) [50] is used to design these LPFs, which follow the Pi topology comprising two 47 pF shunt capacitors and a 220 nH series inductor in between. The ADS schematic is shown in Fig. 46. Furthermore, Fig. 47(a) shows the obtained S_{21} of these filters and their corresponding cut-off frequencies, and Fig. 47(b) illustrates the extreme attenuation at undesired frequencies.

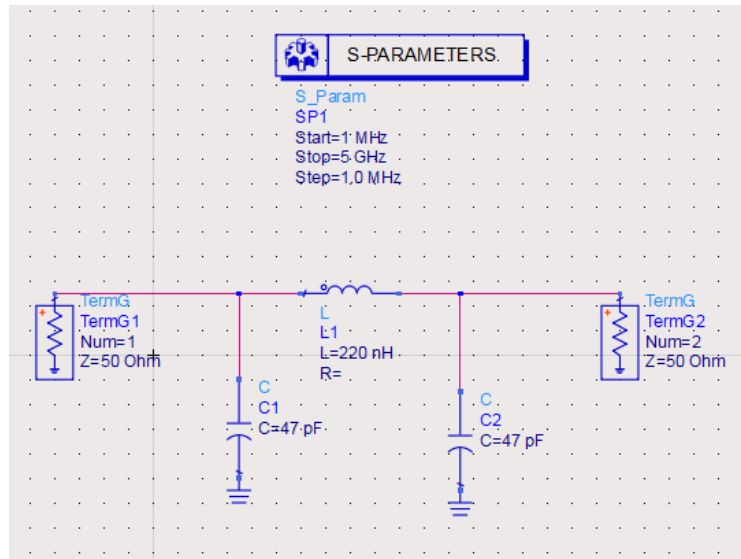


Figure. 46. ADS schematic of the 40 MHz LPF.

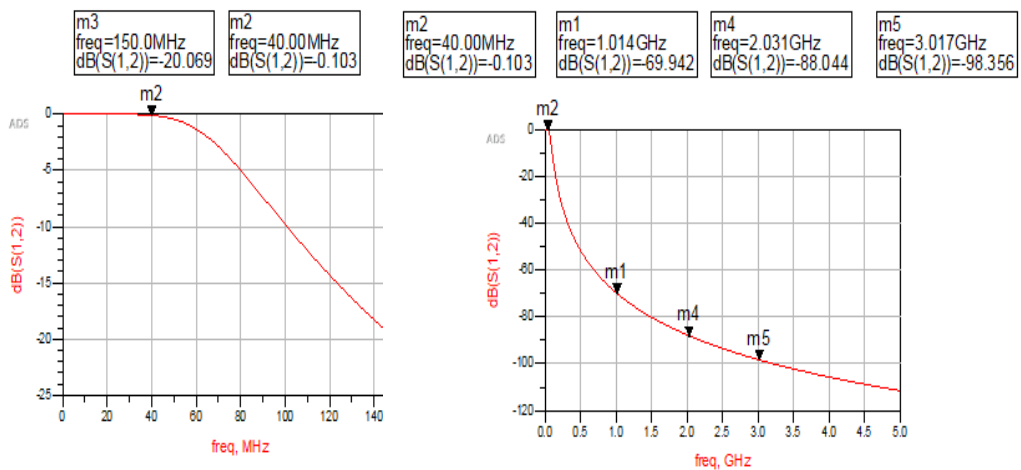


Figure. 47. Simulated results of the LPF at (a) small bandwidth, and (b) large bandwidth.

v. Detectors:

Gain and phase detectors compose the core of this system. These detectors will perform the crucial role of measuring the differences between the previously down-converted signals to produce the reflection coefficient S_{11} . The detector used is the AD8302 Gain and Phase Detector from Analog Devices [51]. Essentially, the AD8302

enables the measurement of the power gain and the phase difference between its two input signals from low frequencies up to 2.7 GHz. The magnitude of the input signals can range from -60 dBm to 0 dBm, and the AD8302 can achieve a maximum gain or loss measurement of 30 dB between the input signals. The AD8302 outputs the gain values as DC voltages across its gain pin, where the measurements are expressed as 30 mV/dB and obey the output characteristics shown in Fig. 48(a). In addition, the AD8302 measures the phase difference between the input signals from 0-180° and also outputs the result as a DC voltage across its phase pin. The phase measurements are expressed as 10 mV/degree and obey the output characteristics shown in Fig. 48(b).

Ideally, the AD8302, in conjunction with a pair of directional couplers, can perform VSWR measurements by forming an inexpensive reflectometer. However, the AD8302 suffers from two main drawbacks that prohibit its use as a network analyzer in our system. First, the frequency range of operation (DC to 2.7 GHz) is much lower than the frequencies used by our proposed sensors (4-6 GHz). The second issue is the phase ambiguity. The AD8302 measures an absolute value of the phase shift $\Delta\theta$ which falls within 0-180° without information on its sign. For example, the same DC output is common for both $\pm \Delta\theta$ phase differences as shown in Fig. 48(b). This phase ambiguity prevents the acquisition of the full S_{11} , and also impedes the necessary calibration, where the true phase must be known. Vector calibration is a powerful feature that must be present due to its effectiveness in reducing multiple types of measurement errors, and it helps in minimizing the gap between an ideal response and an uncalibrated one. These errors include: directivity errors, matching errors, line-loss, and phase mismatch.

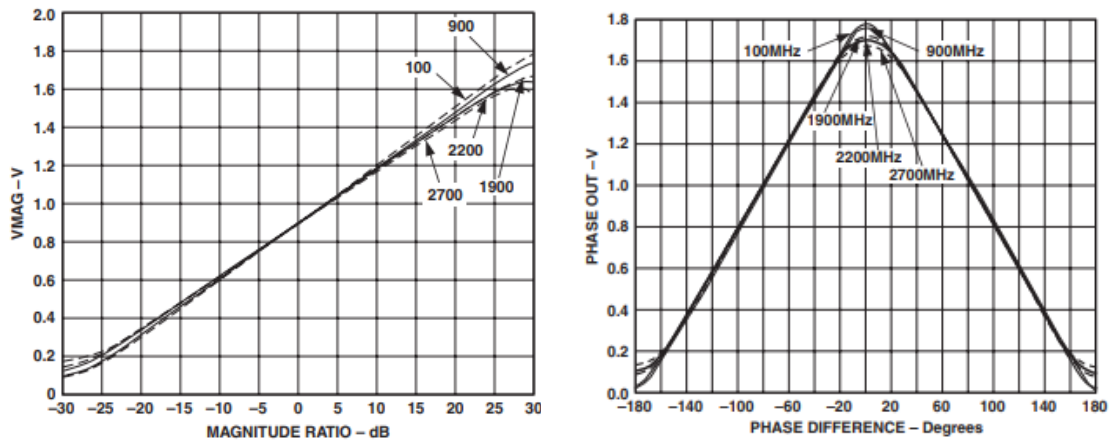


Figure. 48. The magnitude response of the AD8302 (a), and its phase response (b) [51].

Several design-level decisions are implemented to expand the frequency range of operation as well as to disambiguate the phase. To expand the frequency range of operation, it is decided to utilize a frequency down-conversion stage (composed of the previously discussed elements) that lowers the frequency of operation from a few GHz to an intermediate frequency (IF) of 40 MHz that is lower than the maximum operation frequency of 2.7 GHz. This IF is chosen carefully since the choice of frequency controls the type of hardware and interconnects between the down-conversion stage and the detectors. 40 MHz is chosen as the IF for three reasons: 1) This frequency is relatively low when compared to GHz frequencies. Hence, it simplifies the connection between the succeeding components, particularly transmission line effects such as impedance mismatch and undesired coupling between lines are almost negligible at such low frequency and short line length. 2) The design of lumped element filters at 40 MHz is simpler when compared to RF filters. In the case of lumped element filters at high frequencies, unwanted parasitics that degrade the performance of the filter will be present. On the other hand, distributed-element filters at high frequencies require more physical space and increase the risk of high frequency interference. 3) Building a filter

at such a low IF ensures the proper attenuation of all harmonics and spurs generated by the PLL and the amplifier.

As for phase ambiguity, one solution is to utilize two AD8302 units, with appropriate phase shifting at the input terminals to attain a phase-shift measurement from 0 to 360°. The two 40 MHz incoming signals representing the coupled incident and reflected signals are split into two, resulting in 4 signal lines. Each detector accepts one half from every other signal. Detector #1 will receive a reference signal and a reflected signal at its input, while detector #2 will receive a reference signal that is shifted by 90° from its original state, and another unaltered reflected signal as well. Assume we read a phase difference output of 1.5V from detector #1, as shown in Fig. 49. We cannot distinguish whether the phase difference is 45° or -45°. Then, we read the output of detector #2, which is shifted by 90°. If the original phase is -45° (point A), then detector #2 must output 1.2V (point A'), whereas if the true phase is B, detector #2 must output 0.6 V (B').

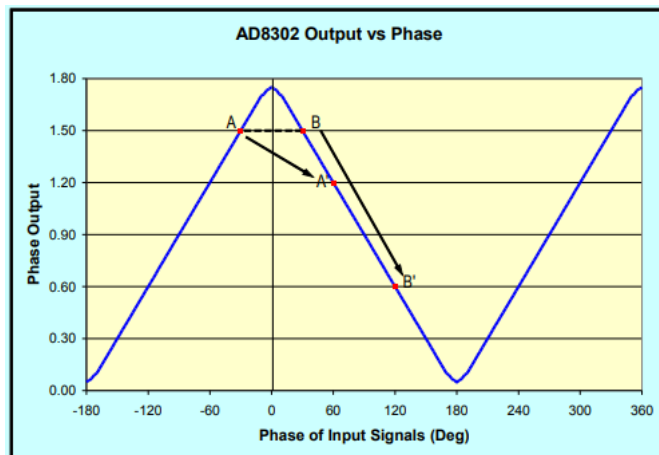


Figure. 49. The effect of introducing a 90° phase shift [52].

The aforementioned 90° phase shift is achieved by designing a T-type LPF that generates a 90° phase shifter at the desired IF (40 MHz). Fig. 50 shows the ADS

schematic of the proposed filter, Fig. 51(a) shows the phase shifter's response that allows the 40 MHz signal to pass unattenuated, and Fig. 51(b) shows the filter's phase response at 40 MHz.

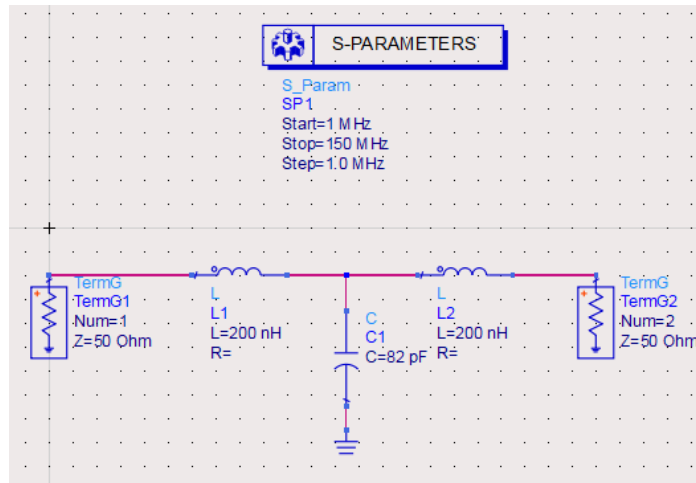


Figure. 50. ADS schematic of the 90 degrees phase shifter.

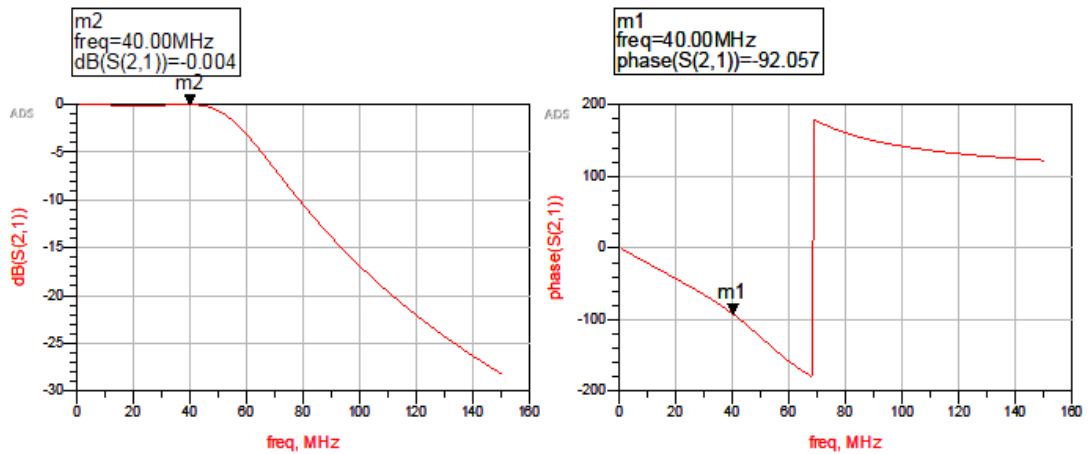


Figure. 51. Simulated performance of the phase shifter.

vi. Microcontroller

In order to communicate with the different ICs, provide power, and perform signal read-out, an Arduino Nano 33 IoT microcontroller is used [53]. This Arduino is

characterized by its compactness, suitable performance, and its wireless connectivity. In addition, this particular model supports castellated mounting holes which enable the solderability of the entire module onto the WaveWhisperer PCB, which achieves higher overall compactness.

c. WaveWhisperer Schematic

This section showcases the schematic diagrams for the WaveWhisperer's electronic circuit which is designed using the easyEDA CAD software [54]. These schematics reveal the used components, their wiring, biasing, and associated lumped components. The schematics are divided into 3 parts: Microcontroller and Power, PLL, and Down-conversion and Detection, which are shown in Fig. 52-54.

It is important to highlight that specific supply voltages are required to power the various components of the system. In our system, the microcontroller is powered by a 5V external USB supply that feeds four low drop-out voltage regulators (LDOs) responsible for creating the voltages required by the various components within the circuit. The chosen LDOs from Texas Instruments [55] ensure a stable voltage across sensitive components such as the PLL. Three of these LDOs transform the 5V into three 3.3V sources that simultaneously feed different parts of the PLL. The fourth LDO transforms the 3.3V into a 1.8V supply voltage required by the crystal oscillator.

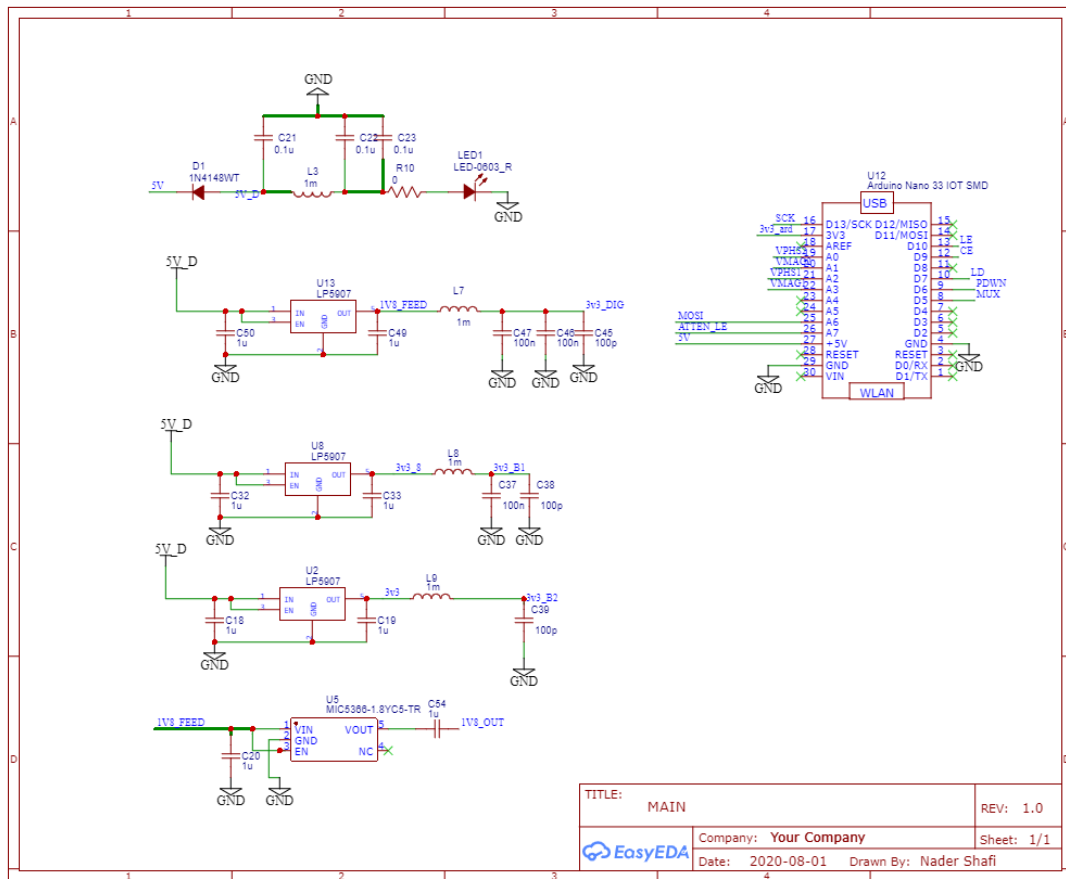


Figure. 52. The schematic of microcontroller and the power sections of the proposed architecture.

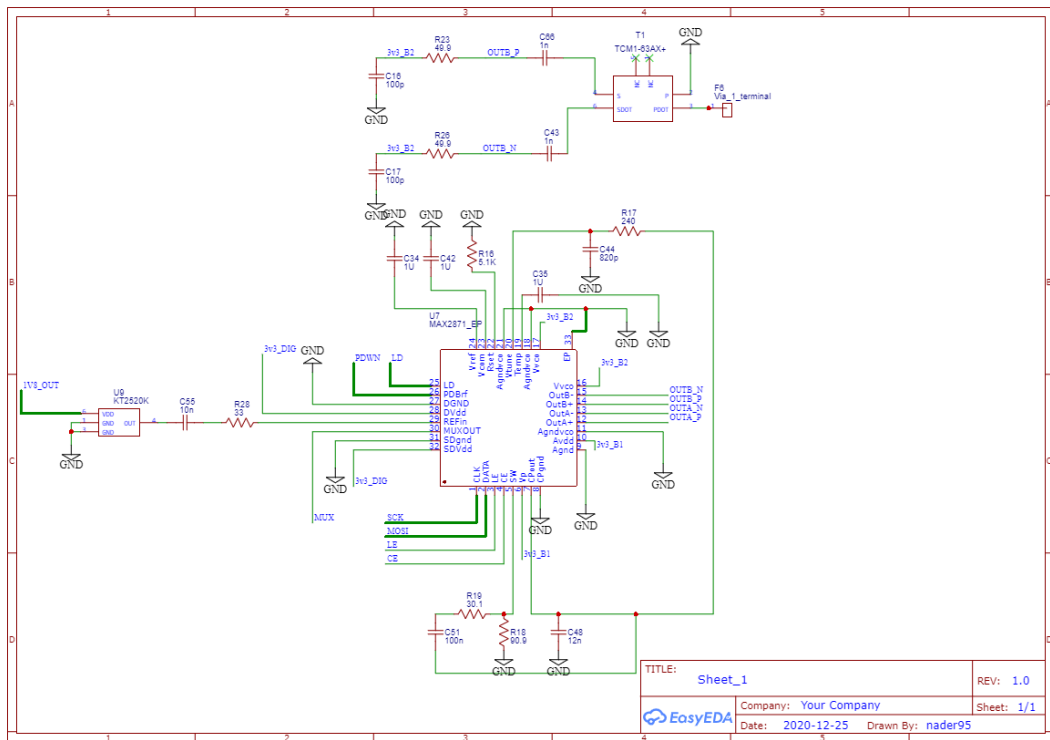


Figure. 53. The schematic of the utilized PLL.

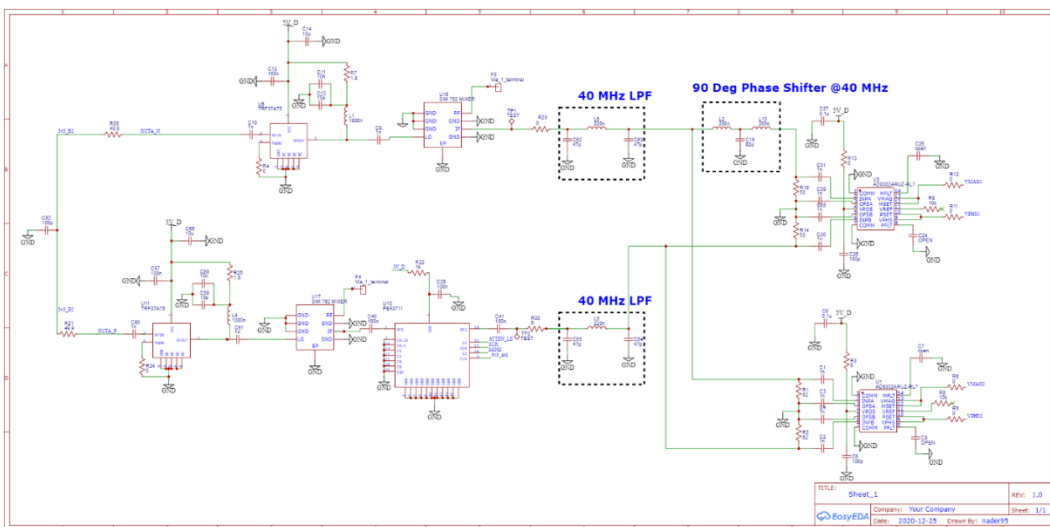


Figure. 54. The schematic of the down-conversion and detection chain.

d. WaveWhisperer Layout

After completing the schematic diagram, the layout of the printed circuit board (PCB) is then manually produced by positioning the components in their most optimal location, and then carefully routing the impedance-controlled RF traces, the digital

signal traces, and the power planes. PCBs come in many variants that are characterized by their number of layers and their dielectric material.

i. The 4 Layer PCB:

Typically, high-performance RF boards utilize multi-layer¹ PCBs such as 4 or more layers, as opposed to only 2-layer PCBs due to multiple reasons. First, multi-layer RF boards possess better isolation between the different planes, meaning that noise and undesired radiation between the power planes, high-speed signal routes, and RF transmission lines is reduced. In addition, having a multi-layer board ensures the presence of a continuous ground plane beneath transmission lines, which is necessary to maintain the characteristic impedance of these lines. Furthermore, integrated circuits (ICs) particularly at RF, typically have small packages and pins, which require very narrow 50-ohm routing lines. In a 2-layer stack-up, the thickness of the dielectric material used as well as its dielectric constant dictate relatively large line widths that complicate routing and potentially compromise proper impedance matching. The PCB of our analyzer circuit adopts a 4-layer stack-up that is commonly recommended for RF and high-speed designs. Each layer serves a designated role, as discussed below:

- **Layer 1 - RF Transmission Lines and High-Speed Signals:** This is the top-most layer at which various components are placed along with the RF transmission lines and high-speed signal lines. Layer 1 is shown in Fig. 55(a).
- **Layer 2 - Continuous Ground Plane:** An unobstructed continuous ground plane beneath the first routing layer that ensures the proper impedance control for the RF transmission lines. This layer also shields other layers from undesired parasitic coupling. Layer 2 is shown in Fig. 55(b).

¹ By layers we mean the copper planes on top of the dielectric material.

- **Layer 3 - Power plane:** This layer is reserved for constructing sub-planes that correspond to different voltages generated by the top-layer LDOs in order to power the different components accordingly. To power a component, a via is inserted between a supply trace on the top layer and the required power sub-plane on layer 3. The voltages present in this plane are 3.3V and 5V. Layer 3 is shown in Fig. 55(c).
- **Layer 4 – Signal and Ground:** This layer, through vias from layer 1, is used to route connections between the top layer components that would have been otherwise impossible or tedious to route due to the presence of other obstructing lines and components on layer 1. Layer 4 is shown in Fig. 55(d).

An additional view of the top layer that includes the corresponding copper mask and silkscreen is shown in Fig. 56. A 3D CAD rendering of the top and bottom layers is shown in Fig. 57. Furthermore, an exploded view of the multi-layer PCB is shown in Fig. 58.

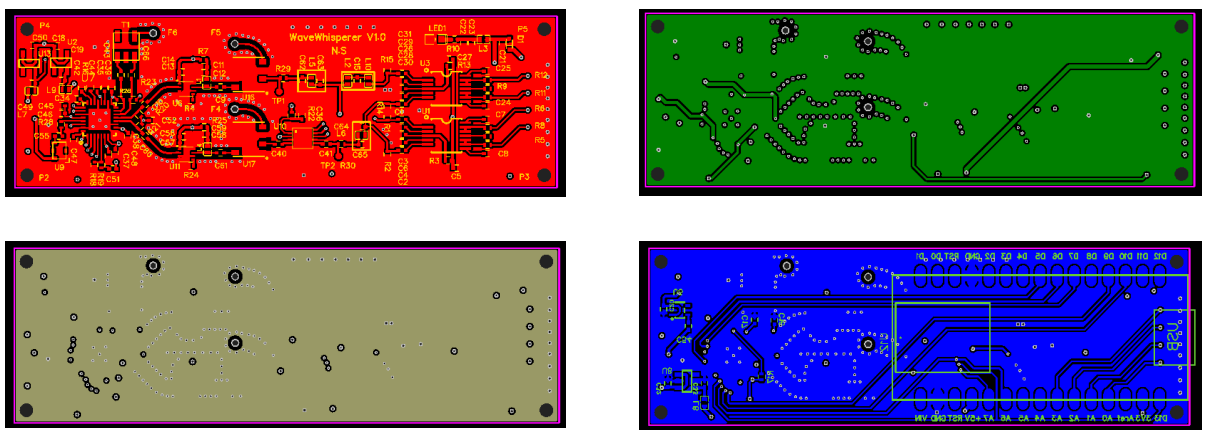


Figure. 55. The different layers of the PCB. (a) Layer 1, (b) Layer 2, (c) Layer 3, and (d) Layer 4.

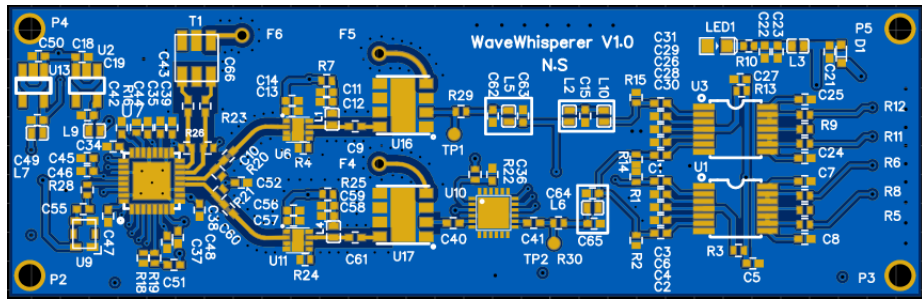


Figure. 56. A Top-layer view of the designed PCB.

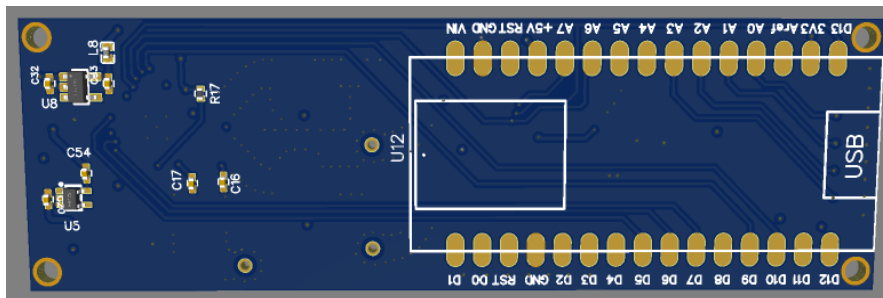
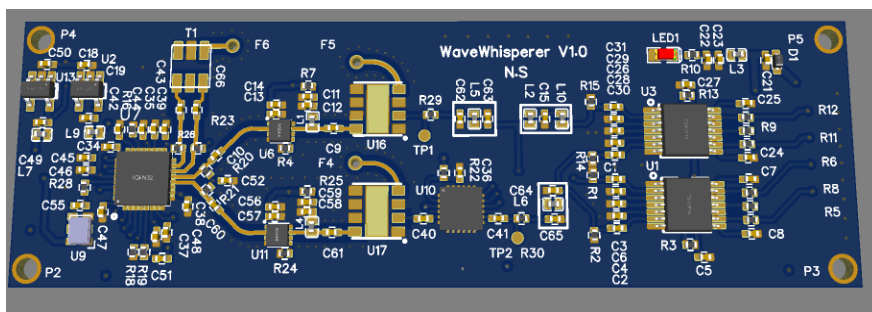


Figure. 57. 3D rendered view of the top and bottom layers.

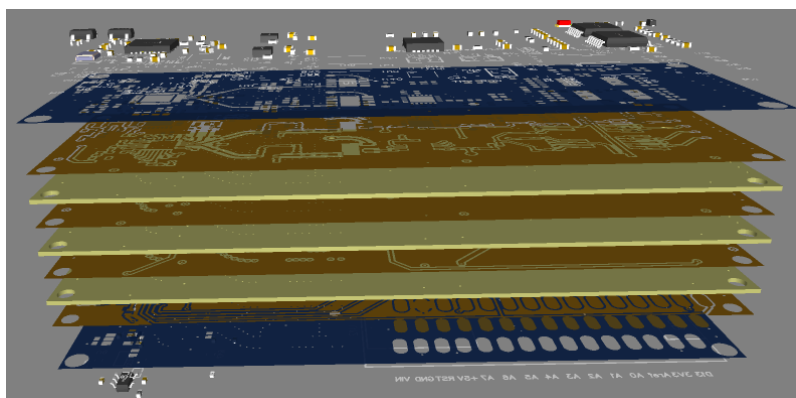


Figure. 58. Exploded view of all layers. Blue layers represent the silkscreen, golden layers represent copper, and white layers represent the dielectric material.

ii. Commercial PCB Stack-up and RF Transmission Lines:

PCB fabrication houses offer multiple stack-ups that are characterized by different properties that suit different applications, such as the thickness of each dielectric layer and its dielectric constant. The chosen 4-layer stack-up is an impedance controlled one known as the JLC7628 from JLCPCB [56]. One of the most important features of this stack-up is the dielectric constant and thickness of the dielectric material between the top conductor layer and the 2nd layer which is the ground plane. The dielectric constant of this layer is 4.6 and its thickness is 0.2 mm. For a 50-ohm transmission line, the aforementioned properties result in a line width of 0.31mm, which is ideal for impedance-controlled routing between finely pitched pins.

iii. Via Stitching and Ground Pour:

Via Stitching, is the placement of vias around transmission lines carrying high frequency signals to prevent undesired radiation and interference [57]. Hence, the overall RF leakage and coupling is reduced. The red ellipses in Fig. 59 highlight the vias surrounding transmission lines. In addition, a *ground pour*, refers to the placement

of a ground plane that surrounds routing lines and components, which aids in reduced cross talk and improved EMI suppression.

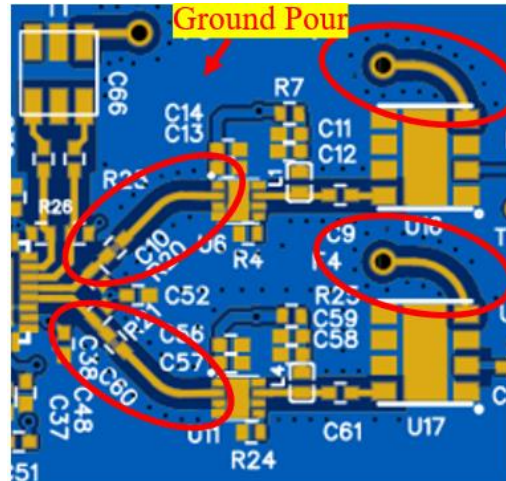


Figure. 59. Locations of the VIA stitches and the ground pour.

iv. WaveWhisperer Fabrication

After completing the design layout, the PCBs were sent to the JLCPCB [56] fabrication house. The finished PCB is shown in Fig. 60. Then, the required ICs, capacitors, resistors, inductors, and the microcontroller were soldered onto their designated positions using hot-air soldering. The top and bottom layers of the WaveWhisperer containing the respective soldered components are shown in Fig. 61. On the other hand, the source frequency module is implemented by soldering the PLL IC and its required components to a second vacant WaveWhisperer PCB while keeping other pads empty, as shown in Fig. 62. Furthermore, the compactness of the WaveWhisperer, whose dimensions are $25.4 \times 80.6 \text{ mm}^2$, is demonstrated by placing it in the palm of the hand, as shown in Fig. 63.

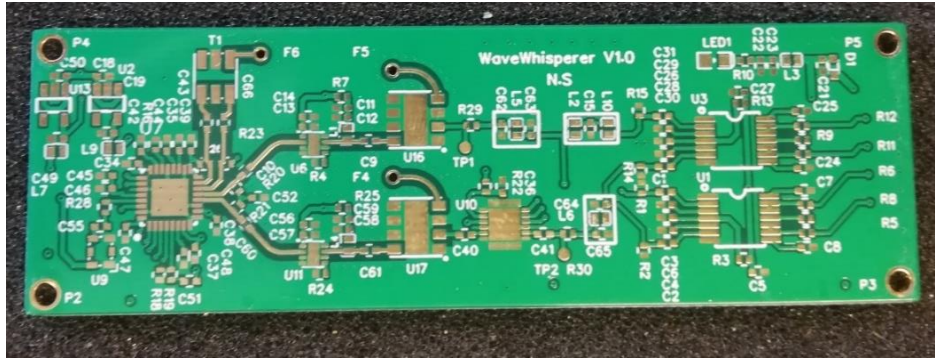


Figure. 60. The fabricated PCB.

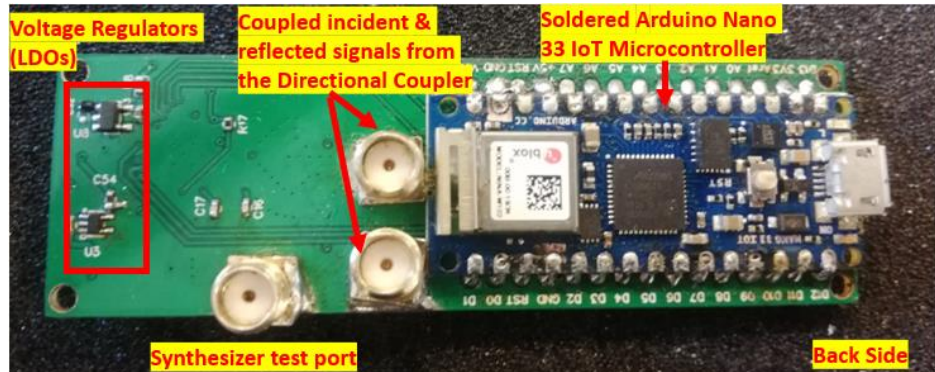
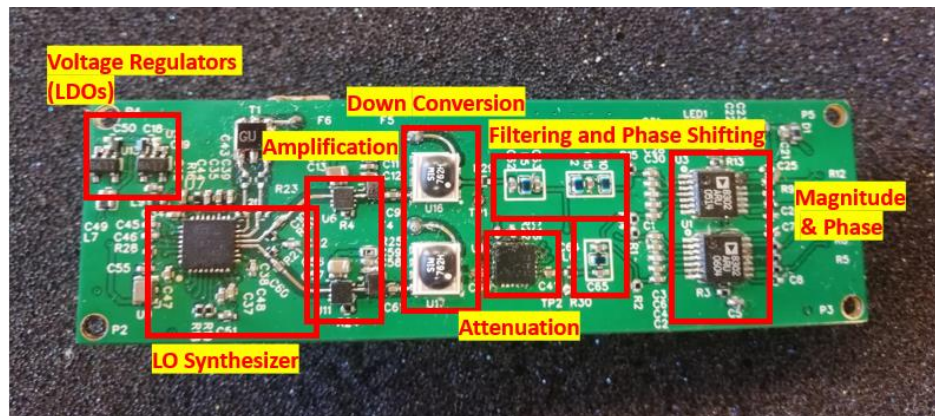


Figure. 61. The soldered PCB (a) top layer, and (b) bottom layer.

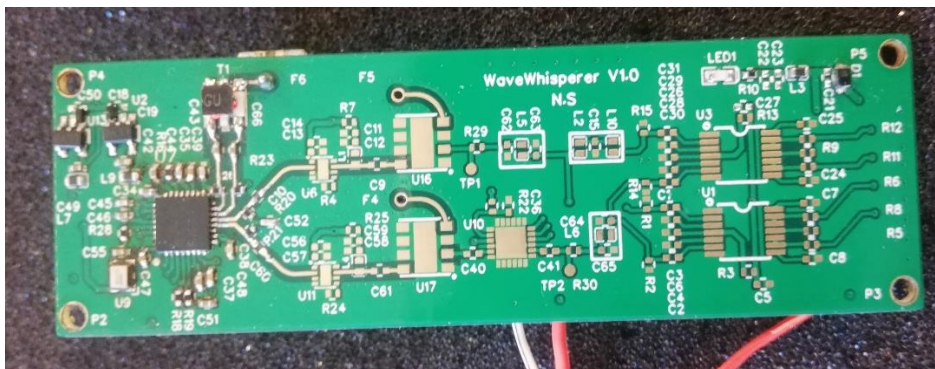


Figure. 62. The source frequency module.

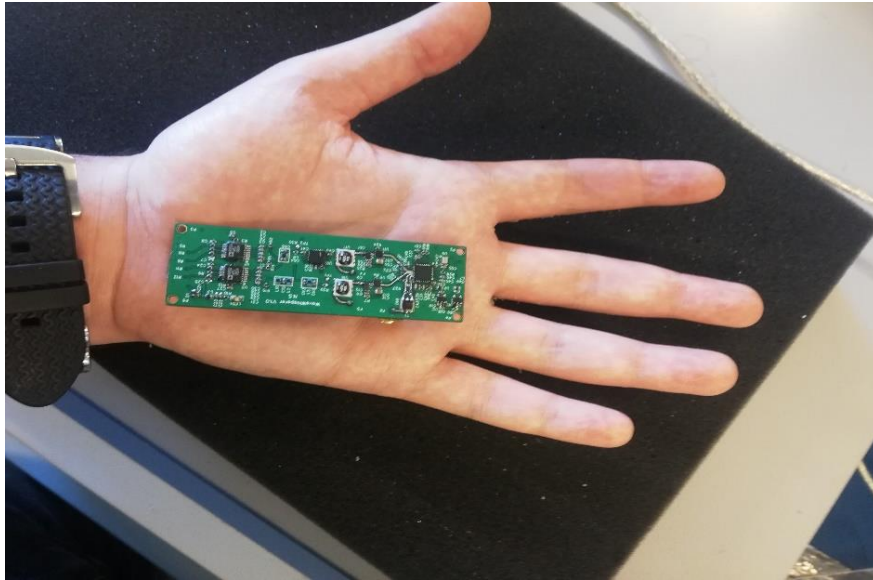


Figure. 63. The WaveWhisperer PCB in the palm for scale.

e. WaveWhisperer Testing

i. Frequency Synthesizer Testing

To validate proper communication between the microcontroller and the PLL and examine the PLL's operation, a series of frequency synthesis tests are conducted. The computer is connected to the WaveWhisperer via USB and the Arduino IDE software [58] is launched. The Arduino IDE provides a serial interface for programming the WaveWhisperer and specifying the desired output frequency that we want to synthesize, along with other settings. Next, the frequency diagnostics port (port A) of the WaveWhisperer is connected to a spectrum analyzer that will display the synthesized frequencies. The WaveWhisperer is programmed to synthesize the frequencies 1 GHz, 2 GHz, 3 GHz, and 6 GHz. By looking at the snapshots recorded from the spectrum analyzer in Fig. 64, we confirm the successful frequency synthesis by observing the desired generated frequencies.

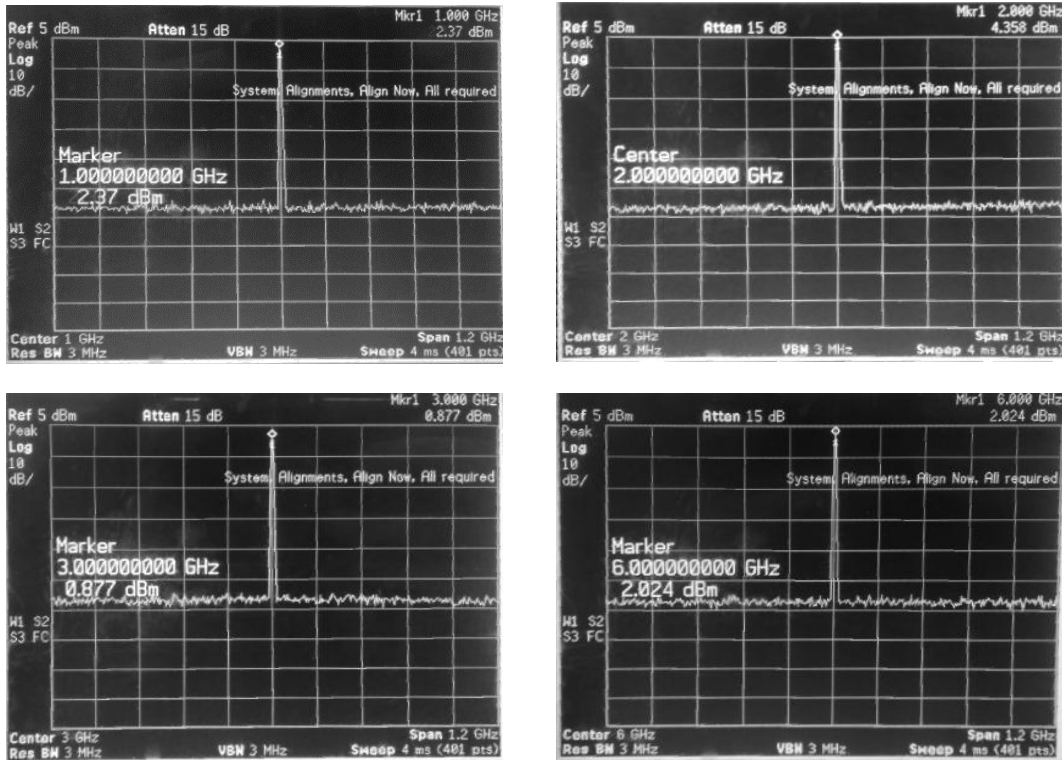


Figure. 64. Screenshots from the spectrum analyzer, showing the synthesized frequencies: (a) 1 GHz, (b) 2 GHz, (c) 3 GHz, and (d) 6 GHz.

ii. Results: Raw Measurement Data, Noise, and Filtering

After verifying successful frequency synthesis, the functionality of the different blocks within the WaveWhisperer is examined by observing the uncalibrated S_{11} data for the used EM sensor. First, the transmitter and the receiver modules of the WaveWhisperer are connected to achieve the necessary serial communication, as shown in Fig. 65. Then, the receiver module is connected to the PC via a USB cable for power and control. Afterwards, the directional couplers are used to couple portions of the incident and reflected signals from the EM sensor.

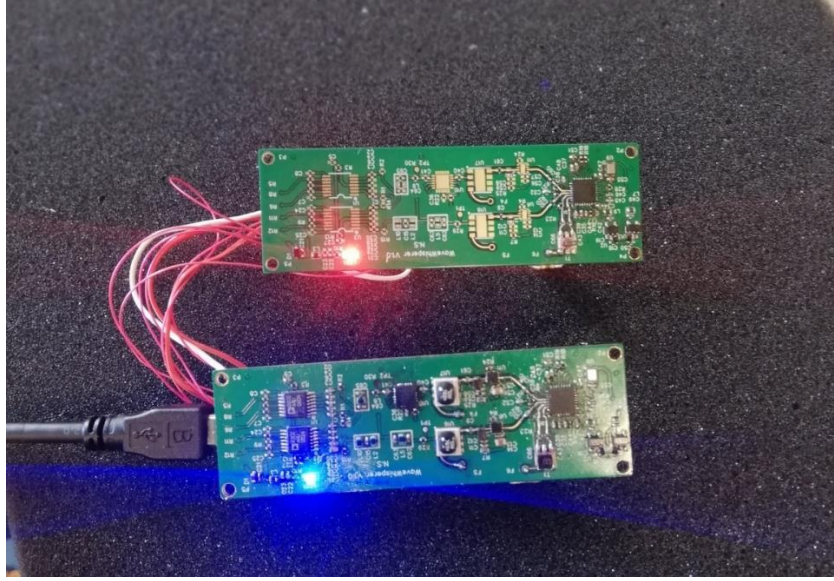


Figure. 65. WW while powered on. The red LED module is the transmitter, and the blue LED module is the receiver.

The EM sensor used operates at 4.75 GHz. The raw magnitude and phase data from detector #1, within the WaveWhisperer, is plotted in Fig. 66. The raw gain values, which are DC voltages, are transformed into their S_{11} dB equivalent by relying on (4) [51]. On the other hand, the measured DC voltages representing the phase angle values are transformed to their equivalent 0-180° values by relying on (5) [51].

$$P_{INA} - P_{INB} (dB) = \frac{V_{MAG} - 900mV}{-30mV} \quad (4)$$

$$\Delta\theta (^\circ) = \frac{V_{PHS} - 900mV}{10mV} + 90^\circ \quad (5)$$

The uncalibrated S_{11} magnitude, corresponding to the red plot in Fig. 66, shows a deviation from the 0 dB level in the non-resonant regions of the sensor. In an ideal situation, the 0 dB level means that the completely reflected signal as well as the incident signal coming from the coupled ports of the directional couplers are equal. This deviation implies an imbalance between the reflected and incident wave paths within the WaveWhisperer, which is expected since the components within have inherent losses and are not ideal. To account for this imbalance, calibration techniques

are typically adopted to improve the observed response and bring it closer to an ideal one. One of these calibration techniques, known as the short-circuit calibration, is applied here. The concept is that we first load the WaveWhisperer with a DUT that causes full-wave reflection, such as a short circuit. Then, the response of the reflected and incident paths is measured, providing us with quantitative information regarding the imbalance. Then, the difference between obtained response and the ideal measurement (0 dB) is computed and added to any subsequent measurements to account for the imbalance. This calibration technique is applied to our EM sensor, and the calibrated response exhibits significant improvements that closely resemble an ideal one, as shown in Fig. 66.

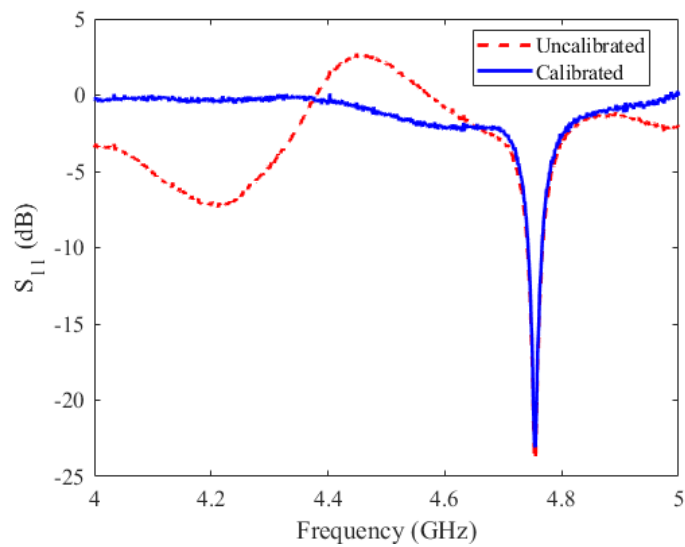


Figure. 66. The raw and the calibrated S_{11} of the used EM sensor.

Furthermore, the WaveWhisperer is then used to perform measurements – identical to clinical ones that utilize a VNA—using our EM sensor. Accordingly, the magnitude of the sensor’s S_{11} is measured in both free-space and while being loaded with a volunteer’s forehead skin. Fig. 67(a) presents the outcome of both the unloaded and loaded states, where the latter is represented by a shift in the frequency of operation

as well as the magnitude of the S_{11} . Initially, the response was slightly noisy, which is attributed to high frequency noise and the inaccuracies of the microcontroller's ADC which is sampling the DC voltage measurements coming from the detectors. To reduce this noise, a Finite Impulse Response (FIR) low-pass filter is utilized. The designed filter was found to provide optimal results when the passband frequency is 150 Hz, and the stopband frequency is 1000 Hz. As a result, the response obtained after the application of the FIR filtering was smoother and contains less noise, as shown in Fig. 67(b).

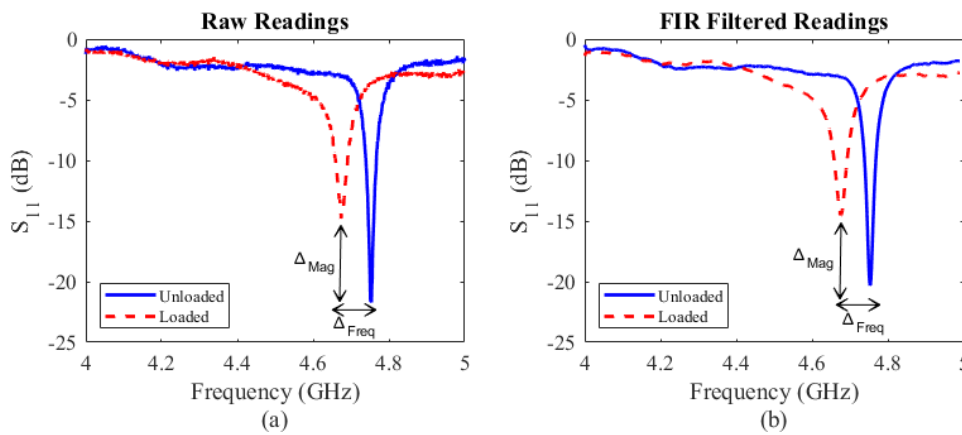


Figure. 67. (a) The S_{11} response with and without loading. (b) The FIR filtered response.

After measuring the magnitude, the phase response of each detector is also measured. Fig. 68 presents these responses in a raw unloaded state, a raw filtered state, a raw loaded state, and a raw filtered state. The 0-180° phase response from each of the two detectors is used to calculate the corresponding 0-360° phase response in both the unloaded and loaded states. The raw unloaded and loaded phase responses are plotted in Fig. 69(a) and the filtered counterparts are plotted in Fig. 69(b).

From Fig. 67 and Fig. 69, we are able to successfully validate that our wave analyzer, the WaveWhisperer, is capable of measuring the frequency shift and the

changes in the phase and magnitude of the S_{11} that are practically witnessed within clinical settings.

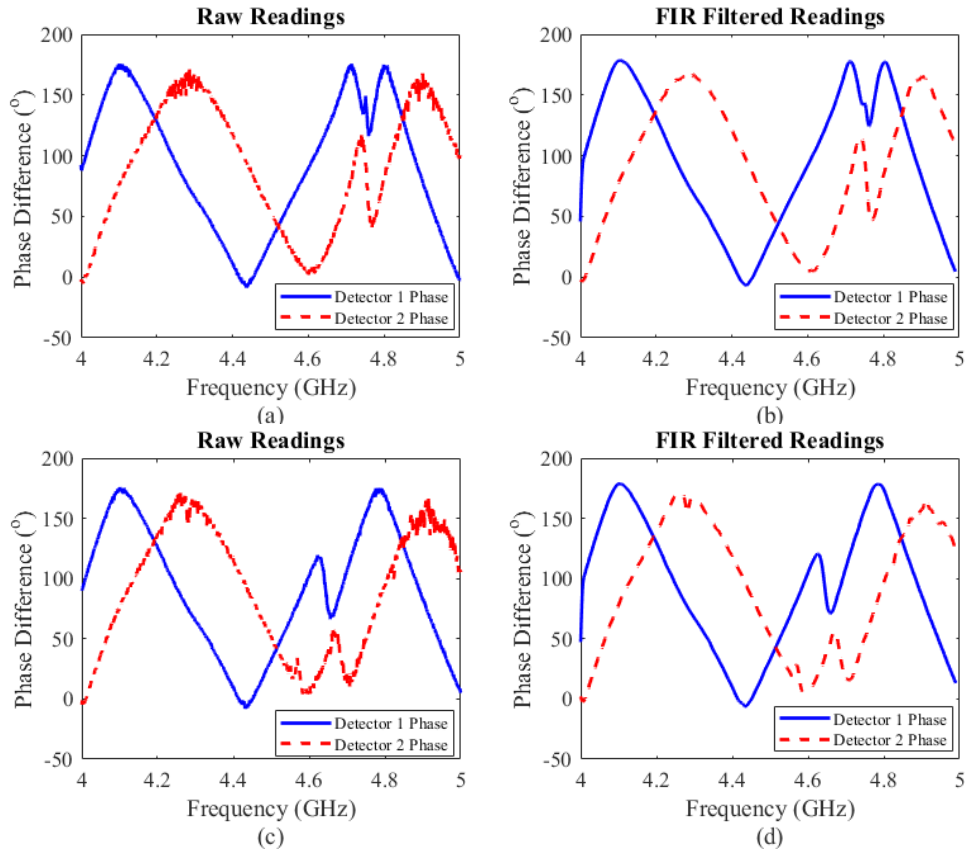


Figure. 68. The phase response of the two detectors in: (a) the raw unloaded state, (b) the FIR filtered unloaded state, (c) the raw loaded state, and (d) the filtered loaded state.

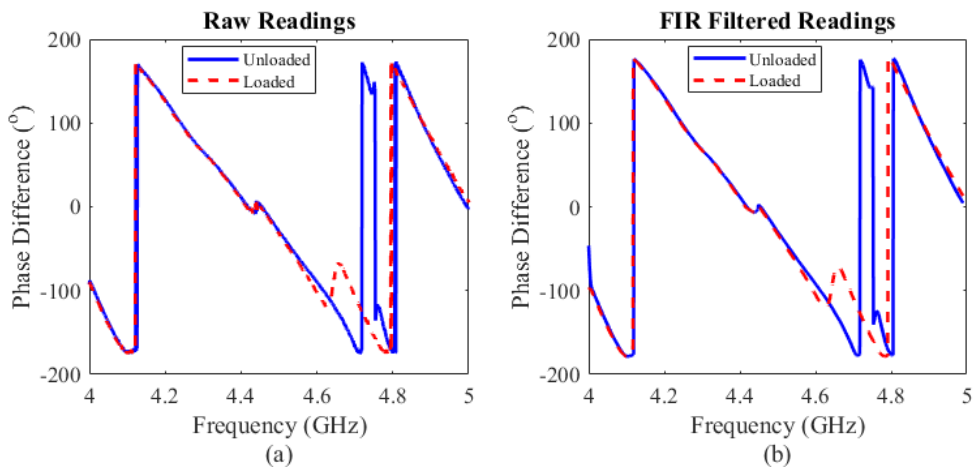


Figure. 69. (a) The raw unloaded and loaded 0-360° phase response. (b) The FIR filtered version of the phase response.

E. Discussion

The design of the initial EM sensor unveiled major challenges to its successful utilization as a diagnostic sensor. These challenges oriented the rationale behind the updated design decisions that formed the cornerstone of the second, improved, and tailored EM sensor. Particularly, the improved sensor introduces a lesion-optimized sensing tip that aims to enhance the interaction between the emanating electromagnetic fields and the skin lesion under test. This enhancement is achieved through adopting a customized hemispherical sensing tip that focuses and enhances the density of the emanating EM fields. Such a technique leads to an improved measurement sensitivity at a practical stand-off distance. The sensor also makes use of a designed metallic enclosure that restricts the sensor's sensing to the particular lesion under test beneath the sensing tip. This also prevents sensing from the surrounding interferers such as objects in close proximity to the sensor and ambient RF noise. These crucial design decisions and modifications enabled a much more sensitive and robust sensor that is optimal for lesion sensing procedures.

Furthermore, the realization of the WaveWhisperer wave analyzer and its successful validation substantiates that such technology can be miniaturized and customized to suit the application at hand. Essentially, the WaveWhisperer employs a custom RF chain composed of magnitude and phase detectors, frequency sources, down-conversion stages, among other RF components. The WaveWhisperer ultimately aims to measure the properties of the reflection coefficient that in turn, highlight the properties of a specimen under test. By integrating the WaveWhisperer and the developed lesion-optimized sensor into one product, we have effectively produced a

powerful RF sensing system that otherwise would have forced researchers to adopt physically impractical, highly expensive, and non-customizable alternatives.

CHAPTER VI

CLINICAL TRIALS

A. Introduction

Trials are conducted to validate the operation of our sensor and technique in an intended clinical setting. The performed clinical trials include testing on patients with pre-diagnosed skin cancer as well as healthy control participants. Furthermore, the clinical trials in this study are approved by the Institutional Review Board at the American University of Beirut. These clinical trials consist of testing the developed EM sensor on a population of 23 participants, which is divided into 12 patients and 11 healthy volunteers. The following sub-sections detail the measurement procedure for each participant group.

B. Measurements on Skin Cancer Patients

The patients involved in this clinical trial are readily pre-diagnosed with skin cancer, where 11 were diagnosed with BCC and 1 was diagnosed with SCC. Our measurements are performed on patients only minutes before undergoing Moh's surgery for the extraction of their cancer. During these measurements, the primary Moh's surgeon is present and oversees the procedure, and the patients have signed the pertinent informed consent. The patient population includes 6 males and 6 females with ages ranging between 32 and 87. Our measurements are performed in vivo while the cancer is still intact on the skin prior to its extraction. This is crucial in order to preserve the fidelity of the measurements especially that the temperature of the body as well as external factors, such as hydration, dryness, or added preservative solutions cause changes in the dielectric properties of the specimen used [6], [8], [26], [59], [60].

Furthermore, works in the literature [61]–[63] have compared the effect of in-vivo and ex-vivo measurements on dielectric properties of a specimen under test, where it is shown that differences in the dielectric properties do exist, especially if the environmental and physiological conditions of the specimen are not preserved.

As a result, we propose and adopt a measurement approach that utilizes multiple techniques to advance the measurement accuracy and preserve the fidelity of the specimen's properties while accounting for the aforementioned variables. Our approach is based on performing differential in-vivo clinical measurements to overcome the challenges faced when measurements are executed on previously excised and pre-processed excisions. This means that we avoided any form of altering the specimen under test, whether by extracting it from its natural environment, decreasing its temperature, or introducing preservative solutions that are typically required for ex-vivo measurements.

The differential mode entails measurements on the cancer as well as on the adjacent healthy tissue in order to diminish the effect of variables that are common to both. As such, measurements are performed by positioning the sensor directly on top of the cancer, where the foam separator embedded within the sensor maintains a fixed distance between the sensing tip and the specimen. Then, 10 measurements of the magnitude and phase of the reflection coefficient are recorded at each site. Next, the sensor is placed on the adjacent healthy tissue and an additional 10 measurements of the same parameters are recorded. Multiple measurements are performed on each site in order to obtain an average value that reduces the random error and the potential fluctuations in the sensor's response. The cancers included in our study were obtained from diverse locations on the face, and they were mostly spread across the nose, cheeks,

temples, forehead, and the scalp, as illustrated Fig. 70. Furthermore, the characteristics of the examined skin cancers for each patient are presented in Table. 3.

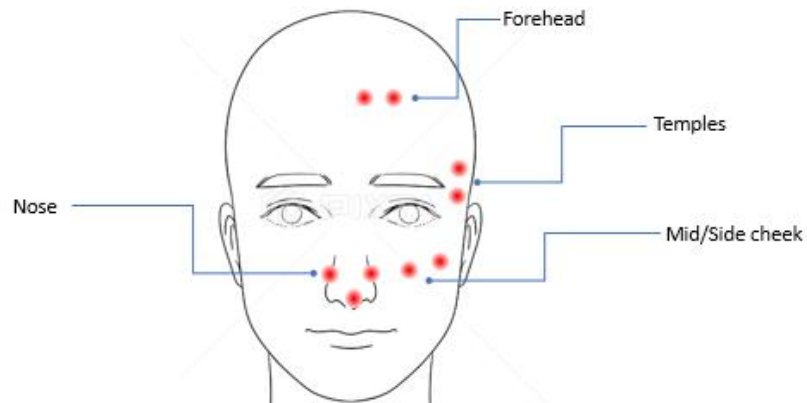


Figure. 70. Most common cancer locations throughout the clinical trials. This figure is modified from <https://www.pixtastock.com/illustration/60972716>.

Table. 3. Patient details.

Patient #	Gender	Type	Site	Dimensions mm2
1	M	SCC	Temple	1.5x1.1
2	F	BCC	Forehead	15x10
3	M	BCC	Tip of nose	8x10
4	M	BCC	Tip of nose	5x5
5	F	BCC	Side nose	6x4
6	F	BCC	Side nose	4x3
7	M	BCC	Top cheek	1.6x1
8	M	BCC	Scalp	NA
9	M	BCC	Ear lobe	NA
10	F	BCC	Forehead	NA
11	F	BCC	Upper nose	NA
12	F	BCC	Scalp	NA

C. Measurements on a Healthy Control Group

Obtaining a large dataset of healthy skin measurements at different locations on the skin provides additional insight on the general properties of healthy skin and leads to more accurate data models. As a result, measurements are performed on 11 healthy individuals, 5 males and 6 females, where measurement locations are chosen to be similar to those that were previously performed on skin cancer patients. Similarly, measurements are repeated 10 times per site until all sites are tested. It is also worth mentioning that all participants are characterized by type III skin on the Fitzpatrick skin scale [32]. Table. 4 summarizes the details of both healthy and patient populations and their respective measurements.

Table 4. Overall subject and measurement information.

Number of Subjects	23
Number of Patients	12
Number of healthy controls	11
Patient Measurements /Patient	20-40
Healthy Measurements /Patient	90
Ages	24 – 87
Conditions	BCC, SCC, Healthy

D. Discussion

The involvement of healthy individuals and skin cancer patients in our clinical trials served to clearly demonstrate the differences between the healthy and diseased skin. Additionally, the in-vivo differential mode of testing on both groups provides an

unadulterated interrogation of the measured specimen's nature, leading to high-quality measurements within a realistic measurement setting. Notably, the quality of the measurements has a direct effect on the sensor's ability to detect differences between the various measured specimen, and ultimately, impacts the ability to achieve accurate diagnosis and classification.

CHAPTER VII

ANALYSIS, RESULTS, AND DISCUSSION

A. Introduction

The magnitude and phase data of the reflection coefficient (S_{11}) both provide the necessary information that eventually determines the difference between the measured specimens, which are composed of tissues with different complex permittivity values. By relying on a statistical analysis of their properties, we can ultimately distinguish between benign or malignant skin lesions. Our proposed EM sensor along with the FieldFox VNA [43] are used to perform these measurements and record them. In each measurement, whether on healthy or cancerous lesions, we sweep 1001 points from 4 GHz to 5 GHz, 10 times. The 10 redundant measurements per site are then averaged to reduce any random fluctuations. These measurements are obtained by positioning the EM sensor on the healthy and cancerous specimens and lightly pressing against the skin with constant pressure to ensure proper contact between the sensor and the skin, as shown in Fig. 71. Finally, the data is categorized based on the nature of the specimen, e.g.: healthy, cancerous, where each category includes a set of S_{11} magnitude measurements and a set of S_{11} phase measurements. In the following sub-sections, we evaluate the proposed sensor's performance, explore two approaches for data modeling and prediction, and analyze the obtained results.

B. Performance: The Distinct Response to Healthy and Cancerous Skin Lesions

The plots in Fig. 72 and Fig. 73 represent our proposed sensor's raw S_{11} measurements on a patient's cancerous lesion and its adjacent healthy skin in terms of

magnitude and phase, respectively. The response of the sensor in both cases is manifested as a shift in the resonance frequency, as well as changes in the magnitude and phase of the sensor's measured S_{11} from an initial unloaded state. We can also observe the existence of distinctive characteristics for the cancerous and healthy measurements in terms of resonance frequency and S_{11} . These differences, their levels, and their associated trends, form the basis of our analysis in the coming sections.



Figure. 71. The EM sensor placed on top of skin.

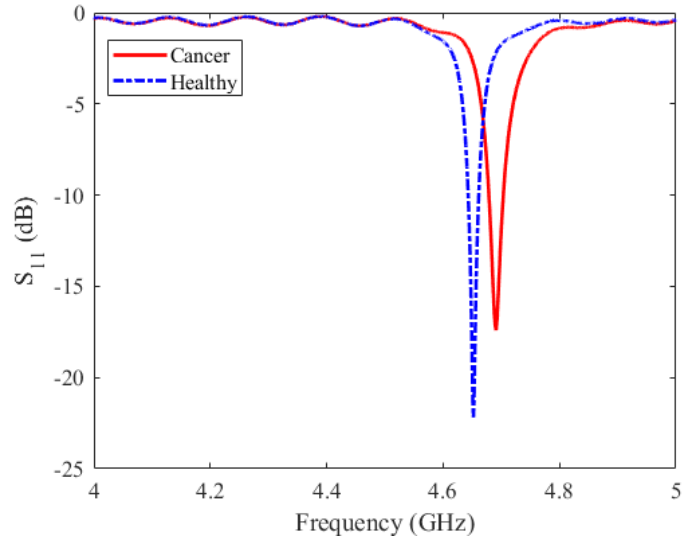


Figure. 72. S_{11} magnitude measurement of a skin cancer and its adjacent healthy skin.

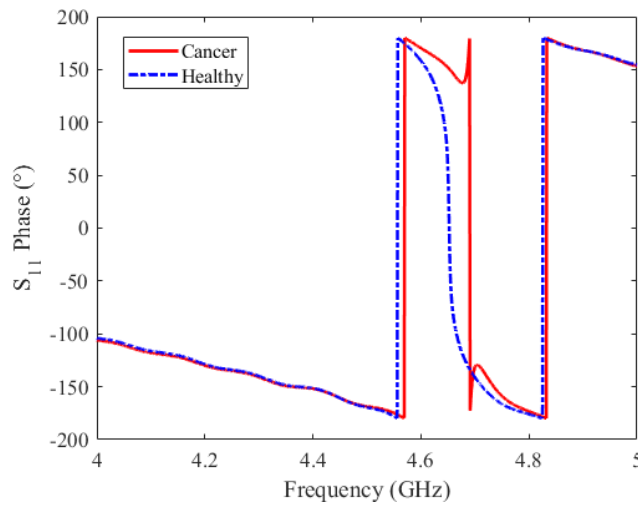


Figure. 73. S_{11} phase measurement of a skin cancer and its adjacent healthy skin.

C. Model Design, Analysis, and Results

1. *Imbalanced to Balanced Data: Synthetic Minority Oversampling Technique (SMOTE):*

In practical applications, and specifically medical ones, classes used in data analysis may not be balanced, in other words, they might not have an equal number of observations, which might lead to misclassification [64]. The class with the fewest observations is called the minority class, whereas the majority class is characterized by

its higher number of observations. As a direct consequence to this imbalance, models using such training data will result in higher classification accuracy for the majority class, while exhibiting lower accuracy for the minority class. In fact, our primary information of interest often lies in the minority class, such as disease prevalence [65]. Notably, balancing the data has been proven to improve the prediction capability of a machine learning model. For this reason, the SMOTE [66], a widely popular algorithm, is introduced as a mean to synthesize new data points instead of replicating the pre-existing data to balance the minority class, such as cancer measurements. Such oversampling enables higher accuracy and deeper insight. SMOTE has seen numerous applications within the literature in applications where data imbalance prevails [65]–[69]. The SMOTE algorithm, based on a distance metric, interpolates between a specified number of neighbors from the pre-existing dataset to generate the new data point. For instance, Fig. 74 shows 5 minority class points: x_i to x_{i4} that are used to create the 4 new minority class instances, r_1 - r_4 [66]. In the upcoming sections, SMOTE will be used to increase the minority class observations, i.e.: skin cancer observations.

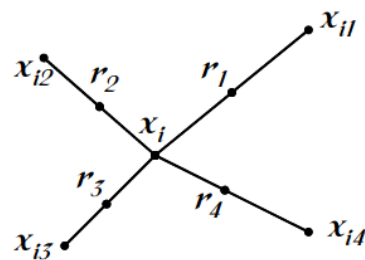


Figure. 74. Illustration of SMOTE synthesis [62].

2. *Support Vector Machines (SVM):*

a. Introduction

SVM is one of the most powerful and commonly used machine learning algorithms that are employed in a variety of applications. The SVM is a kernel-based

machine learning algorithm used in regression and classification applications, and it falls under the category of supervised learning algorithms [70]. Notably, SVM is commonly employed in a plethora of medical binary classification applications due to its powerful classification ability, such as several cancer classification and prediction problems [71]–[74]. The primary objective of the SVM is to generate an accurate boundary, known as the hyperplane, between the groups of data to be classified. The SVM takes training data as well as pre-defined outcome labels to train the model. In addition, one of the most important characteristics of the SVM is its soft margin. The soft margin is a separator between the data classes that is formed by border-line data points belonging to the different classes to form what is known as Support Vectors. In other words, support vectors utilize some of the data points from both classes to build the decision boundary.

SVM utilizes functions known as kernels that, if necessary, transform the input data into higher dimensions where the classes become linearly separable. There are several kernel functions, the most common ones are the Linear, Polynomial, RBF, and the Sigmoid, where each one of them is capable of producing different hyperplanes to separate the different classes, as illustrated in Fig. 75. Typically, an SVM model is tested with different kernel functions, and the kernel function that results in an SVM with the lowest K-Fold Cross Validation Error is then adopted as the best predictor. After choosing the appropriate kernel function, the model is trained using a training data set and pre-determined labels, and then its prediction performance is validated using a testing dataset. Throughout our study, we will employ SVM as our classification model.

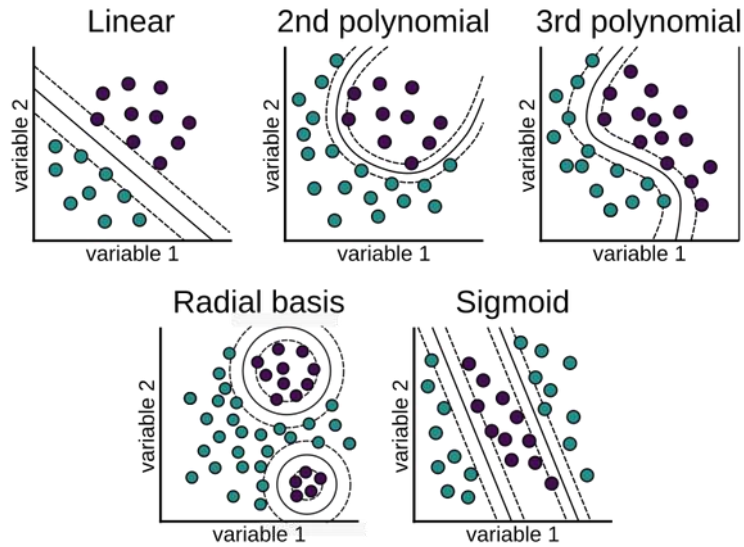


Figure. 75. Typical SVM hyperplanes [75].

b. K-Fold Cross Validation

Typically, a classification model is evaluated based on its prediction performance, which is achieved by dividing a dataset into a training dataset and validating its performance by utilizing a testing dataset. This methodology, however, may not provide the most optimal evaluation, since only one subset from the entire dataset was used to evaluate a model's accuracy. K-Fold CV is introduced to solve this problem by dividing the dataset into K partitions, and iteratively ensures the usage of each partition for testing while the remaining partitions are reserved for training. K-Fold CV is especially important when comparing the performance of a model using different kernel functions. The kernel that results in a model's lowest K-Fold CV is the one exhibiting the highest prediction performance on the utilized data set and must therefore be used in the designed model.

c. Performance Metrics

Some of the most common evaluation metrics for machine learning algorithms that will be used throughout this study are Sensitivity, Specificity, Accuracy, and

Youden's index (YI). These metrics are derived from the confusion matrix elements, namely the True Positive (TP), False Positive (FP), True Negative (TN), and False Negative (FN) rates.

$$Sensitivity = \frac{TP}{(TP + FN)} * 100 \quad (8)$$

$$Specificity = \frac{TN}{(TN + FP)} * 100 \quad (9)$$

$$Accuracy = \frac{TP+TN}{(TP + TN+FP+ FN)} * 100 \quad (10)$$

$$YI = Sensitivity - (1 - Specificity) \quad (11)$$

3. *Approaches for Classification and Prediction*

a. Correlation-Based Classification

The magnitude and the phase of the S_{11} for patients and healthy volunteers are collected. For patients, the S_{11} measurements are organized into measurements of cancerous-lesion origin and of adjacent-healthy origin. Likewise, for the healthy volunteers, S_{11} measurements at different locations that mimic the locations of cancerous lesions are organized according to their measurement location, e.g.: Temple 1, Temple 2, Forehead 1, and Forehead 2. Originally, the S_{11} data is measured at 1001 points, where each point corresponds to a frequency step of 1 MHz within the 4 GHz to 5 GHz frequency span. To reduce computation time and improve data visualization, the insignificant S_{11} measurements surrounding the resonance bandwidth of the sensor are omitted. As such, for each patient we choose a bandwidth of 141 MHz centered around its resonance frequency of the cancer measurement (typically ~4.6 GHz). Similarly, the corresponding healthy measurement of the same patient is also centered around its new resonance frequency within a larger 200 MHz bandwidth. This larger bandwidth allows us to

choose the 141 observation points of the healthy measurements that coincide within the 141 cancer-measurement frequency range, essentially allowing us to maintain the shift in the resonance frequency from the cancer reference. Fig. 76 represents the S_{11} magnitude of the cancerous and healthy lesions of 12 patients, and Fig. 77 represents the phase response for 10 patients. Similarly, Fig. 78 and Fig. 79 represent the magnitude and phase response of measurements on two adjacent forehead locations on 11 healthy volunteers. It is worthy to note that the measurements of patients, whether in magnitude or phase, exhibit distinct differences in terms of the shift in frequency and the magnitude and phase of the S_{11} . On the other hand, measurements on healthy volunteers exhibit an extreme degree of similarity.

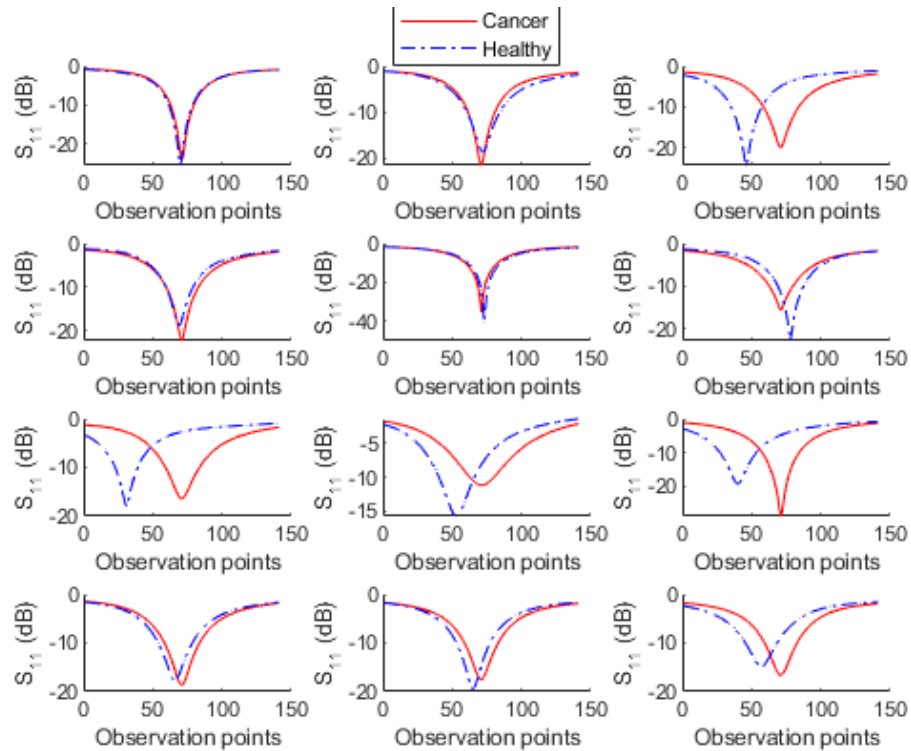


Figure. 76. S_{11} magnitude variation between healthy and cancerous lesions for 12 patients.

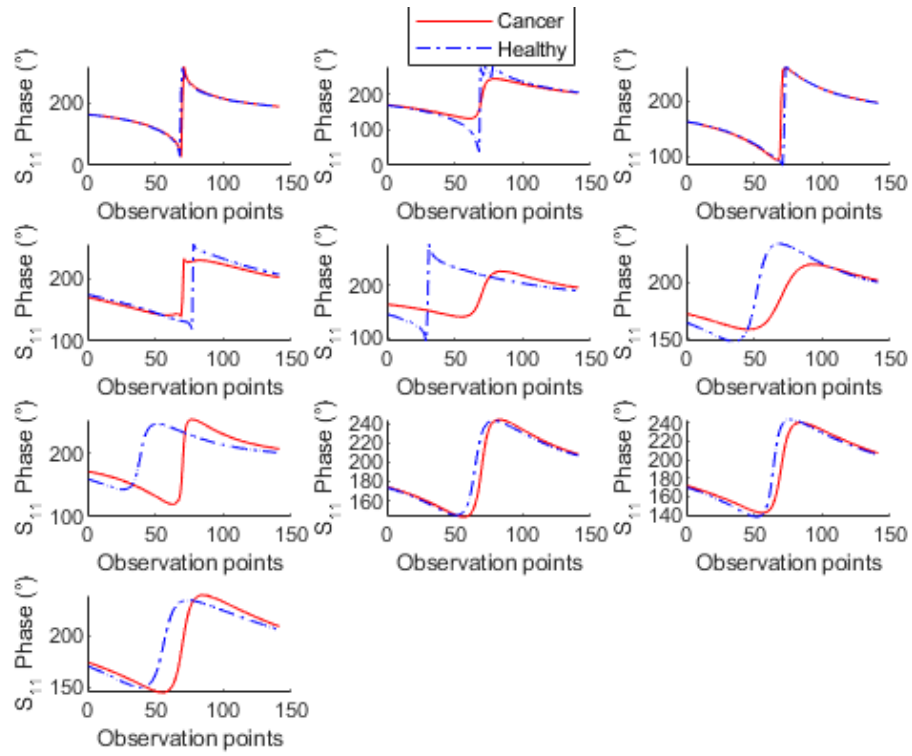


Figure. 77. S_{11} phase variation between healthy and cancerous lesions for 10 patients.

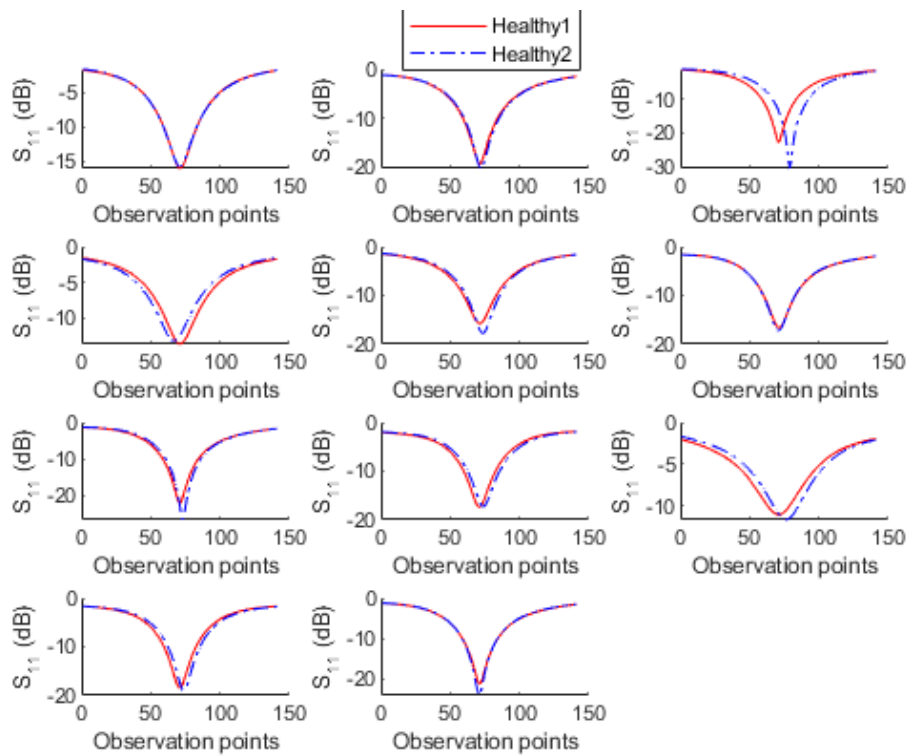


Figure. 78. S_{11} magnitude variation between two forehead locations for 11 volunteers.

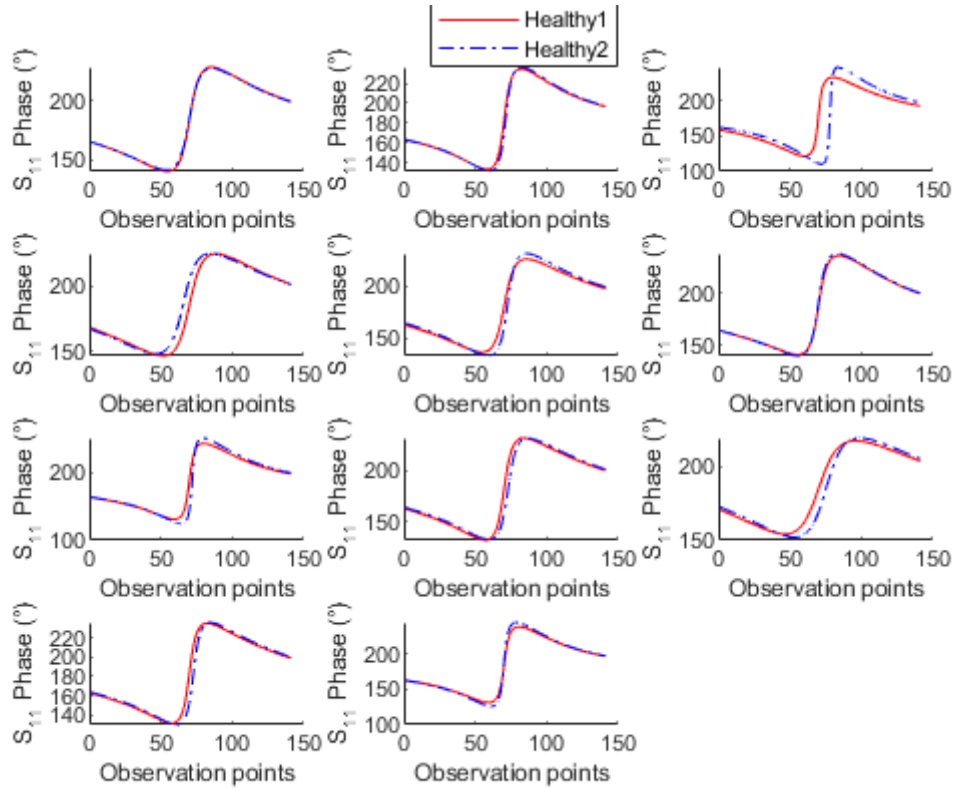


Figure. 79. S_{11} phase variation between two forehead locations for 11 volunteers.

Afterwards, the squared correlation, also known as the coefficient of determination, denoted by r^2 , is calculated between the differential measurements of each subject. For patients, we obtain r_{H-C}^2 for both the phase and magnitude measurements of the healthy skin and the cancerous lesion within a patient, and for healthy volunteers we obtain r_{H-H}^2 for the phase and magnitude measurements at two adjacent healthy locations. These correlation values essentially demonstrate the relation between the tested classes of skin (cancerous and healthy). Furthermore, we obtain the value of $1 - r^2$ for all correlation values, since it better represents differences within the two classes when compared to r^2 .

Since measurements on patients (correlation values) are less than measurements on healthy volunteers, we are dealing with a typical data imbalance

scenario in medical applications. For this reason, we employed the well-known SMOTE oversampling algorithm to increase our patient measurement population. As a result, we expanded the measurement data from 10 correlation points (each corresponding to a patient) to 44 points, effectively balancing the data with the 44 healthy measurements. As for healthy volunteers, 141 points are also extracted around the resonance frequency at each measurement location, and the same alignment procedure to that of patients is applied to maintain shifts in frequency.

At this stage, the best data model will be sought to provide the model that can best predict malignancy of skin lesions. The model to be used utilizes the previously discussed SVM classifier, and an iterative procedure is followed to determine the kernel function that results in the smallest K-Fold CV. Towards this end, the data is divided into 90% training data while the remaining 10% are reserved for testing. For our study, we evaluated the most common kernel functions, namely, the Polynomial, Linear, and Radial Basis Function (RBF) kernels. Our results have shown that the polynomial kernel achieved a K-FOLD CV error of 6.2% when compared to Linear and RBF kernels, as summarized in Table. 5. Hence, the polynomial kernel along with training data and the corresponding labels are used to construct our SVM classifier. The process of choosing the training and testing data is repeated 20 times, where each time the data is shuffled randomly before being fed into the SVM classifier.

Our model exhibits significant statistical results, as represented by the outcome of our performance metrics. This model is characterized by a 3.3% test error, a sensitivity of 97.85%, a specificity of 95.4%, a YI of 93.25%, and an accuracy of 96.67%, as summarized in Table. 6. Fig. 80 shows the $1 - r^2$ values of

the overall magnitude and phase measurements for all subjects along with their respective predictions. The healthy measurements are represented by blue dots, the cancerous lesions are represented by red stars, the red squares are cancer predictions, and the blue squares are healthy predictions. Additionally, four runs of the SVM model fed by shuffled training and testing data are illustrated in Fig. 81, where a clear distinction is shown between cancer measurements, healthy measurements, and the chosen support vectors with the respective SVM hyperplane boundaries. Finally, the effect of SMOTE is analyzed by plotting all test errors with respect to the test numbers in the cases of with and without SMOTE in Fig. 82. As expected, the model employing SMOTE achieved significantly less test errors compared to the model without SMOTE.

Table 5. CV evaluation of the polynomial, RBF, and linear kernels.

METRIC	POLYNOMIAL	RBF	LINEAR
K-FOLD CV	6.2%	6.6%	9%

Table 6. Performance metrics for the best SVM model.

BEST KERNEL	TEST ERROR	SENSITIVITY	SPECIFICITY	YI	ACCURACY
POLYNOMIAL	3.3%	97.85%	95.4%	93.25%	96.67%

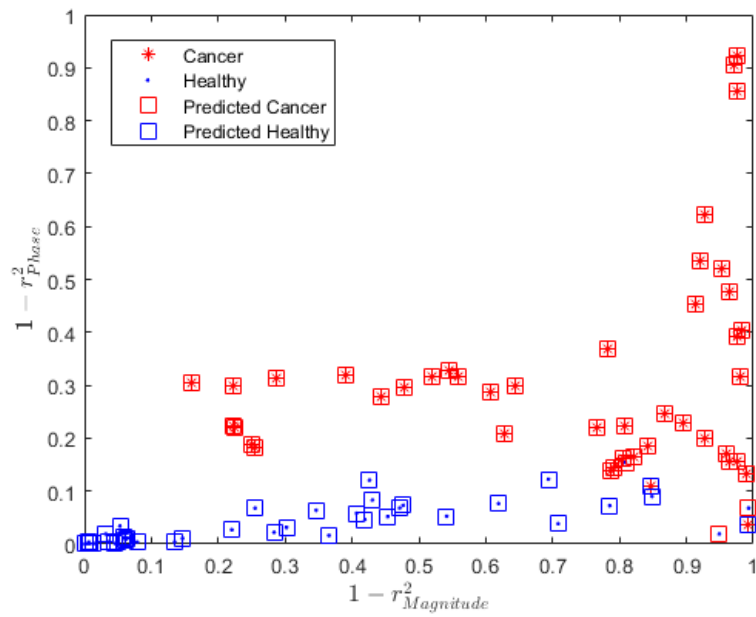


Figure. 80. The overall magnitude and phase sample points and the corresponding predictions.

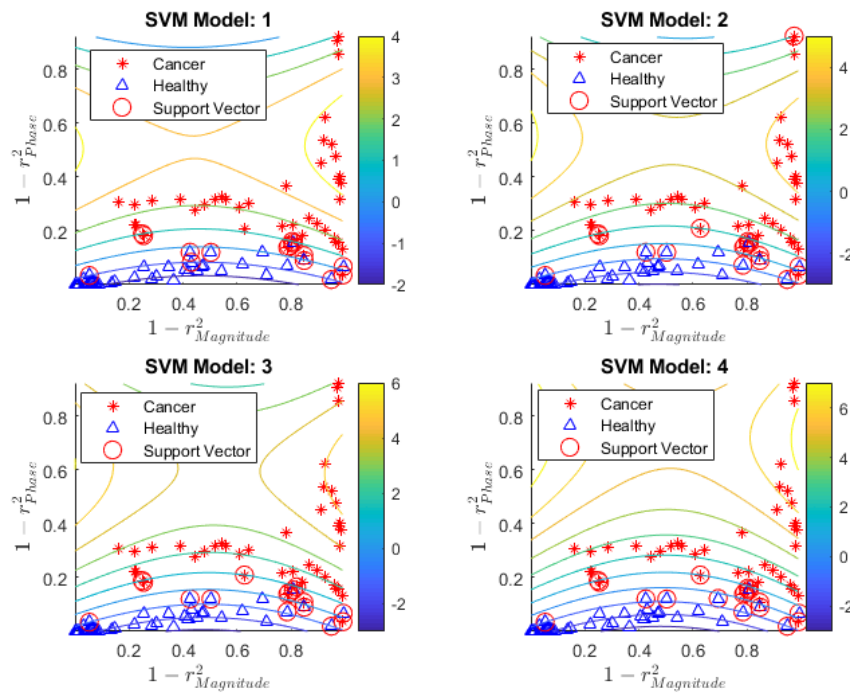


Figure. 81. Four runs of the SVM model fed by training and testing data shuffled randomly.

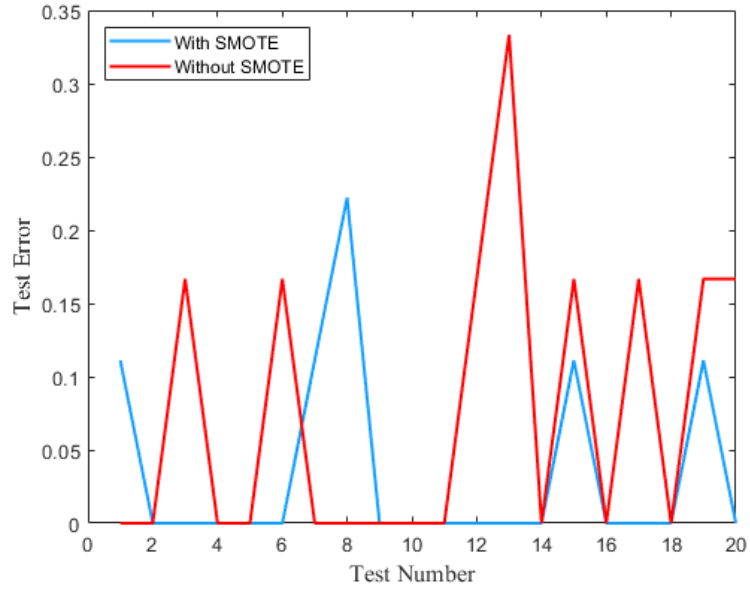


Figure. 82. The model's test outcome with and without SMOTE employed.

b. Feature Selection Wrapper

In this approach, we rely on the magnitude and phase values of the S_{11} within a chosen bandwidth, essentially resulting in a large feature pool instead of relying on correlation values as in approach #1. The objective of this approach is to traverse every feature (frequency) within our selected range and analyze the corresponding observations (magnitude and phase for every patient and control) measured at these features, and ultimately extract the feature sets that best predict the outcome. In this approach, we take the difference between the healthy and cancerous measurements of patients (Δ_{HC}) and the difference between the healthy measurements at different locations for the healthy volunteers (Δ_{HH}). This difference is applied to both the magnitude and phase data, e.g.: (ΔMAG_{HC}), (ΔPH_{HC}), (ΔMAG_{HH}), and (ΔPH_{HH}). If the entire 141-point range is taken, we would have 141 points for ΔMAG and 141 points for ΔPH , which results in 282 features. Since many of these features surrounding the resonance bandwidth of the sensor are insignificant for our analysis, the data must be

reduced by omitting ΔMAG and ΔPH that fall below preset thresholds. As such, the raw magnitude and phase data pass through a normalization block that selectively omits ΔMAG values below a threshold of 10 dB and the ΔPH values below a threshold of 30°. Additionally, these magnitude and phase values are normalized to limit their distribution between 0 and 1.

To account for the data imbalance between the majority class (healthy volunteers) and the minority class (cancer patients), the SMOTE is used to balance the patient and control classes. As such, 34 additional observations to the patient minority class are generated using the SMOTE, for both the ΔMAG and ΔPH . To perform feature selection, a modified form of the Forward Feature Selection Wrapper (FFSW) technique is employed. The FFSW takes the number of best features to be sought as a parameter labeled `num_features`. Once `num_features` is specified, the FFSW will traverse the entire feature pool in aims of finding the best set of `num_features` that results in the lowest test error. Our developed algorithm runs the sequential feature selection while using the SVM classifier as the model. The FFSW is iterated for three kernel functions: Polynomial, RBF, and Linear. Within each iteration, the K-Fold CV, with a K of 10, is calculated for each newly added feature set. This allows us to observe what number of features, out of the best features, results in the lowest K-Fold CV. This procedure is repeated for all kernel functions. Then, the kernel resulting in the lowest K-Fold CV is chosen along with its set of best features. Fig. 83 shows the K-Fold CV for each kernel as a function of `num_features`.

After identifying the best kernel function and the optimal number of features, an SVM model is trained on data at the aforementioned features. Then, the model is validated 10 times using test data at the best features, where the testing and training data

are randomly shuffled. This approach resulted in significant results based on our predefined performance metrics, as summarized in Table 7.

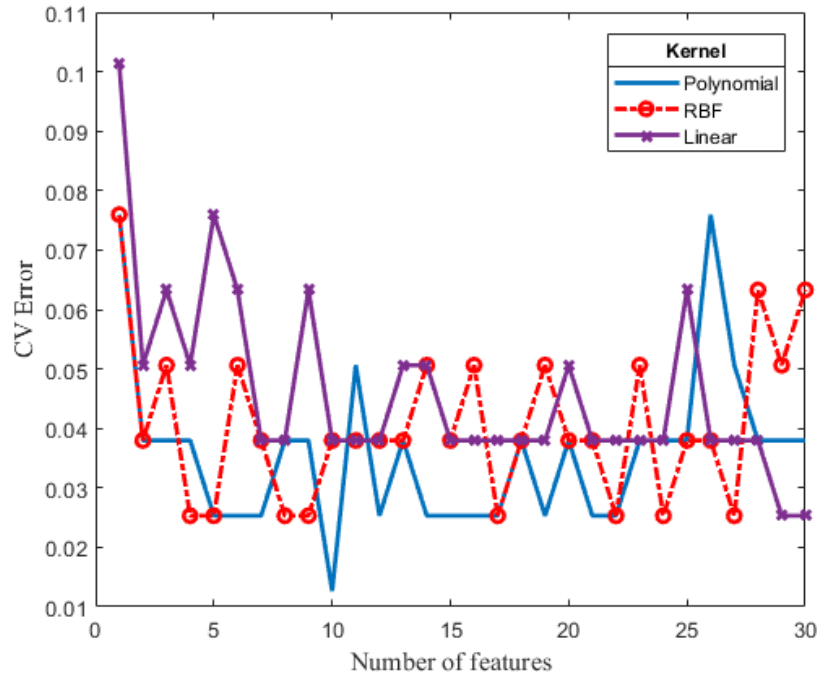


Figure. 83. CV error as a function of number of features for every used kernel function.

Table 7. Performance metrics for the FFSW approach.

BEST KERNEL	TEST ERROR	SENSITIVITY	SPECIFICITY	YI	ACCURACY
POLYNOMIAL	1.1%	97.9%	100%	97.9%	98.9%

D. Discussion

The presented system establishes a unique and innovative platform that successfully blends EM-based sensing with medical diagnostics. The combination of several sensor design decisions tailored for malignant lesion detection enhanced our sensitivity in the microwave frequency range. Our findings, through robust statistical modeling, attest to our system’s ability to electromagnetically interrogate suspected skin

lesions non-invasively. It is necessary to note that the enhanced sensitivity of the sensor, and specifically the multi-feature statistical analysis methods adopted by our approach, unlocked deep insights into the nature of the skin lesion under test and highlighted the importance of analyzing the data at multiple features. Our results are highly encouraging, exhibiting sensitivity, accuracy, and specificity $> 95\%$, which paves the way for the development of a commercial solution that can be potentially integrated into clinical settings.

CHAPTER VIII

CONCLUSION AND FUTURE WORK

Skin cancer diagnosis methods are time-consuming and invasive, and there is currently no simple, portable, and cost-effective screening alternative for quick and easy integration into a clinical setting. As a result, we proposed an EM-based sensing system composed of a highly sensitive front-end sensor operating at 4.75 GHz and its corresponding backend wave analyzer for the quick non-invasive diagnosis of skin cancer. In collaboration with medical professionals from the AUBMC, clinical trials are conducted on patients with skin cancer to validate the functionality of our system. Our findings are very encouraging, where significant and clear differences between cancerous lesions and healthy tissues are observed. Furthermore, we studied the relationships within the obtained data and the corresponding trends, which culminated in developing two statistical classification models. Our two classification models are SVM-based classifiers that follow two approaches, a correlation-based one, and a best-feature selector. Both approaches yielded significant specificity, accuracy, and sensitivity. Our proposed work successfully and definitively validates the strength of the proposed system and techniques which have a great potential into becoming a tool that augments the traditional inspection techniques followed by medical professionals.

Future versions of the proposed system aim to increase processing speed by utilizing performance microcontrollers and field programmable arrays (FPGAs), on-board memory, an external analog-to-digital convert (ADC), and sensors that operate at multiple frequencies to explore trends at more features. Furthermore, we also aim to expand our clinical trials to include a larger number of skin cancer patients, including different types of skin cancer and potentially other debilitating diseases.

BIBLIOGRAPHY

- [1] K. Brind'Amour, "All About Common Skin Disorders," Accessed: Jan. 03, 2021. [Online]. Available: <https://www.healthline.com/health/skin-disorders>.
- [2] "Radiation: Ultraviolet (UV) radiation and skin cancer.," Oct. 2017, Accessed: Jan. 03, 2021. [Online]. Available: [https://www.who.int/news-room/q-a-detail/radiation-ultraviolet-\(uv\)-radiation-and-skin-cancer](https://www.who.int/news-room/q-a-detail/radiation-ultraviolet-(uv)-radiation-and-skin-cancer).
- [3] "Early Detection," *The Skin Cancer Foundation*. <https://www.skincancer.org/early-detection/> (accessed Jan. 03, 2021).
- [4] "Basal and Squamous Cell Skin Cancer Tests | Skin Cancer Biopsy." <https://www.cancer.org/cancer/basal-and-squamous-cell-skin-cancer/detection-diagnosis-staging/how-diagnosed.html> (accessed Jan. 03, 2021).
- [5] M. Lazebnik *et al.*, "A large-scale study of the ultrawideband microwave dielectric properties of normal, benign and malignant breast tissues obtained from cancer surgeries," *Phys. Med. Biol.*, vol. 52, no. 20, pp. 6093–6115, Oct. 2007, doi: 10.1088/0031-9155/52/20/002.
- [6] J. L. Schepps and K. R. Foster, "The UHF and microwave dielectric properties of normal and tumour tissues: variation in dielectric properties with tissue water content," *Phys. Med. Biol.*, vol. 25, no. 6, pp. 1149–1159, Nov. 1980, doi: 10.1088/0031-9155/25/6/012.
- [7] S. I. Alekseev and M. C. Ziskin, "Human skin permittivity determined by millimeter wave reflection measurements," *Bioelectromagnetics*, vol. 28, no. 5, pp. 331–339, 2007, doi: <https://doi.org/10.1002/bem.20308>.

- [8] A. Taeb, S. Gigoyan, and S. Safavi-Naeini, “Millimetre-wave waveguide reflectometers for early detection of skin cancer,” *IET Microw. Antennas Propag.*, vol. 7, no. 14, pp. 1182–1186, Nov. 2013, doi: 10.1049/iet-map.2013.0189.
- [9] F. Töpfer, S. Dudorov, and J. Oberhammer, “Millimeter-Wave Near-Field Probe Designed for High-Resolution Skin Cancer Diagnosis,” *IEEE Trans. Microw. Theory Tech.*, vol. 63, no. 6, pp. 2050–2059, Jun. 2015, doi: 10.1109/TMTT.2015.2428243.
- [10] A. Mirbeik-Sabzevari, E. Oppelaar, R. Ashinoff, and N. Tavassolian, “High-Contrast, Low-Cost, 3-D Visualization of Skin Cancer Using Ultra-High-Resolution Millimeter-Wave Imaging,” *IEEE Trans. Med. Imaging*, vol. 38, no. 9, pp. 2188–2197, Sep. 2019, doi: 10.1109/TMI.2019.2902600.
- [11] V. Suntzeff and C. Carruthers, “The water content in the epidermis of mice undergoing carcinogenesis by methylcholanthrene,” *Cancer Res.*, vol. 6, pp. 574–577, Oct. 1946.
- [12] A. Zamani, S. A. Rezaeieh, and A. M. Abbosh, “Lung cancer detection using frequency-domain microwave imaging,” *Electron. Lett.*, vol. 51, no. 10, pp. 740–741, Apr. 2015, doi: 10.1049/el.2015.0230.
- [13] S. I. Alekseev, I. Szabo, and M. C. Ziskin, “Millimeter wave reflectivity used for measurement of skin hydration with different moisturizers,” *Skin Res. Technol. Off. J. Int. Soc. Bioeng. Skin ISBS Int. Soc. Digit. Imaging Skin ISDIS Int. Soc. Skin Imaging ISSI*, vol. 14, no. 4, pp. 390–396, Nov. 2008, doi: 10.1111/j.1600-0846.2008.00319.x.

- [14] K. Haddadi, D. Glay, and T. Lasri, "A 60 ghz scanning near-field microscope with high spatial resolution sub-surface imaging," *IEEE Microw. Wirel. Compon. Lett.*, vol. 21, no. 11, pp. 625–627, Nov. 2011, doi: 10.1109/LMWC.2011.2167744.
- [15] L. F. Handjojo, K. J. Bois, J. Bauer, R. Hamilton, and R. Zoughi, "Broad-Band Microwave Dielectric Property Characterization and Nondestructive Inspection of Various Glass Specimens," 2000, doi: 10.1080/10589750008953063.
- [16] M. T. Ghasr, S. Kharkovsky, R. Zoughi, and R. Austin, "Comparison of near-field millimeter-wave probes for detecting corrosion precursor pitting under paint," *IEEE Trans. Instrum. Meas.*, vol. 54, no. 4, pp. 1497–1504, Aug. 2005, doi: 10.1109/TIM.2005.851086.
- [17] A. Mirbeik-Sabzevari, R. Ashinoff, and N. Tavassolian, "Ultra-wideband millimeter-wave dielectric characteristics of freshly excised normal and malignant human skin tissues," *IEEE Trans. Biomed. Eng.*, vol. 65, no. 6, pp. 1320–1329, Jun. 2018, doi: 10.1109/TBME.2017.2749371.
- [18] M. Tabib-Azar, J. L. Katz, and LeClair, "Evanescent microwaves: a novel super-resolution noncontact nondestructive imaging technique for biological applications," *IEEE Trans. Instrum. Meas.*, vol. 48, no. 6, pp. 1111–1116, Dec. 1999, doi: 10.1109/19.816123.
- [19] F. Kazemi, F. Mohanna, and J. Ahmadi-Shokouh, "Detection of biological abnormalities using a near-field microwave microscope," *Int. J. Microw. Wirel. Technol.*, vol. 10, no. 8, pp. 933–941, Oct. 2018, doi: 10.1017/S1759078718000752.

- [20] O. Malyuskin and V. F. Fusco, “High-Resolution Microwave Near-Field Surface Imaging Using Resonance Probes,” *IEEE Trans. Instrum. Meas.*, vol. 65, no. 1, pp. 189–200, Jan. 2016, doi: 10.1109/TIM.2015.2476277.
- [21] D. Isakov, C. J. Stevens, F. Castles, and P. S. Grant, “A Split Ring Resonator Dielectric Probe for Near-Field Dielectric Imaging,” *Sci. Rep.*, vol. 7, no. 1, Art. no. 1, May 2017, doi: 10.1038/s41598-017-02176-3.
- [22] E. F. Buskgaard, B. K. Krøyer, A. Tatomirescu, O. Franek, and G. F. Pedersen, “Tiny Integrated Network Analyzer for Noninvasive Measurements of Electrically Small Antennas,” *IEEE Trans. Microw. Theory Tech.*, vol. 64, no. 1, pp. 279–288, Jan. 2016, doi: 10.1109/TMTT.2015.2504475.
- [23] M. A. Abou-Khousa, M. A. Baumgartner, S. Kharkovsky, and R. Zoughi, “Novel and simple high-frequency single-port vector network analyzer,” *IEEE Trans. Instrum. Meas.*, vol. 59, no. 3, pp. 534–542, Mar. 2010, doi: 10.1109/TIM.2009.2024701.
- [24] L. F. Chen, C. K. Ong, C. P. Neo, V. V. Varadan, and V. K. Varadan, *Microwave electronics: Measurement and materials characterization*. Wiley, 2004.
- [25] C. Gabriel, S. Gabriel, and E. Corthout, “The dielectric properties of biological tissues: I. Literature survey,” *Phys. Med. Biol.*, vol. 41, no. 11, pp. 2231–2249, Nov. 1996, doi: 10.1088/0031-9155/41/11/001.
- [26] S. Gabriel, R. W. Lau, and C. Gabriel, “The dielectric properties of biological tissues: II. Measurements in the frequency range 10 Hz to 20 GHz,” *Phys. Med. Biol.*, vol. 41, no. 11, pp. 2251–2269, Nov. 1996, doi: 10.1088/0031-9155/41/11/002.

- [27] S. Gabriel, R. W. Lau, and C. Gabriel, “The dielectric properties of biological tissues: III. Parametric models for the dielectric spectrum of tissues,” *Phys. Med. Biol.*, vol. 41, no. 11, pp. 2271–2293, Nov. 1996, doi: 10.1088/0031-9155/41/11/003.
- [28] H. P. Schwan, “Electrical Properties of Tissue and Cell Suspensions* *This work was supported in part by grants from the United States Public Health Service, H-1253(c2-4) and in part by the Office of Naval Research, 119–289.,” in *Advances in Biological and Medical Physics*, vol. 5, J. H. Lawrence and C. A. Tobias, Eds. Elsevier, 1957, pp. 147–209.
- [29] “5.1 Layers of the Skin – Anatomy & Physiology.” <https://open.oregonstate.edu/aandp/chapter/5-1-layers-of-the-skin/> (accessed Jan. 03, 2021).
- [30] M. Venus, J. Waterman, and I. McNab, “Basic physiology of the skin,” *Surg. Oxf.*, vol. 29, no. 10, pp. 471–474, Oct. 2011, doi: 10.1016/j.mpsur.2011.06.010.
- [31] “Anatomy and Physiology of the Skin: Erratum,” *J. Dermatol. Nurses Assoc.*, vol. 3, no. 6, p. 366, Dec. 2011, doi: 10.1097/JDN.0b013e31823cccbe.
- [32] “Considering Laser Hair Removal? Get To Know Your Fitzpatrick Skin Type - Barris Laser & Skin Care - Boulder, CO.” <https://barrislaser.com/considering-laser-hair-removal-get-to-know-your-fitzpatrick-skin-type/> (accessed Jan. 10, 2021).
- [33] “Basal cell carcinoma - Symptoms and causes,” *Mayo Clinic*. <https://www.mayoclinic.org/diseases-conditions/basal-cell-carcinoma/symptoms-causes/syc-20354187> (accessed Jan. 03, 2021).

- [34] “Squamous cell carcinoma of the skin - Symptoms and causes,” *Mayo Clinic*.
<https://www.mayoclinic.org/diseases-conditions/squamous-cell-carcinoma/symptoms-causes/syc-20352480> (accessed Jan. 03, 2021).
- [35] “Melanoma - Symptoms and causes,” *Mayo Clinic*.
<https://www.mayoclinic.org/diseases-conditions/melanoma/symptoms-causes/syc-20374884> (accessed Jan. 03, 2021).
- [36] G. Martinsen, S. Grimnes, and H. Schwan, “Interface Phenomena and Dielectric Properties of Biological Tissue.,” 2002.
- [37] “Skin cancer - Symptoms and causes,” *Mayo Clinic*.
<https://www.mayoclinic.org/diseases-conditions/skin-cancer/symptoms-causes/syc-20377605> (accessed Jan. 03, 2021).
- [38] “N1501A Dielectric Probe Kit | Keysight.” <https://www.keysight.com/en/pd-2492144-pn-N1501A/dielectric-probe-kit?cc=US&lc=eng> (accessed Jan. 03, 2021).
- [39] D. Pozar, *Microwave engineering*. Hoboken, NJ: Wiley, 2012.
- [40] C. Balanis, *Antenna theory: Analysis and design*. Hoboken, New Jersey: John Wiley, 2016.
- [41] “ANSYS HFSS: High Frequency Electromagnetic Field Simulation Software.”
<https://www.ansys.com/products/electronics/ansys-hfss> (accessed Jan. 03, 2021).
- [42] F. Kazemi, F. Mohanna, and J. Ahmadi-Shokouh, “Nondestructive high-resolution microwave imaging of biomaterials and biological tissues,” *AEU - Int. J. Electron. Commun.*, vol. 84, pp. 177–185, 2018, doi:
<https://doi.org/10.1016/j.aeue.2017.10.031>.
- [43] “N9923A FieldFox Handheld RF Vector Network Analyzer, 4 GHz and 6 GHz | Keysight.” <https://www.keysight.com/en/pdx-x201782-pn-N9923A/fieldfox->

- handheld-rf-vector-network-analyzer-4-ghz-and-6-ghz?cc=LB&lc=eng (accessed Jan. 03, 2021).
- [44] “RF Safety FAQ,” *Federal Communications Commission*, Nov. 25, 2015. <https://www.fcc.gov/engineering-technology/electromagnetic-compatibility-division/radio-frequency-safety/faq/rf-safety> (accessed Jan. 08, 2021).
- [45] “Radio Frequency Safety,” *Federal Communications Commission*, Mar. 02, 2011. <https://www.fcc.gov/general/radio-frequency-safety-0> (accessed Jan. 08, 2021).
- [46] “MAX2871 23.5MHz to 6000MHz Fractional/Integer-N Synthesizer/VCO - Maxim Integrated.” <https://www.maximintegrated.com/en/products/comms/wireless-rf/MAX2871.html> (accessed Jan. 03, 2021).
- [47] A. C. F. Changpuak aka, “Arduino Shield “MILLIMOD,”” www.changpuak.ch. <https://www.changpuak.ch/electronics/Arduino-Shield-MILLIMOD.php> (accessed Jan. 08, 2021).
- [48] “ZHDC-10-63+ - Mini Circuits | Directional Coupler.” <https://www.everythingrf.com/products/directional-couplers/mini-circuits/45-12-zhdc-10-63> (accessed Jan. 03, 2021).
- [49] “Mini-Circuits.” <https://www.minicircuits.com/WebStore/dashboard.html?model=SIM-762H%2B> (accessed Jan. 03, 2021).
- [50] Keysight, “PathWave Advanced Design System (ADS),” *Keysight*. <https://www.keysight.com/zz/en/products/software/pathwave-design-software/pathwave-advanced-design-system.html> (accessed Jan. 03, 2021).

- [51] “AD8302 Datasheet and Product Info | Analog Devices.”
<https://www.analog.com/en/products/ad8302.html#product-overview> (accessed Jan. 03, 2021).
- [52] S. Wetterlin, “USE OF PHASE SHIFT TO RESOLVE SIGN AMBIGUITY,” p. 9.
- [53] “Arduino Nano 33 IoT | Arduino Official Store.”
<https://store.arduino.cc/usa/nano-33-iot> (accessed Jan. 03, 2021).
- [54] “EasyEDA - Online PCB design & circuit simulator.” <https://easyeda.com/>
(accessed Jan. 03, 2021).
- [55] “LP5907 data sheet, product information and support | TI.com.”
<https://www.ti.com/product/LP5907> (accessed Jan. 08, 2021).
- [56] “PCB Prototype - JLCPCB.”
<https://jlcpcb.com/quote/pcbOrderFaq/PCB%20Stackup> (accessed Jan. 03, 2021).
- [57] “Via Stitching and Via Shielding | Altium Designer 21.0 User Manual | Documentation.” <https://www.altium.com/documentation/altium-designer/via-stitching-and-via-shielding-ad> (accessed Jan. 08, 2021).
- [58] “Software.” <https://www.arduino.cc/en/software> (accessed Jan. 08, 2021).
- [59] D. Huber, M. Talary, F. Dewarrat, and A. Caduff, “The compensation of perturbing temperature fluctuation in glucose monitoring technologies based on impedance spectroscopy,” *Med. Biol. Eng. Comput.*, vol. 45, no. 9, pp. 863–876, Sep. 2007, doi: 10.1007/s11517-007-0229-3.
- [60] D. A. Pollacco, L. Farina, P. S. Wismayer, L. Farrugia, and C. V. Sammut, “Characterization of the dielectric properties of biological tissues and their

- correlation to tissue hydration,” *IEEE Trans. Dielectr. Electr. Insul.*, vol. 25, no. 6, pp. 2191–2197, Dec. 2018, doi: 10.1109/TDEI.2018.007346.
- [61] R. J. Halter *et al.*, “The correlation of in vivo and ex vivo tissue dielectric properties to validate electromagnetic breast imaging: initial clinical experience,” *Physiol. Meas.*, vol. 30, no. 6, pp. S121–S136, Jun. 2009, doi: 10.1088/0967-3334/30/6/S08.
- [62] L. Farrugia, P. S. Wismayer, L. Z. Mangion, and C. V. Sammut, “Accurate in vivo dielectric properties of liver from 500 MHz to 40 GHz and their correlation to ex vivo measurements,” *Electromagn. Biol. Med.*, vol. 35, no. 4, pp. 365–373, Oct. 2016, doi: 10.3109/15368378.2015.1120221.
- [63] S. Salahuddin, A. L. Gioia, M. A. Elahi, E. Porter, M. O’Halloran, and A. Shahzad, “Comparison of in-vivo and ex-vivo dielectric properties of biological tissues,” in *2017 International Conference on Electromagnetics in Advanced Applications (ICEAA)*, Sep. 2017, pp. 582–585, doi: 10.1109/ICEAA.2017.8065312.
- [64] S. Fotouhi, S. Asadi, and M. W. Kattan, “A comprehensive data level analysis for cancer diagnosis on imbalanced data,” *J. Biomed. Inform.*, vol. 90, p. 103089, Feb. 2019, doi: 10.1016/j.jbi.2018.12.003.
- [65] Z. Huang, C. Yang, X. Chen, K. Huang, and Y. Xie, “Adaptive over-sampling method for classification with application to imbalanced datasets in aluminum electrolysis,” *Neural Comput. Appl.*, vol. 32, no. 11, pp. 7183–7199, Jun. 2020, doi: 10.1007/s00521-019-04208-7.
- [66] A. Fernandez, S. Garcia, F. Herrera, and N. V. Chawla, “SMOTE for Learning from Imbalanced Data: Progress and Challenges, Marking the 15-year

- Anniversary,” *J. Artif. Intell. Res.*, vol. 61, pp. 863–905, Apr. 2018, doi: 10.1613/jair.1.11192.
- [67] M. Alghamdi, M. Al-Mallah, S. Keteyian, C. Brawner, J. Ehrman, and S. Sakr, “Predicting diabetes mellitus using SMOTE and ensemble machine learning approach: The Henry Ford Exercise Testing (FIT) project,” *PLoS ONE*, vol. 12, no. 7, Jul. 2017, doi: 10.1371/journal.pone.0179805.
- [68] S. F. Abdoh, M. A. Rizka, and F. A. Maghraby, “Cervical Cancer Diagnosis Using Random Forest Classifier With SMOTE and Feature Reduction Techniques,” *IEEE Access*, vol. 6, pp. 59475–59485, 2018, doi: 10.1109/ACCESS.2018.2874063.
- [69] W. Wiharto, H. Kusnanto, and H. Herianto, “Intelligence System for Diagnosis Level of Coronary Heart Disease with K-Star Algorithm,” *Healthc. Inform. Res.*, vol. 22, no. 1, pp. 30–38, Jan. 2016, doi: 10.4258/hir.2016.22.1.30.
- [70] J. Cervantes, F. Garcia-Lamont, L. Rodríguez-Mazahua, and A. Lopez, “A comprehensive survey on support vector machine classification: Applications, challenges and trends,” *Neurocomputing*, vol. 408, pp. 189–215, Sep. 2020, doi: 10.1016/j.neucom.2019.10.118.
- [71] Y. Shen, C. Wu, C. Liu, Y. Wu, and N. Xiong, “Oriented Feature Selection SVM Applied to Cancer Prediction in Precision Medicine,” *IEEE Access*, vol. 6, pp. 48510–48521, 2018, doi: 10.1109/ACCESS.2018.2868098.
- [72] S. HUANG, N. CAI, P. P. PACHECO, S. NARANDES, Y. WANG, and W. XU, “Applications of Support Vector Machine (SVM) Learning in Cancer Genomics,” *Cancer Genomics Proteomics*, vol. 15, no. 1, pp. 41–51, Dec. 2017, doi: 10.21873/cgp.20063.

- [73] E. Zafiropoulos, I. Maglogiannis, and I. Anagnostopoulos, “A Support Vector Machine Approach to Breast Cancer Diagnosis and Prognosis,” in *Artificial Intelligence Applications and Innovations*, Boston, MA, 2006, pp. 500–507, doi: 10.1007/0-387-34224-9_58.
- [74] H.-J. Chiu, T.-H. S. Li, and P.-H. Kuo, “Breast Cancer–Detection System Using PCA, Multilayer Perceptron, Transfer Learning, and Support Vector Machine,” *IEEE Access*, vol. 8, pp. 204309–204324, 2020, doi: 10.1109/ACCESS.2020.3036912.
- [75] hefinioanrhys, “Support Vector Machines with the mlr package,” *R-bloggers*, Oct. 10, 2019. <https://www.r-bloggers.com/2019/10/support-vector-machines-with-the-mlr-package/> (accessed Jan. 09, 2021).

